Mid-Pliocene Greenhouse Climate Simulated by Atmospheric General Circulation Model : Comparison with Paleoclimate Proxy Data

January 2012

Youichi KAMAE

Mid-Pliocene Greenhouse Climate Simulated by Atmospheric General Circulation Model : Comparison with Paleoclimate Proxy Data

A Dissertation Submitted to
the Graduate School of Life and Environmental Sciences,
the University of Tsukuba
in Partial Fulfillment of the Requirements
for the Degree of Doctor of Philosophy in Science
(Doctoral Program in Geoenvironmental Sciences)

Youichi KAMAE

Abstract

The mid-Pliocene warm period (~3 million years ago; 3 Ma) is one of the plausible scenarios which provide insight into the climate system in a globally warmer world as projected by climate models for the future. The paleoenvironmental reconstructions by the Pliocene Research, Interpretation and Synoptic Mapping phase 3 (PRISM3) reveal significant warmer climate in mid- and high-latitude and moister climate in subtropical regions relative to the present-day.

The sensitivity of an atmospheric general circulation model (AGCM) is studied by prescribing surface condition based on the PRISM3 paleoenvironmental reconstructions. The simulated Walker circulation generally slows down, inducing convergent anomaly over the African continent and divergent anomaly over the Asian monsoon region at the lower troposphere; and vice versa at the upper troposphere in response to the reduced east-west gradient of the tropical sea surface temperature (SST) in that period. The ascending branch of the Hadley cell expands poleward, implying a weakening of the meridional circulation in response to the warmer SST in the higher latitudes. To identify the physical reason for the modulation of the wet-dry climatological pattern in low latitudes, additional sensitivity experiments were conducted by changing the configurations of ice-sheet cover, vegetation and zonal patterns of the SST. The results indicate that the reduction of meridional and zonal gradient of tropical SST is the key factor for the expansion of proxy-suggested wetter climate over Africa.

The Earth climate system during the 3 Ma is cooled by enhancement of longwave emission owing to the warmer condition in mid- and high-latitude. However, net radiative balance (positive downward) at top of atmosphere (TOA) is positive (+3.8 W m^{-2} in global mean) particularly in low latitude. The alteration of SST pattern in low latitude, associated with the changes in ocean heat transport and thermal structure, induces warming of the Earth system through reductions of cloud cover. The magnitude of the SST effect is prior to the other factors

of surface forcings, the sea ice reduction, changes in the topography, the shrinking of the land glaciers, and the shifts of vegetation cover. The weakening of shortwave reflection by cloud according to the reductions of cloud cover, i.e., deep convective cloud in the northern Indian Ocean, western tropical Pacific, and Southern Pacific Convergence Zone (SPCZ), and low-level stratocumulus in the eastern edges of the ocean sectors, is primarily induced by the diminished east-west gradient of SST in low latitude.

The paleovegetational dataset during 3 Ma in lower latitudes are applied to evaluation for annual-mean 3 Ma climate simulated by the AGCM. The model-derived warmer climate in mid-latitude and the wetter condition in subtropics are generally confirmed by the terrestrial proxy data. The comparisons of their general patterns reveal an ability of AGCM to predict the sustained-warmer climate under the different forcings from present day. In comparing to the proxy data, the enhanced rainfall over the semi-arid regions in accordance with the alteration of Hadley/Walker circulation in 3 Ma is supported but the extent may be partially underestimated. The paleobotanical data in the lower latitudes indicate an importance of interactive response of vegetation to climate under the equilibrium warmer state of the Earth system.

Key words: Mid-Pliocene, El-Niño like condition, proxy data, cloud radiative forcing, data-model comparison, equilibrium biogeography model

Contents

List of Tables

List of Figures

1. Introduction

1.1 Mid-Pliocene – A warm scenario for the Earth climate system

During the Quaternary, 2.58 million years ago (Ma) to present, the earth climate system experienced predominant variation between warm interglacial and cold glacial conditions, i.e., glacial-interglacial cycles, accompanied with variations of orbital forcings, atmospheric trace gas concentrations, and extent of Northern Hemisphere ice sheets (e.g., Cubasch et al. 2006; Otto-Bliesner et al. 2006; Abe-Ouchi et al. 2007). In contrast, the mid-Pliocene warm period (3.29~2.97 Ma), a period before the Quaternary, is a warm interval experienced in transition from the sustained warmer climate of the early Pliocene, with relatively small (or absent) Northern Hemisphere ice sheets, to the cooler climate of the Quaternary (e.g., Zachos et al. 2001; Lisiecki and Raymo 2005; Jansen et al. 2007). It is also the most recent period when the global climate was substantially warmer than the present-day for a sustained time (~300 thousand years, e.g., Dowsett et al. 1994; Haywood et al. 2009a). The mid-Pliocene warm period is one of the interval in which the Earth climate system reached its equilibrium state with greatly warmth in the past. In addition, the geographic distribution of continents and oceans in this period was similar to that in the present day. The effort in simulating the climate for this interval is expected to make substantial contributions to the advanced validation of climate models predicting future climate change (e.g., Crowley 1996; Salzmann et al. 2009), to the estimation of "Earth system sensitivity" (Lunt et al. 2010; Pagani et al. 2010), and to provide insight into the globally warmer world that is predicted by the climate models for the future (e.g., Meehl et al. 2007; Knutti and Hegerl 2008).

The paleoclimate conditions in the mid-Pliocene are investigated by a series of studies that summarized conditions at a large number of marine and terrestrial sites and areas. As a part of the United State Geological Survey (USGS) Global Changes Research effort, the Pliocene Research Interpretation and Synoptic Mapping (PRISM) Project (e.g., Dowsett et al. 1994, 1996,

1999, 2009b) has documented the characteristics of climate in the mid-Pliocene warm period on a global scale by use of various types of proxy records (e.g., foraminifera, diatoms, ostracods, pollen and plant macrofossil data). The PRISM datasets have been used to drive numerical simulations designed to explore the impact of climate forcing and feedback during the Pliocene (e.g., Chandler et al. 1994; Sloan et al. 1996; Jiang et al. 2005), and assess the reproducibility of climate simulations derived by general circulation models (GCMs) in this period (e.g., Haywood et al. 2005; Haywood et al. 2009b). Recently, as a worldwide framework for studying the paleoclimate reconstructions and simulations, the Paleoclimate Modeling Intercomparison Project (PMIP; e.g., Joussaume et al. 1999; Braconnot et al. 2007a, b) has focused on the mid-Pliocene warm period as one of new target intervals in its latest phase (PMIP3; Otto-Bliesner et al. 2009).

1.2 Climate reconstructions during mid-Pliocene warm period

The reconstruction of sea surface temperature (SST) during the mid-Pliocene by the latest phase of the PRISM project (PRISM3; Haywood et al. 2010) features pronounced warming (up to ~15 K) in mid- and high-latitudes, particularly in the North Atlantic Ocean (Dowsett et al. 2009; details are described in Chapter 2). In contrast, the SST is similar to the present day value in tropical regions. The SST pattern in the mid-Pliocene is distinct from the significant warming trend in low latitude in the future projection by experiments forced by increasing atmospheric greenhouse gases concentrations (e.g., Meehl et al. 2007). Recently, it was revealed that the proxy records from the modern upwelling areas off the west coast of South America suggest warmer surface conditions in the mid-Pliocene than the present day (e.g., Ravelo et al. 2004; Haywood et al. 2005; Wara et al. 2005; Dekens et al. 2007; Dowsett and Robinson 2009). In the tropical Pacific, greatly weakening of east-west gradient of SST and associated atmospheric circulation are often referred to as “permanent El-Niño” or “El-Niño like condition” (e.g., Wara et al. 2005; Brierley et al. 2009; Dowsett and Robinson 2009). The east-west anomalous SST

contrast in the tropics could have played a fundamental role for atmospheric general circulation patterns and global climate in the mid-Pliocene (e.g., Etourneau et al. 2010; Ravelo 2010). Possible mechanisms of formation and sustainment of the salient features in SST pattern during 3Ma (intensification of meridional heat transport, deep thermocline depth, closure or shoaling of seaways, intensification of subsurface mixing induced by tropical cyclone activity) are discussed widely (Philander and Fedorov 2003; Fedorov et al. 2006; Lunt et al. 2008a; Karas et al. 2009; Sarnthein et al. 2009; Steph et al. 2010; Fedorov et al. 2010). It is still under discussion when and how the reductions of SST gradient meridionally or zonally were started to develop and encourage the Plio-Pleistocene climate transition (Etourneau et al. 2010; Ravelo 2010; Li et al. 2011).

Numerical studies through the use of GCMs evoked some features of the atmospheric general circulation in the mid-Pliocene. One of the key aspects of the mid-Pliocene climate was a weakening of atmospheric east-west overturning circulation in the tropics, manifested as Walker circulation, as a part of a "permanent El-Niño" condition (e.g., Barreiro et al. 2006; Brierley et al. 2009) resulting from the reduction of east-west temperature gradient in the tropical Pacific (e.g., Ravelo et al. 2004; Wara et al. 2005; Dekens et al. 2007). As for the latitudinal direction, characteristics of mean meridional circulation (MMC) in the tropics (Hadley circulation) during this interval were investigated by various configurations (Sloan et al. 1996; Barreiro et al. 2006).

The AGCM studies forced by SST with coarser resolution or present-day meridional gradient in the tropics did not show any significant changes in the strength and location of the Hadley circulation. In contrast, weakening of the Hadley circulation has been also reported in several studies (e.g., Chandler et al. 1994; Haywood et al. 2000; Jiang et al. 2005). Brierley et al. (2009) revealed that a diminished meridional gradient of SST in low latitude, as based on several types of proxy records, is responsible for the greatly weakened and a latitudinal expansion of the Hadley circulation in early Pliocene (ca. 4 Ma). Haywood et al. (2009b) showed broadening of the Hadley cells caused by reduction in the equator-to-pole temperature gradient in the results of

two AGCM simulations using PRISM2 boundary conditions (Dowsett et al. 1999).

In addition to the alteration of the high-latitude climate, the reconstructed air temperature and rainfall show that the atmospheric circulation in low latitude was also largely modulated, and inherent physical processed are insufficiently understood, especially monsoon related wet/dry climate (e.g., Chandler et al. 1994; Sloan et al. 1996; Haywood et al. 2009b). The improvement in the reconstruction of the paleoenvironmental conditions by PRISM has provided insight into large-scale atmospheric circulation for altered regional climate patterns under warmer conditions as well as validation of the simulation with paleovegetation data. The purpose of the present study is examining the details of atmospheric global circulation and tropical/subtropical climate patterns in low latitude during the mid-Pliocene warm period by use of state-of-the-art PRISM reconstruction dataset, which has additional data points in equatorial Pacific and other regions. Examining the consistency of simulated climate with the terrestrial proxy data may contribute to test the ability of GCM to simulate the climate under the warmer conditions. It should be noted that formation of the climate system through the modulation of the oceanic general circulation and SST distribution during this period is not discussed in this study because sea surface conditions, which also includes substantial influences over the other boundary conditions, are prescribed. We only consider the annual-mean values in this paper because the information about seasonality in proxy data was not sufficient to verify the results of simulations. Results of 3 Ma climate simulation are described in Chapter 3.

1.3 Radiative balance in a warm phase of the Earth climate system

The driving factors for the Pliocene warmth have been discussed widely. The atmospheric composition is one of the major factors for the warm condition in 3 Ma. The atmospheric CO_2 concentration during 3 Ma documented by several types of proxy evidences (e.g., Van der Burgh et al. 1993; Kürschner et al. 1996; Raymo et al. 1996; Pagani et al. 2010) is significantly higher (330~425 ppmv) than the level in pre-industrial (280 ppmv). However, the radiative forcing of

the CO_2 with estimated concentration is deficient for the greatly warmer condition and the regionality of the surface thermal environment in 3 Ma (Crowley 1996; Haywood et al. 2009a). Haywood and Valdes (2004) concluded that the dominant factor for the global Pliocene warmth is the reduced extent of ice sheet and sea-ice cover resulting in a strong ice-albedo feedback. Lunt et al. (2008b) tested hypotheses about the onset of Northern Hemisphere glaciations during the late Pliocene and concluded that the decrease in atmospheric CO_2 during the late Pliocene mainly encouraged the enhancement of the glaciation. Lunt et al. (2010) revealed that the alterations of the land ice and vegetation are necessary for the simulation of the greatly-warmed climate during 3 Ma in addition to the increase in CO_2 concentration. In addition, Haywood et al. (2009b) showed role of increased cloud cover in high-latitude for the warmer condition in 3 Ma using two kinds of general circulation models (GCMs). The major factors for the 3 Ma warmth have been focused on the CO_2 concentration and its effects in the higher-latitude regions through ice-albedo, cloud, and vegetation feedbacks.

In contrast, lower latitude perspective is also important for the insight about the 3Ma warmth (e.g., Ravelo 2010; Kamae et al. 2011; Kamae and Ueda 2012a). Brierley et al. (2009) and Kamae et al. (2011) showed greatly alteration in atmospheric circulation and water cycle in low latitude corresponding with reductions of the meridional and zonal SST gradients. The Hadley and Walker circulations are weakened significantly, which might contribute for the characteristics of the 3 Ma climate in contrast to that in the Quaternary (e.g., Etourneau et al. 2010; Li et al. 2011). In several studies, the possible impact of the reduction of east-west SST gradient in tropics for the 3 Ma warmth by assuming zonally-uniform SST in tropics during the Pliocene through alteration of radiative balance at top of the atmosphere (TOA) over the stratocumulus regions is revealed (Barreiro et al. 2006; Brierley and Fedorov 2010). Barreiro et al. (2006) showed that the low-level stratocumulus cloud over subtropical upwelling regions in eastern edges of ocean sectors and associated shortwave reflection by cloud were reduced, resulting the surface warming in low latitude. Brierley and Fedorov (2010) also quantified the

impacts of changes in the meridional and zonal SST gradient in low latitude during early Pliocene (4.2~4 Ma) and concluded that magnitudes of those effects on global radiative balances are comparable. Fedorov et al. (2010) proposed a hypothesis about more frequent and/or stronger tropical cyclones affected the ocean's heat uptake, poleward heat transport, and hence global temperatures during the Pliocene.

The greatly alterations of surface environments in 3 Ma, extremely-warmer condition in northern North Atlantic/Arctic regions, shrinking of continental glaciers and sea ice coverage, and changes of spatial patterns in vegetation revealed by PRISM3 paleoenvironmental dataset, would have significant role for the the 3 Ma warmth through the changes in TOA radiative balance. However, the magnitude and spatial patterns of them have not been investigated. The PRISM3 dataset has been used in the PlioMIP experiments (Haywood et al. 2010, 2011) for the systematic study of GCMs and to assess their ability to simulate the large differences of climate that occurred in the 3 Ma. The recent improvement in SST reconstruction of PRISM3 obtained the new proxy records particularly in the tropical Pacific which made significant advancement in reproducing general climate pattern in low latitude. We quantify the TOA radiative imbalance accompanied with the alterations of surface boundary conditions or atmospheric forcings and relative importances for the sustainment of the warm phase of the Earth system. The radiative balance at TOA during 3 Ma is described in Chapter 4.

1.4 Data-model comparison using paleovegetation data

Geographical distributions of surface ecosystem, including vegetation, are primarily influenced by climate changes. Global patterns of vegetation also change regional climate as a boundary forcing (e.g., Harrison et al. 1995) or through biogeophysical and/or biogeochemical feedbacks (e.g., Claussen 2009) on atmosphere-ocean-land interactions in the past and the future (e.g., Haywood and Valdes 2006; O'ishi et al. 2009). Evaluations of simulated paleoclimate with reconstructed paleovegetation data could test for the abilities of numerical climate models to

simulate climate change under different boundary conditions and different forcing mechanisms (Bradley 1999).

Paleoenvironmental data in 3 Ma reveal significant warmer climate in mid- and high-latitude, especially in the northern North Atlantic (~16 K), with the absence of increase in SST in low latitude (e.g., Dowsett et al. 2009). Zonal gradient of SST in low latitude during 3 Ma is also largely different to that in the present-day. Kamae et al. (2011) shows changes in wet/dry climate in low latitude in accordance with the alterations of Hadley/Walker circulation corresponding to the changes in meridional/zonal SST pattern. In comparison to vegetation pattern in present-day, the terrestrial proxy records in 3 Ma indicate; (1) poleward expansion of temperate/boreal forest at the expense of boreal forest and tundra grassland in mid- and high-latitude in accordance with the warmer climate, and (2) expansion of tropical savannas and woodland in Africa, Central Asia, and Australia at the expense of deserts corresponding with moister climate in the semi-arid regions (Salzmann et al. 2008).

Previous studies discussing about responses of geographical patterns of vegetation under 3 Ma climate (e.g., Haywood et al. 2009; Lunt et al. 2009) used reconstructed paleovegetation dataset for Pliocene Research, Interpretation and Synoptic Mapping phase 2 (PRISM2), based on terrestrial proxy records in 74 sites (Thompson and Fleming 1996). Salzmann et al. (2008) archived the new mid-Pliocene (3.6~2.6 Ma) vegetation reconstruction based on proxy data from 202 sites. Though some limitations (see Chapter 5), the state-of-the-art terrestrial proxy data allows us to evaluate the reproducibility of climate modeling for the sustained warmer interval by comparing the dataset with the climate simulated by the numerical climate model predicting the changes in tropical atmospheric circulations and monsoon/desert climate patterns in the lower latitudes. For that purpose, we evaluate the consistency of biomes deduced by BIOME4 model driven by climate parameters simulated in Chapter 3 with the PRISM3 paleovegetation dataset (Salzmann et al. 2008). Results of data-model comparisons and evaluations are shown in Chapter 5.

2. Data and models

2.1 Atmospheric general circulation model (AGCM)

The model used for the present study is an atmospheric component of an air-sea coupled model developed at the Meteorological Research Institute in Japan (MRI-CGCM2.3; Yukimoto et al. 2001, 2006) for climate projections and paleoclimate simulations (e.g., Kitoh et al. 2001; Kitoh and Murakami 2002; Ueda et al. 2011). The AGCM has horizontal T42 resolution (an approximately 280 km transform grid) and 30 layers in the vertical, with the top at 0.4 hPa. The model treats cloud with diagnostic scheme applying different types of relationships between cloud amount and relative humidity depends on convective/layer cloud and land/ocean regions (Yukimoto et al. 2006). For deep moist convection, the Arakawa-Schubert scheme (Arakawa and Schubert 1974) with prognostic closure similar to that of Randall and Pan (1993) is used in the AGCM. The land component is based on the simple biosphere (SiB) model (Sellers et al. 1986; Sato et al. 1989), which includes the effects of vegetation. The land model has three soil layers with different field capacities depending on the vegetation type, in which the temperature, liquid water, and frozen water in each soil layer are predicted. Canopy and grass are treated for each of the 13 vegetation types, for which the parameters are dependent on the vegetation type and month of the year.

2.2 PRISM3 paleoenvironmental dataset

The mid-Pliocene surface conditions used in this study are PRISM3 dataset (Haywood et al. 2010), which combines 202 terrestrial and 86 marine sites. This dataset is provided to the paleoclimate modeling community through a series of digital datasets as part of the PRISM data-model cooperative, also known as the Pliocene Model Intercomparison Project (PlioMIP). The PRISM3 paleoclimate reconstruction contains all major boundary conditions, including SST and sea ice extent (Dowsett et al. 2009b; Haywood et al. 2010), ice sheet height and extent,

vegetation types and distribution (Salzmann et al. 2008), and topography (Sohl et al. 2009).

Figure 2.1a shows estimates of SST by proxy evidences revealing prominent warming in mid- and high-latitude particularly in the northern North Atlantic (~18K; Dowsett et al. 1994, 2009a, Robinson 2009). In contrast, the proxy evidences generally shows that the surface conditions are similar to that in the present-day in low latitude (Dowsett et al. 1994, 1999). The weakening of meridional SST gradient (the greatly warmth in mid- and high-latitude and moderate change of temperature in low latitude) is one of the predominant feature in 3 Ma climate. However, recent improvement of SST reconstruction in the tropics and subtropics revealed that SST in equatorial and coastal upwelling regions was significantly higher than that in the present-day (Herbert and Schuffert 1998; Marlow et al. 2000; Dekens et al. 2007).

Figure 2.1b shows differences in topography and ice sheet height between 3 Ma and the present day. The reconstruction of topography by palaeobotanical and palaeoelevation evidence shows that the East African Rift Valley was 500 m higher in the mid-Pliocene relative to the present value (Thompson and Fleming 1996; Dowsett et al. 1999; Sohl et al. 2009). In contrast, the western cordilleras of North America and northern South America were lower than the present day. Figure 2.2 shows the land ice distribution estimated by stable isotopic, stratigraphic sea level records, and pollen data on the land. This evidence reveals significant reduction of the continental ice sheet on Greenland and Antarctica (Thompson and Fleming 1996; Dowsett et al. 1999). The land ice extent over Greenland was reduced by half (Dowsett et al. 1999), with the ice restricted to the high altitude regions of East Greenland. In East Antarctica, significant ice sheet reduction was recognizable in the Wilkes and Aurora Subglacial basins (Haywood et al. 2010). Figure 2.3 shows sea ice cover estimated by key diatom taxa in Southern Hemisphere (Barron, 1996a, b; Dowsett et al., 1996) and the Arctic region (Robinson 2009; Matthiessen et al., 2009). The estimate of sea-ice reveals seasonally ice-free condition and extreme warm environment in relation to the SST pattern in 3Ma (Haywood et al. 2010).

Figure 2.4 shows reconstruction of vegetation for mid-Pliocene (3.6~2.6 Ma) compiled

from fossil pollen and plant macrofossil data from terrestrial sites covering all continents (Thompson and Fleming 1996; Salzmann et al. 2008). The patterns of reconstructed vegetation in the mid-Pliocene indicate a generally warmer and moister climate relative to the present day. The major differences in vegetation patterns between the modern and the mid-Pliocene are significant reductions of tundra area accompanied by northward migration of evergreen taiga. The vegetation distribution was characterized by a parallel northward shift of temperate forests and grasslands in Eurasian and eastern North America, replacing the boreal conifer forests. In the lower latitude, the mixed warm-temperate forests in East Asia and North America became dominant in central Europe. The northward shift of vegetation patterns in mid- and high-latitude, together with significant reduction of continental ice sheet in Greenland and Antarctica suggests vastly warmer conditions than the present day, particularly at the polar regions (e.g., Salzmann et al. 2008). It is also notable that more humid conditions spread over broader areas in low latitude. Salzmann et al. (2008) revealed a wetter climate in the subtropics relative to the present day due to the expansion of tropical savannas and woodlands in Africa and Australia in the current expense of subtropical deserts.

PRISM3 SST differs from PRISM2 SST (Dowsett et al. 1999) by taking into account data from more localities, particularly in the equatorial Pacific (Dowsett and Robinson 2009) and North-eastern Atlantic/Arctic regions (Dowsett et al. 2009a, b; Robinson 2009). In addition, PRISM3 incorporates multiple temperature proxies (multivariate analysis of fossil planktonic foraminifera, ostracods, and diatoms as well as Mg/Ca and alkenone unsaturation index palaeothermometry) which provide greater overall confidence in the SST fields. The new multiple proxy SST estimates are now greatly enhance and extend the PRISM SST reconstruction into regions previously not represented.

2.3 Equilibrium vegetation model (BIOME4)

The equilibrium biogeography model, BIOME4 (Kaplan et al. 2003), is used to translate

the climate data from the general circulation model (GCM) experiments into vegetation distributions. The model predicts the most-prevailed vegetation types (biomes) as a function of the seasonal cycle of climate parameters by physiological considerations that place constraints on the growth and regeneration of different plant functional types. These constrains are calculated through the use of limiting factors for plant growth, which include mean temperature of the coldest and warmest month, annual minimum temperature, growing degree days (GDD) above 5 and 0 °C, and calculation of a coefficient (Priestley-Taylor coefficient) for the extent to which soil moisture supply satisfies atmospheric moisture demand. GDDs are calculated by linearly interpolated daily temperature from monthly climate data. This approach facilitates comparison of GCM-simulated climate with paleovegetation data, allowing us to assess the regional patterns of simulated climate.

By use of the high-resolution observation-based dataset, the BIOME4 and earlier members of the BIOME model family can reproduce modern natural vegetation well with some minor inconsistencies. Haxeltine and Prentice (1996) revealed the reproducibility of the BIOME model by comparing with natural vegetation map developed by Mellilo et al. (1993). In low latitude, some inconsistency were found in the “Prairie Peninsula” in the midcontinental United State, western coast of South America, southeast Asia and India in accordance with lack of consideration of interannual variability of rainfall, special soil conditions (e.g., extensive iron pans), and very high rates of evapotranspiration. The simulated present-day biomes using BIOME model were, however, generally well-reproducing the natural vegetation in tropics and subtropics. In addition, almost of minor discrepancies in the biome estimates using 28 types of BIOME4 classification are in the same category in the 9 types of MEGABIOME classification (e.g., Haxeltine and Prentice 1996; Kaplan et al. 2003; Wohlfahrt et al. 2008). The BIOME4 model and the MEGABIOME scheme are suitable tools for the present-day natural vegetation and paleovegetation simulations (e.g., Harrison et al. 1998; Kaplan et al. 2003; Haywood et al. 2009).

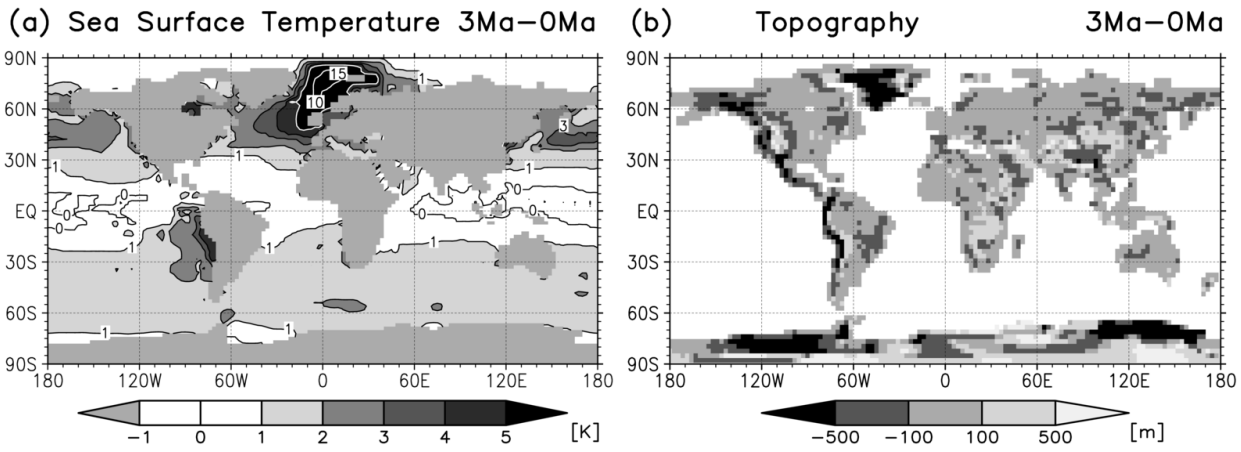

Fig. 2.1. Differences in boundary conditions used in the AGCM (3 Ma minus 0 Ma). (a) Annual mean SST (K). Black and white contour interval is 1, 5 K, respectively. (b) Topography (m).

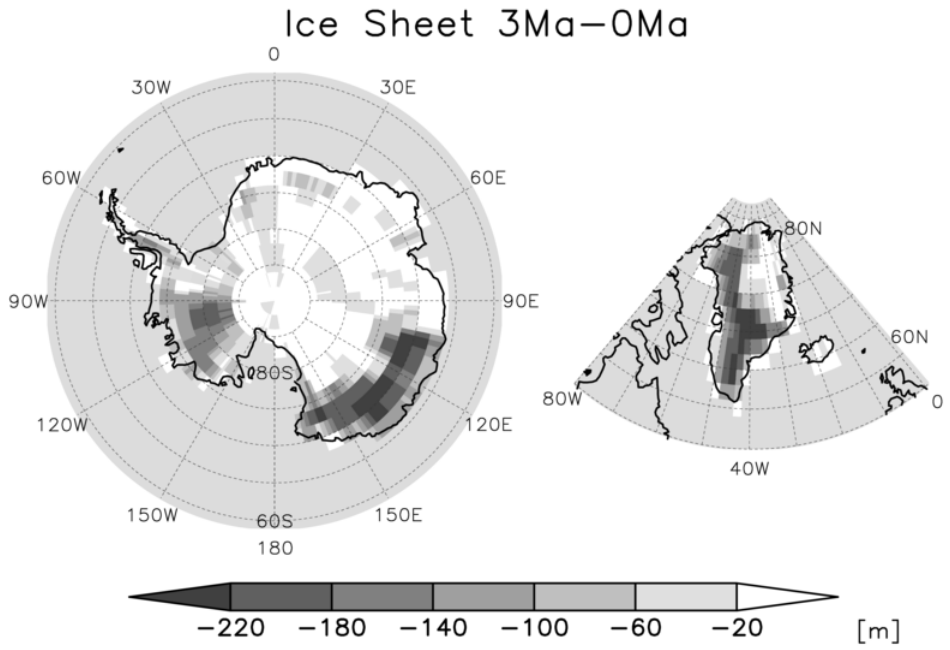

Fig. 2.2. Differences in land-ice extent (m) on Antarctic Continent and Greenland between 3 Ma and 0 Ma.

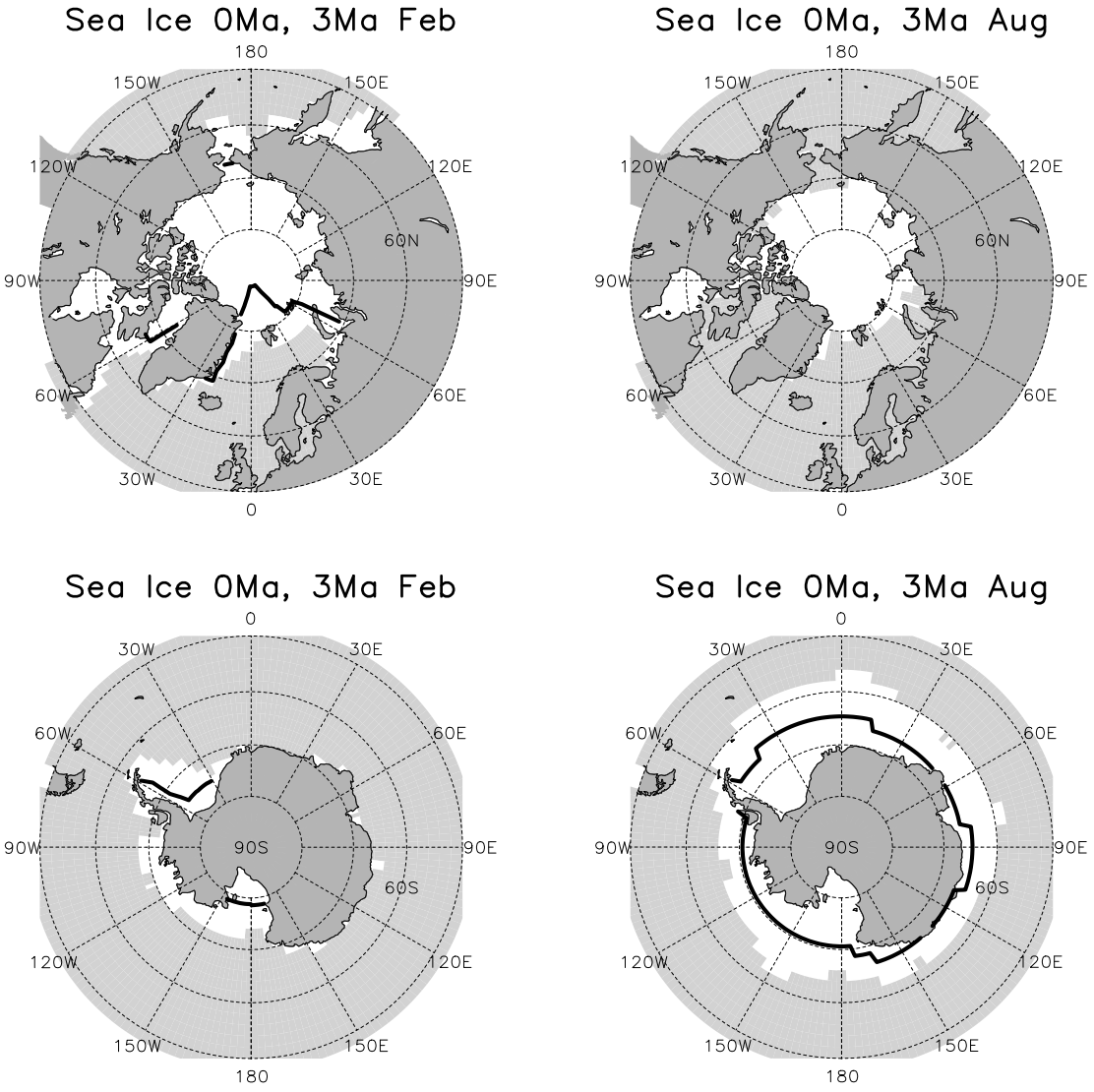

Fig. 2.3. Sea ice covers in Arctic and Antarctic Oceans during 3 Ma and 0 Ma. White shading and black contour represents 0 Ma and 3 Ma, respectively.

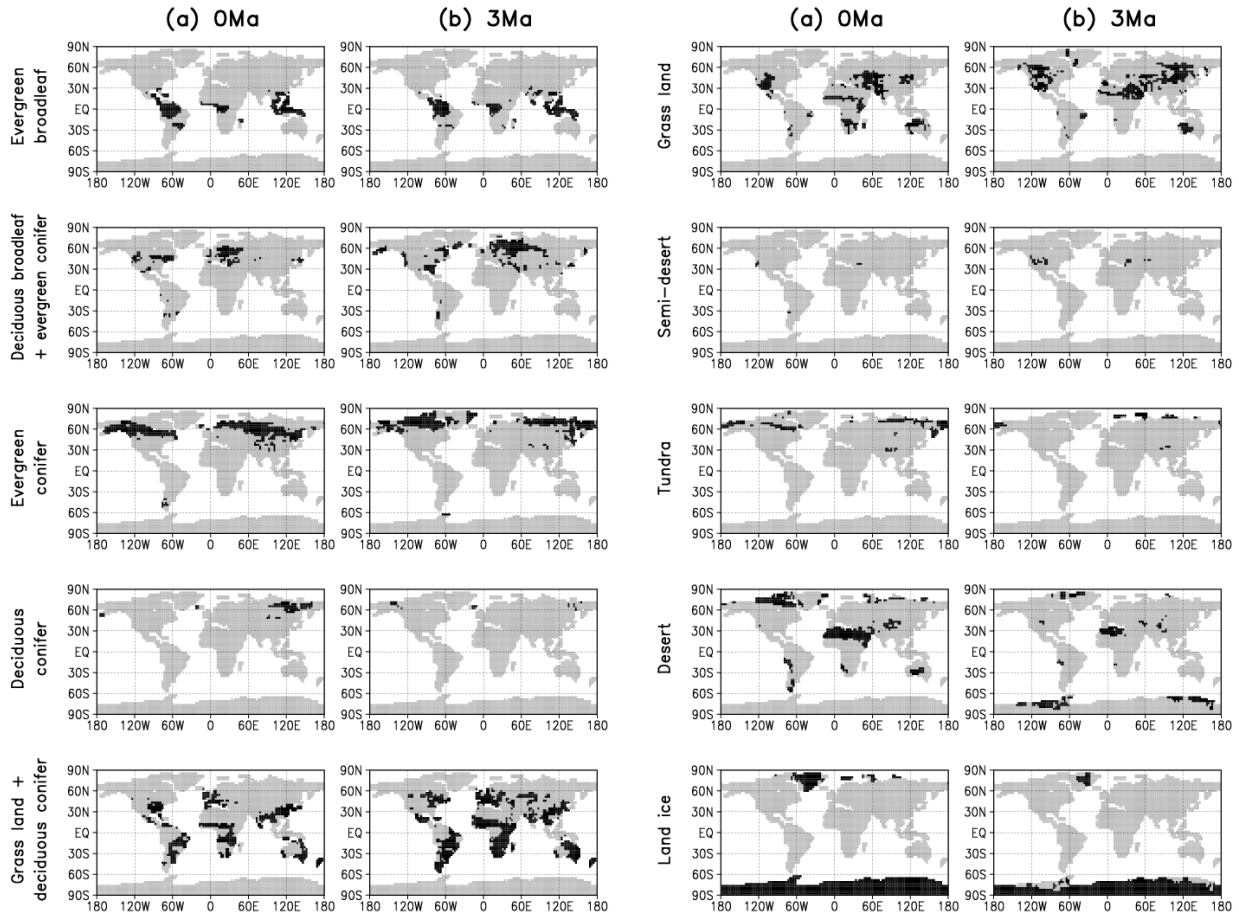

Fig. 2.4. Distributions of vegetation used in the AGCM. (a) 0 Ma, (b) 3 Ma. Vegetation type in each grid is classified into 13 types of SiB classification. Any grids are not classified into three types of vegetation (deciduous broadleaf, broadleaf deciduous shrubs, cultivated land) in this study.

3. Climate simulation during mid-Pliocene warm period

3.1 Experimental designs and methods

3.1.1 3 Ma experiments and sensitivity experiments

Fundamental framework of experimental design for the pre-industrial control run (hereafter, 0 Ma) and the mid-Pliocene simulation (3 Ma) in this study is based on "alternate experiment" in the PlioMIP in which changes in land/sea mask from default setting in climate model are not required, as detailed in Haywood et al. (2010). The experimental settings about atmospheric composition and external forcings in this study are summarized in Table 3.1. The orbital configuration is specified as the same as 0Ma setting. The concentration of CO_2 in the atmosphere was set to 280 and 405 ppmv in 0 Ma and 3 Ma. Note that the setting of atmospheric CO_2 concentration is not greatly important because the prescribed SST already includes surface warming by change in CO_2 concentration in this study. In the absence of any adequate proxy data, all other trace gases were specified to pre-industrial value, as was the solar constant. The details of experimental framework are described in Haywood et al. (2010).

Table 3.2 shows details of seven experiments conducted in this study. The all surface conditions of 0 Ma and 3 Ma experiments are adjusted according to the PRISM3 datasets. Other five sensitivity experiments are designed to investigate the contributions of SST, sea ice, topography, land ice, and vegetation to the mid-Pliocene climate, respectively. The effects of boundary parameters are evaluated as the difference in the result between 3 Ma control experiment and 3 Ma simulation forced by prescribed 0 Ma parameter in this study. For example, the effect of SST is calculated by subtracting the result of 3 Ma_0SST from that of 3 Ma. The basic framework for evaluating the effects of boundary conditions by sensitivity experiments is almost identical to Ueda et al. (2011). To note that the surface warming due to the high-level CO_2 also affect the SST, sea ice, land ice, and vegetation in 3 Ma used in this methodology. All

simulations were run for 60 years and the results reported below are climatological mean for the last 50 years.

3.1.2 Idealized SST experiments

In addition to the sensitivity simulations, we performed three additional idealized experiments summarized in Table 3.3 to investigate more details in the relationship between SST distribution and 3 Ma climate. Figure 3.1 shows the distributions of SST anomaly in boundary conditions for use of the three simulations. Other boundary conditions in the experiments are similar to the 3 Ma simulation. The pattern of SST represented in Fig. 3.1a is the difference of the SST between 3 Ma and 0 Ma boundary conditions (also shown in Fig. 2.1a). Fig. 3.1b shows pattern of zonal-mean SST anomaly between 3 Ma and 0 Ma (hereafter, ZSST). By use of ZSST, we performed "3 Ma_ZSST" simulation to separate contributions of meridional distribution of ZSST and zonal asymmetry in SST difference between 3 Ma and 0 Ma (hereafter, ZASST). The effect of ZSST is determined by subtracting the result of the 3 Ma_ZSST from the result of the 3 Ma_0SST. Fig. 3c and 3d shows difference of SST between 3 Ma and 0 Ma, except for ZSST in the Atlantic Ocean and the Arctic Ocean (AtlZSST) and the Pacific Ocean and the Indian Ocean (PIZSST), respectively. By use of AtlZSST (PIZSST) for boundary condition, 3 Ma_AtlZSST (3 Ma_PIZSST) experiment is performed to evaluate the effect of ZASST in the Pacific Ocean and the Indian Ocean (the Atlantic Ocean) by comparing with the result of 3Ma_ZSST. Note that the zonal-mean SST anomaly in a part of global ocean is computed by averaging in the region (not global) to keep meridional distribution of zonal-mean SST with 3 Ma simulation (Fig. 3.1b).

3.1.3 Indices of Hadley and Walker circulation

As a simple parameter to gauge the intensity of the Hadley circulation, we use the mass stream function (Oort and Yienger 1996) to represent the strength of the mean meridional overturning of mass. This index is defined by calculating the northward mass flux above a

particular pressure level, p. The mass stream function of the MMC Ψ_M is defined as

$$\Psi_M = \frac{2\pi a \cos\phi}{g} \int_0^p [v] dp \tag{3.1}$$

where π is circular constant, a is the radius of the Earth, ϕ is the latitude, g is the gravity acceleration, v is the meridional velocity. The operator [ ] stands for the zonal averaging. The Hadley circulation is described by the two cells (Northern one and Southern one) of Ψ_M in the tropics. The latitudinal extent and centers of the Hadley cells are represented by the absolute value of Ψ_M at 500 hPa became zero and maximum. This index representing the intensity and width of the Hadley circulation was also used in many other studies investigating past, present and future climate changes (e.g., Kitoh and Murakami 2002; Lu et al. 2007; Ohba and Ueda 2010). The Walker circulation is calculated by the divergent component of the zonal wind in the tropics (Yu and Boer 2002; Yu and Zwiers 2010). We define a function Ψ_Z as

$$\Psi_Z = \frac{2\pi a}{g} \int_0^p u_D dp \tag{3.2}$$

where u_D is averaging value of the divergent component of the zonal wind in low latitude (30°S-30°N). The two indices enable us to describe the differences in the planetary scale circulations between the mid-Pliocene and the present day.

3.2 Atmospheric circulation and wetter subtropics in the mid-Pliocene

3.2.1 Precipitation pattern

Primary feature of atmospheric circulation in the mid-Pliocene is found in meridional contrast. Figure 3.2 shows annual-mean differences in surface temperature and precipitation between 3 Ma and 0 Ma simulations. The surface temperature in 3 Ma tends to be higher than 0

Ma in most part of the globe, with 2.1 K warming in global averaging value. Significant warming is evident in mid- and high-latitude in both hemispheres (Fig. 3.2a). The most prominent warming occurring in the high-latitude North Atlantic is about 16 K comparing to the present day. Over the ocean, the surface warming pattern bears considerable resemblance with the distribution of the SST changes (Fig. 3.2a). The increases in the surface temperature in high latitude are corresponding to the area where the sea ice and land ice reduced markedly (Figs. 2.2 and 2.3). In contrast, any substantial changes are not evident in low latitude, except over the tropical eastern Pacific and subtropical North Africa. The east-west gradient in SST over the tropical Pacific are weakened remarkably (~-4 K) because of the increasing (~4 K) /unchanged (~0 K) SST contrast over the tropical eastern/western Pacific (Fig. 3.2a). The surface cooling over subtropical North Africa is attributed to increase in evaporative cooling corresponding with intensification of hydrological cycle on that region (Fig. 3.2d).

The precipitation pattern in low latitude is characterized with decreasing (increasing) on the inside (outside) of the tropical rainfall zone (the area where annual-mean rainfall exceeds 4 mm day^{-1}) in 0 Ma (Fig. 3.2d). For example, precipitation decreases over the tropical Indian Ocean, tropical western Pacific, the equatorial central Pacific, the central South Pacific and the equatorial western Atlantic, and increases over the tropical and subtropical Africa, the Arabian Peninsula, the subtropical South Asia and subtropical Oceania. These patterns reveal that inter-tropical convergence zone (ITCZ) in 3 Ma is broadening and the rainfall accompanying with large-scale convergence in ITCZ is weakening compared to 0 Ma. Although on the inside of the tropical rainfall zone, precipitation also increases over the tropical eastern Pacific and northern South America. The meridional pattern in zonal-mean precipitation anomaly (Fig. 3.2e) displays the rainfall reduction in the center of the ITCZ and rise in the subtropics, indicating meridional expansion of the convergence zone in low latitude. The precipitation pattern in low latitude (30°S-30°N) also represents systematical difference between 3 Ma and 0 Ma (Fig. 3.2f), i.e., increasing at 20°W-70°E (in the western Atlantic, the African continent, and the western

Indian Ocean) and 120°W-60°W (in the eastern Pacific and the South America), and decreasing at 80°E-110°E (in the central-eastern Indian Ocean and Maritime Continent) and 140°E-150°W (in the western-central Pacific). On the outside (inside) of the convergence regions in the tropics, the 3 Ma climate is more rainy (arid) compared to 0 Ma. It is also noteworthy that the simulated wetter condition in the subtropical regions, especially in Africa and Australia, are consistent with the paleoenvironmental reconstructions (Fig. 2.4) by the fossil pollen and plant macrofossil evidences (Salzmann et al. 2008; see Chapter 5).

In order to quantify the change of large-scale circulation in the mid-Pliocene, velocity potential χ is used in this study. The velocity potential field is calculated using the non-rotational horizontal wind vector V_χ at 200 hPa following the definition by Krishnamurti (1971) as:

$$V_\chi = -\nabla\chi \tag{3.3}$$

The change of the velocity potential field in 3 Ma relative to 0 Ma is shown in Fig. 3.3. The general pattern of velocity potential in 3 Ma represents that the anomalous divergent wind flows from the ITCZ to the outside regions in low latitude. The velocity potential is weakened over the western tropical Pacific and the eastern Indian Ocean where the major centers of the divergent circulation implying rising motion in the region are located in 0 Ma (not shown). In contrast, the velocity potential in 3 Ma is strengthen over Africa, the eastern Atlantic, the western Indian Ocean, and the eastern tropical Pacific where the convergence of divergent circulation is dominated in 0 Ma. The east-west pattern of velocity potential in low latitude (Fig. 3.3b) is similar to that of the precipitation in low latitude. The area of the divergent/convergent anomaly in low latitude correspond to the large-scale change of the precipitation pattern increasing at 20°W-70°E (over Africa and the western Indian Ocean) and decreasing at 140°E-150°W (over the western-central Pacific). The changes in velocity potential over the other regions (the eastern Pacific, northern South America, the western Atlantic, and the central-eastern Indian Ocean) are

near zero and the precipitation changes shows complexity in latitudinal structure in low latitude.

The characteristics of atmospheric circulation and hydrological cycle in 3 Ma can be approximated by sum of contributions of each boundary condition. Figure 3.4 shows the precipitation pattern in the 3 Ma simulation and effects of the boundary conditions by the sensitivity experiments (see Section 3.1.1). The precipitation change in 3 Ma (Figs. 3.2d and 3.4a) can be explained by the contribution of SST generally (Fig. 3.4b). As for the other boundary conditions, sea ice, topography, land ice, and vegetation (Figs. 3.4c-f), the contributions to the precipitation pattern in 3 Ma are very little. Only the signal of vegetation effect (Fig. 3.4f) appears as precipitation increase in subtropical North Africa and Arabian Peninsula. The enhanced precipitations in the regions are attributed to decrease in surface albedo and strengthening of atmospheric radiative heating, resulting in favoring convection and increasing precipitation by replacing forest and grassland from desert in those regions (e.g., Charney 1975).

The general figure of the changes in atmospheric circulation and the hydrological cycle in low latitude can be explained by the SST pattern approximately in 3 Ma. Further details in the relationship between the SST distribution and 3 Ma climate are investigated by the three additional idealized experiments (see Section 3.1.2). Each simulation is performed to isolate contribution of ZSST and ZASST in each ocean sector. Figure 3.5 shows effect of each anomalous SST pattern on precipitation. The effect of global SST (Figs. 3.4b and 3.5a), similar to the pattern of 3 Ma simulation (Fig. 3.2d), shows some disagreements with pattern of ZSST effect (Fig. 3.5b). The pattern of increasing in the equatorial eastern Pacific, northern South America, and Africa, and decreasing in the central South Pacific is not evident in the effect of ZSST. The contribution of ZSST is responsible for the latitudinal characteristics of hydrological cycle, while ZSST modifies little the zonal asymmetry in precipitation change. In contrast, the simulation forced by 3 Ma SST in the Pacific Ocean and the Indian Ocean and ZSST in Atlantic (Fig. 3.5c) well reproduce the precipitation pattern in 3 Ma (Fig. 3.2d). Result of simulation (Fig.

3.5d) forced by 3 Ma SST in the Atlantic Ocean and ZSST in the Pacific Ocean and the Indian Ocean (Fig. 3.1d) is not similar to the 3 Ma pattern (Fig. 3.2d). These results explain that ZASST in the Pacific Ocean and the Indian Ocean (Fig. 3.1c) plays a fundamental role for the zonal asymmetry in the precipitation pattern in 3 Ma.

Figure 3.6 shows changes in the velocity potential at 200 hPa in the idealized SST experiments. The SST effect (Fig. 3.6a) reproduces the pattern of 3 Ma change very well which is accompanied by the precipitation change in 3 Ma (Fig. 3.3a). The effect of SST is evident in the increasing of divergent circulation over the eastern Atlantic, Africa, the western Indian Ocean, the eastern tropical Pacific, and the northern South America and the decreasing over the western-central Pacific. The anomalous divergent wind in 3 Ma flows from Africa and northern South America to the major divergent regions in 0 Ma (the eastern Indian Ocean and the Pacific ITCZ). Note that the major divergence over the Bay of Bengal and the eastern Indian Ocean in 0 Ma which represents the intensity of the Asian monsoon is attenuated in 3 Ma. The divergent anomaly over the eastern Atlantic and Africa at the upper level correspond with weakening of the subtropical anticyclone over the Atlantic and Africa at lower level (not shown). The contribution of ZSST for the divergent wind in 3 Ma is also seen over the eastern Indian Ocean and the western Pacific but very restricted in strength and spatial range (Fig. 3.6b). As for the effect of ZASST in the Pacific/Indian Ocean (Fig. 3.6c) and ZASST in the Atlantic Ocean (Fig. 3.6d), the former contributes to the pattern of the SST effect (Fig. 3.6a) rather than the latter. The results explain that the changes of the meridional precipitation pattern in 3 Ma are altered by the change of the meridional gradient in SST, while the precipitation pattern in low latitude and the anomalous convergent/divergent circulations at upper level result from the ZASST in the Pacific Ocean and the Indian Ocean in 3 Ma.

3.2.2 Hadley and Walker circulation

The results of changes in atmospheric circulation patterns shown in the above imply the

existence of general modification of atmospheric overturning circulation in the mid-Pliocene relative to the present day. Figure 3.7 shows zonal-mean atmospheric meridional circulation (e.g., Hadley circulation in the tropics) and east-west overturning circulation in low latitude (Walker circulation), defined by Eqs. (3.1) and (3.2). Increasing (decreasing) values over the negative (positive) circulation in 0 Ma climatology represent slow-down of circulation in 3 Ma. The Hadley circulation (Figs. 3.7a and 3.7c) weakens (up to ~30 %) in center of region where deep convection pronounces (10°S-15°N) in the tropics. As for the poleward boundaries of the Hadley cells, around 30°S and 30°N, the circulations are strengthened, indicating poleward widening of the Hadley cells. More evident tendency of latitudinal expansion is appeared in the ascending branches in the Hadley circulation, defined as the range between equator boundary and center of circulation at 500 hPa constant-pressure surface (Fig. 3.7c). The width of the ascending branches in the northern and southern cells in 0 Ma (3 Ma) are 7.9° (8.9°) and 19.7° (21.5°) latitude, respectively. The ascending branches in the northern and southern cells extend by about 1.0° and 1.8° latitude in 3 Ma relative to 0 Ma. Both of these expansions are much larger than the interannual variability in 0 Ma (0.3° and 0.9° latitude in the northern and the southern cells, respectively). The weakening of upward motion together with the broadening of ascending branches in the Hadley circulation is concurrent with the expanding of the tropical rainfall zone and the precipitation decreasing on the inside of the area (Fig. 3.2e).

Figure 3.7b shows the Walker circulation defined by the east-west component of divergent wind integrating vertically in low latitude (Eq. 3.2). The annual-mean Walker circulation in the present-day observed climatology has three major components (e.g., Hastenrath 1991; Peixoto and Oort 1992): 1) a cell ascending in the tropical western-central Pacific and descending in the eastern Pacific (Pacific Ocean cell), 2) ascending in the maritime continent, and descending in the western Indian Ocean (Indian Ocean cell), and 3) ascending in the African continent and descending in the western Atlantic (Atlantic Ocean cell). In the simulation, the Atlantic Ocean cell is represented unclearly because of conjunction of the east-west overturning circulation over

South America, Atlantic, and Africa in low latitude. Boundary between the two cells over the Indian Ocean and the Atlantic Ocean is not apparent because they merge over the western Indian Ocean. The zonally-asymmetric overturning circulations are generally weakening in 3 Ma, especially in the Pacific Ocean cell (up to ~30 %) and the Indian Ocean cell (up to ~66 %). The weakening of the Walker cells is attributed to the diminishing of east-west SST contrast in the tropics (Fig. 1a). The characteristics of east-west overturning circulation in 3 Ma are highly correlated with the precipitation changes in low latitude (Figs. 3.2d and 3.2f). The slow-down of the ascending motion, between the centers of the weakened Indian Ocean cell and Pacific Ocean cell (40°E-160°W), corresponds with the attenuated precipitation area in the tropical eastern Indian Ocean and the tropical western-central Pacific. In addition, the area where the precipitation increases, in the tropical eastern Pacific and the African continent, is located in the area between the centers of the weakening cells (160°W-40°E) where the large-scale descending motion is suppressed.

Figure 3.8 shows contributions of 3 Ma SST (Fig. 3.8a), ZSST (Fig. 3.8b), global SST and ZSST in Pacific and Indian Ocean (Fig. 3.8c), and global SST and ZSST in Atlantic (Fig. 3.8d) for the changes in Walker circulation. The characteristics of Walker circulation in the 3 Ma simulation (Fig. 3.7b), generally weakening of the cells in Pacific and Indian Ocean, are well reproduced by the global SST effect (Fig. 3.8a). These changes in Walker circulations are not evident in result of ZSST effect (Fig. 3.8b). Contrastingly, effect of ZASST in Pacific and Indian Ocean to Walker circulation (Fig. 3.8c) is quite similar to the SST effect (Fig. 3.8a), but that in Atlantic Ocean (Fig. 3.8d) is moderate. These facts indicate that the change of zonal overturning circulation in tropical atmosphere in 3 Ma is induced by ZASST anomaly, especially in Pacific and Indian Ocean.

Figure 3.9 shows longitudinal distribution of velocity potential at 200 hPa in low latitude (30°S-30°N) in the idealized SST experiments. The anomalous east-west divergent contrast in 3 Ma (divergent at 20°W-70°E and convergent at 140°E-150°W) corresponds with the weakening

of the Indian Walker cell and the Pacific Walker cell (Fig. 3.7b). The divergent anomaly over Africa and the convergent anomaly over the western-central Pacific are not reproduced by ZSST and ZASST in the Atlantic Ocean sufficiently but contributed by ZASST in the Pacific Ocean and the Indian Ocean, as shown in Fig. 3.9. These results are consistent with the fact that the amplitude of ZASST in the Pacific Ocean is much greater (~4.0 K) than in the Indian Ocean (~0.5 K) and in the Atlantic Ocean (~0.5 K). The idealized experiment above reveals that the major factor contributing the weakening of the Walker circulation over the Indian Ocean and the Pacific Ocean accompanied by the zonal asymmetric change of the precipitation pattern in 3 Ma is ZASST in the Pacific Ocean and the Indian Ocean.

The atmospheric meridional circulation in low latitude is closely correlated to the change in the meridional gradient of SST. Figure 3.10 shows the changes in latitudinal ranges of the ascending branch in the Hadley circulation simulated by the idealized SST experiments. All of the latitudinal distributions of zonal-mean SST in the simulations (3 Ma, 3 Ma_ZSST, 3 Ma_AtlZSST, and 3 Ma_PIZSST) are the mid-Pliocene pattern. The Hadley cells in both hemispheres are expanding in the simulations using by SST with the 3 Ma latitudinal distributions of zonal-mean value. The broadening in southern cell is larger than that in northern cell in each simulation. The extending is largest in the simulation forced by global ZSST (1.3° and 2.4° latitude in the northern and the southern cells, respectively). In either case, the broadenings of ascending branches in the Hadley cells are larger than interannual variability in the 0 Ma simulation. This result reveals that the latitudinal range of ascending branch in the Hadley cells expand in response to the weakening of the meridional gradient of SST in 3 Ma, either zonally uniform or nonuniform.

3.3 Discussions

3.3.1 Wetter climate in subtropical Africa

In this study, the wetter surface condition in the subtropical Africa during the mid-Pliocene which is also suggested by the fossil pollen data is reproduced. Plio-Pleistocene climate change and onset of aridity in the subtropics (e.g., deMenocal 1995; McLaren and Wallace 2010) had an essential role in the transition of regional paleoenvironmental conditions and evolutions of flora and fauna, including Hominids. The climate of subtropical North Africa shifted from wetter to dryer condition gradually in late Cenozoic (e.g., Axelrod and Raven 1978; Leroy and Dupont 1994) and begun to perturb between dry and humid climate during the glacial-interglacial cycle corresponding to the fluctuation of summer insolation in the Northern Hemisphere high latitude (e.g., Prell and Kutzbach 1987), the northern glaciations, and the cooler North Atlantic SST (e.g., deMenocal and Rind 1993; deMenocal et al. 2000). The wetter conditions in subtropical Africa and Australia (Fig. 3.2d) reproduced in this study are mainly contributed by the pattern of SST rather than orography, land ice, sea ice, and vegetation in this interval (Fig. 3.4) through the alternation of the atmospheric circulation pattern (Fig. 3.3) associated with the expansion of the ascending branch of the Hadley circulation (Figs. 3.7a, 3.7c, and 3.10) and the slow-down of the Walker circulation (Figs. 3.7b and 3.9). This study represents the importance of the diminishing of the meridional and zonal SST gradient in low latitude for the moister climate in the subtropical Africa during the mid-Pliocene greenhouse world.

3.3.2 Differences in the atmospheric structure with the global warming projection

The meridional-vertical structure of the tropical atmosphere is key factor for interpreting the modulation of the atmospheric circulation (e.g., Held and Soden 2006) and climate feedback system (e.g., Soden and Held 2006) under the projected warmer condition. Although the mid-Pliocene climate is often cited as an analog for the warmer climate, the characteristics in the simulation of the atmospheric circulation show several differences to those in the future projections. Figure 3.11 shows latitude-vertical cross section of zonal-mean air temperature and specific humidity. Low- and mid-tropospheric air temperature in 3 Ma rises significantly in mid-

and high-latitude and changes slightly in low latitude (Fig. 3.11a). The peaks of the atmospheric warming in troposphere (~8 K) are mainly found at near surface in high latitude regions. This pattern is different from the projected climate change forced by increasing of atmospheric greenhouse gases concentrations in which the peaks are appeared at upper-troposphere in low latitude corresponding with the intensification of condensational heating (e.g., Meehl et al. 2007; Lu et al. 2008). Note that the tropical precipitation in the 3 Ma simulation does not increase relative to 0 Ma (Fig. 3.2e). Contrasting to the troposphere, temperature in the stratosphere rises in the tropics and falls in mid- and high-latitude in 3Ma simulation. In the CO_2-rich climate, Manabe and Wetherald (1967) revealed that intensification of radiative cooling lead to temperature drop in the stratosphere by use of one-dimensional radiative-convective equilibrium model. The stratospheric cooling simulated in the 3 Ma experiment is attributed to the rise of CO_2 concentration in the atmosphere (Table 1). The latitudinal contrast is also evident in the zonal-mean specific humidity (Fig. 3.11b). The specific humidity increases in the lower troposphere corresponding to the near-surface warming and decreases in the lower and mid-troposphere over the equatorial region. This represents weakening of atmospheric upward motion and vertical transport of water vapor in the tropics. The atmospheric moisture pattern is accompanied with the decreasing (increasing) of precipitation on the inside (outside) of the tropical rain band (Figs. 3.2d and 3.2e).

The weakening of atmospheric upward motion in the tropics also affects atmospheric vertical structure in the upper troposphere. Figure 3.12 shows tropopause height in 0 Ma and 3 Ma, calculated by the algorithm of Reichler et al. (2003) and the World Meteorological Organization (1957) (Lu et al. 2007). In low latitude, the tropopause moves downward (~5 hPa) in 3 Ma compared to 0 Ma, and in contrast to the upward shift in the future warming simulation (Lu et al. 2008). The downward shift of the tropopause in the tropics corresponds with the weakening of atmospheric upward motion, resulting in stratospheric cooling (Fig. 11a) because atmospheric temperature begins to decrease above the tropopause level. The tropopause height

outside of the tropics shifts upward, indicating poleward broadening in the characteristics of the tropical climate. The general figure of the surface conditions reconstructed by the proxy is similar to that of the global warming simulations in the aspects of mid- and high-latitude warming and El-Niño like pattern in the tropics. This work, however, shows that the zonal-mean structure of the 3 Ma atmosphere in low latitude differs from that in the future projection.

3.3.3 Limitations of discussions – SST formation in the mid-Pliocene

It should be noted that formation processes of the tropical SST pattern during the mid-Pliocene warm period were not discussed in this study because the results were derived from the AGCM experiments prescribing the sea-surface conditions (see Section 3.1.1). Many studies have tried to improve the interpretation as to the formation and maintenance of the SST pattern in the pre-Quaternary through high latitude (ice-albedo feedback and thermohaline circulation; e.g., Crowley 1996; Robinson 2009; Etourneau et al. 2010; Steph et al. 2010) and tropical (air-sea interaction and ocean upwelling) perspectives (e.g., Philander and Fedorov 2003; Fedorov et al. 2006; Ravelo 2010). Recently, it is also found that ocean vertical mixing by tropical cyclone activities in the warmer world has an important role in the SST pattern during the early Pliocene (Fedorov et al. 2010). Further effort in improving the understanding of the control factors for mid-Pliocene sea surface condition could benefit the prediction of climate in the future greenhouse world.

3.4 Summary

The recent improvement of SST reconstruction obtaining the new proxy records, particularly in the tropical Pacific, made significant advancement in the reproducing of the pattern of the atmospheric circulation in the mid-Pliocene. The PRISM3 boundary condition containing the detailed information about east-west contrast in tropical oceans used in this study enable us to describe more systematical pattern in the atmospheric circulation. The weakening of

meridional gradient in SST suppresses the intensity of the Hadley circulation and broadens the ascending branches of the Hadley cells. The expansion of the ascending area in low latitude produces wetter climate to the wider regions, including subtropical Africa and Australia. The weakening of the east-west gradient of SST in the tropics, particularly in the Pacific Ocean and the Indian Ocean, corresponds with the slow-down of the Walker circulation and modifies the precipitation pattern in low latitude. Further efforts for the improvement of the SST reconstruction during the mid-Pliocene in the tropics may help investigating the detailed aspects of the sustained warmer climate.

The equilibrium warm climate for sustained time period (~300 thousand years) is compared to the present day condition in this study. The mid-Pliocene climate also perturbed corresponding with the fluctuation of orbital configuration amplifying the interactions between climate subsystems (e.g., Philander and Fedorov 2003; Fedorov et al. 2006) or closure of Oceanic gateways (e.g., Haug and Tiedemann 1998; Bartoli et al. 2005; Lunt et al. 2008a; Steph et al. 2010) and gradually shifted to the Quaternary climate. The details of the processes of the transitions should be investigated by GCMs coupled with Ocean and other subsystems (e.g., ice sheet and vegetation) with numerous kinds of experimental configurations. As this work focuses on the climate change in low latitude, the extent and volume of the sea ice and land ice are not discussed enough. However, the fluctuations of the arctic sea ice, ice sheet extent in high latitude, and intensity of Atlantic meridional overturning circulation are the hot topics for the comparison with the Quaternary and the future climate changes. The proxy data in the high latitude North Atlantic, Arctic region, and deep sea in the Atlantic has been investigated recently (e.g., Billups et al. 1997; Knies et al. 2002; Cronin et al. 2005; Poore et al. 2006; Dowsett et al. 2009b; Robinson 2009). It may help progressing of future works researching about comprehensive figure of the mid-Pliocene climate system.

In this study, only the annual-mean values are considered to investigate the features of the atmospheric global circulation in the mid-Pliocene. However, the seasonal or interannual

characteristics in the mid-Pliocene climate also have much significance for how the climate system in the sustained warm period is formed and sustained. Particularly, comparison of the global monsoon system between in the glacial-interglacial period and in the mid-Pliocene is one of important remaining subjects. The attenuated precipitation over the eastern Indian Ocean and Bay of Bengal, attributing to weakening of Asian summer monsoon, corresponds to the increase in subtropical North Africa and Arabian Peninsula. The precipitation pattern is suggestive of negative monsoon-desert mechanism (Rodwell and Hoskins 1996) which is worthwhile issue by investigating seasonal aspect of the climate. More detailed studies about modification of the West African monsoon and the South African monsoon could help to capture comprehensive figure about formation of the wetter African climate in the mid-Pliocene.

Table 3.1. External forcings and atmospheric constituents in this study.

Solar constant [W m^{-2}]	Eccentricity	Obliquity [°]	Precession [°]	CO_2 (0 Ma) [ppmv]	CO_2 (3 Ma) [ppmv]	CH_4 [ppbv]	N_2O [ppbv]
1365	0.016724	23.446	102.04	280	405	760	270

Table 3.2. Surface properties for the experiments. Spatial range where difference in topography and vegetation exists between 3 Ma and 0 Ma is the globe except the Greenland and the Antarctic Continent. Differences of "Land ice" in orography and biomes between 3 Ma and 0 Ma exist only on the Greenland and the Antarctic Continent.

Experiments	SST	Sea ice	Topography*	Land ice**	Vegetation*
0 Ma	**0 Ma**	**0 Ma**	**0 Ma**	**0 Ma**	**0 Ma**
3 Ma	3 Ma	3 Ma	3 Ma	3 Ma	3 Ma
3 Ma_0SST	**0 Ma**	3 Ma	3 Ma	3 Ma	3 Ma
3 Ma_0Sea ice	3 Ma	**0 Ma**	3 Ma	3 Ma	3 Ma
3 Ma_0Topo	3 Ma	3 Ma	**0 Ma**	3 Ma	3 Ma
3 Ma_0Land ice	3 Ma	3 Ma	3 Ma	**0 Ma**	3 Ma
3 Ma_0Veg	3 Ma	3 Ma	3 Ma	3 Ma	**0 Ma**

*except the Greenland and the Antarctic Continent
**only on the Greenland and the Antarctic Continent

Table 3.3. SST configurations in the idealized experiments. The other boundary conditions in the experiments are similar to the 3 Ma simulation. The configurations in the two contrast experiments are shown in the upper column.

Experiments	SST in the Pacific Ocean and the Indian Ocean	SST in the Atlantic Ocean and the Arctic Ocean
3 Ma	3 Ma	3 Ma
3 Ma_0SST	0 Ma	0 Ma
3 Ma_ZSST	3 Ma zonal	3 Ma zonal
3 Ma_AtlZSST	3 Ma	3 Ma zonal
3 Ma_PIZSST	3 Ma zonal	3 Ma

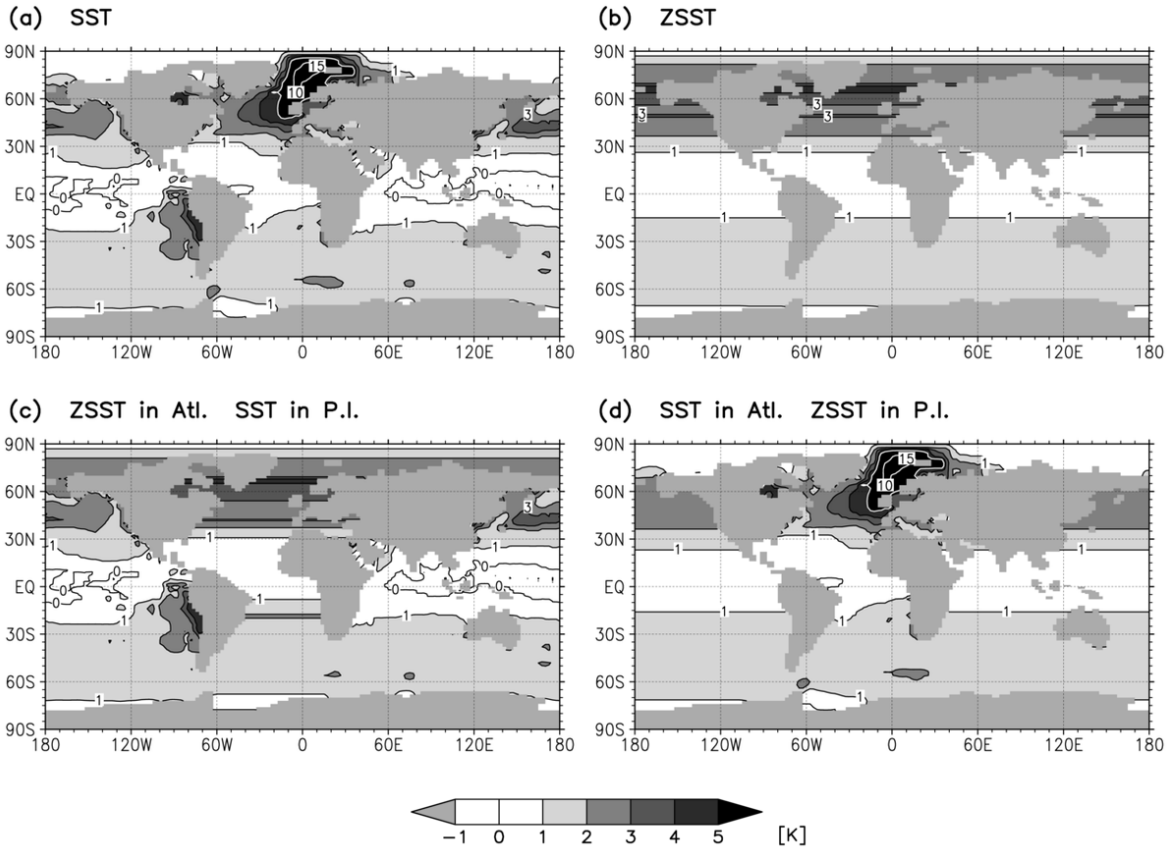

Fig. 3.1. Differences in annual mean SST (K) between idealized SST experiments and 0 Ma. (a) 3 Ma (same as Fig. 2.1a), (b) 3 Ma_ZSST (zonal-mean SST in globe), (c) 3 Ma_AtlZSST (same as Fig. 3.1a but for zonal SST in the Atlantic Ocean), (d) 3 Ma_PIZSST (same as Fig. 3.1a but for zonal SST in the Pacific/Indian Ocean). Boundaries between the Southern Atlantic Ocean and the Southern Pacific/Indian Ocean (22.5°E, 67.5°W) are smoothing with neighboring grids.

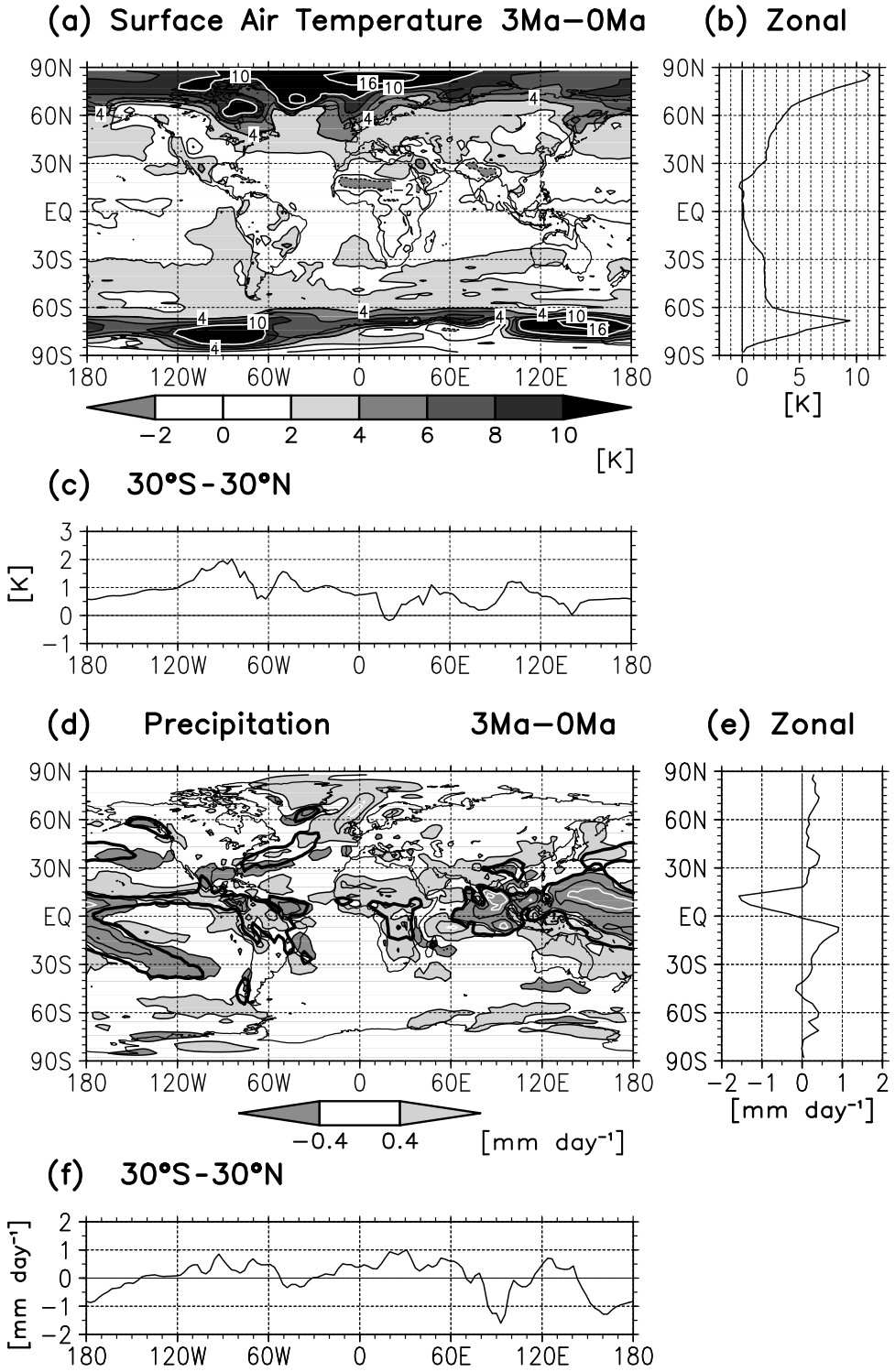

Fig. 3.2. Differences in the annual mean value between 3 Ma and 0 Ma. (a) Surface air temperature (K). Black and white contour interval is 2 and 6 K, respectively. (b) Zonal mean of surface air temperature anomaly. (c) Low latitude (30°S−30°N) surface air temperature anomaly. (d) Precipitation (color shading in mm day^{-1}). Thin black contour represents ±0.4, ±2 mm day^{-1} and white contour interval is 4 mm day^{-1} in precipitation change. Solid black contour represents 4 mm day^{-1} in 0Ma precipitation. (e) Zonal mean of precipitation anomaly. (f) Low latitude (30°S−30°N) precipitation (mm day^{-1}) anomaly.

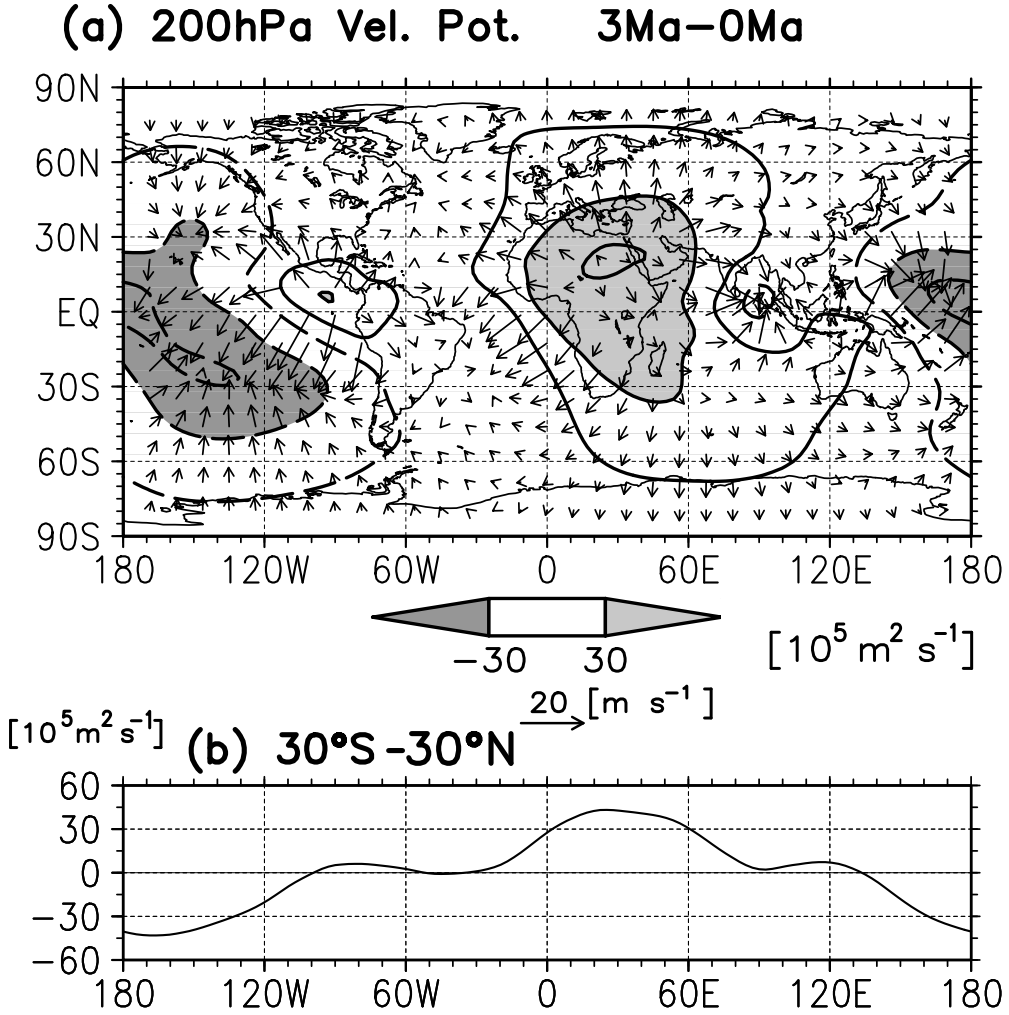

Fig. 3.3. Differences in the annual mean value between 3 Ma and 0 Ma. (a) Velocity potential at 200 hPa (contour in 10^5 m^2 s^{-1}) and divergent wind at 200 hPa (vector in m s^{-1}). Contour interval is 20 × 10^5 m^2 s^{-1}. (b) Low latitude (30°S−30°N) velocity potential at 200 hPa (10^5 m^2 s^{-1}) anomaly.

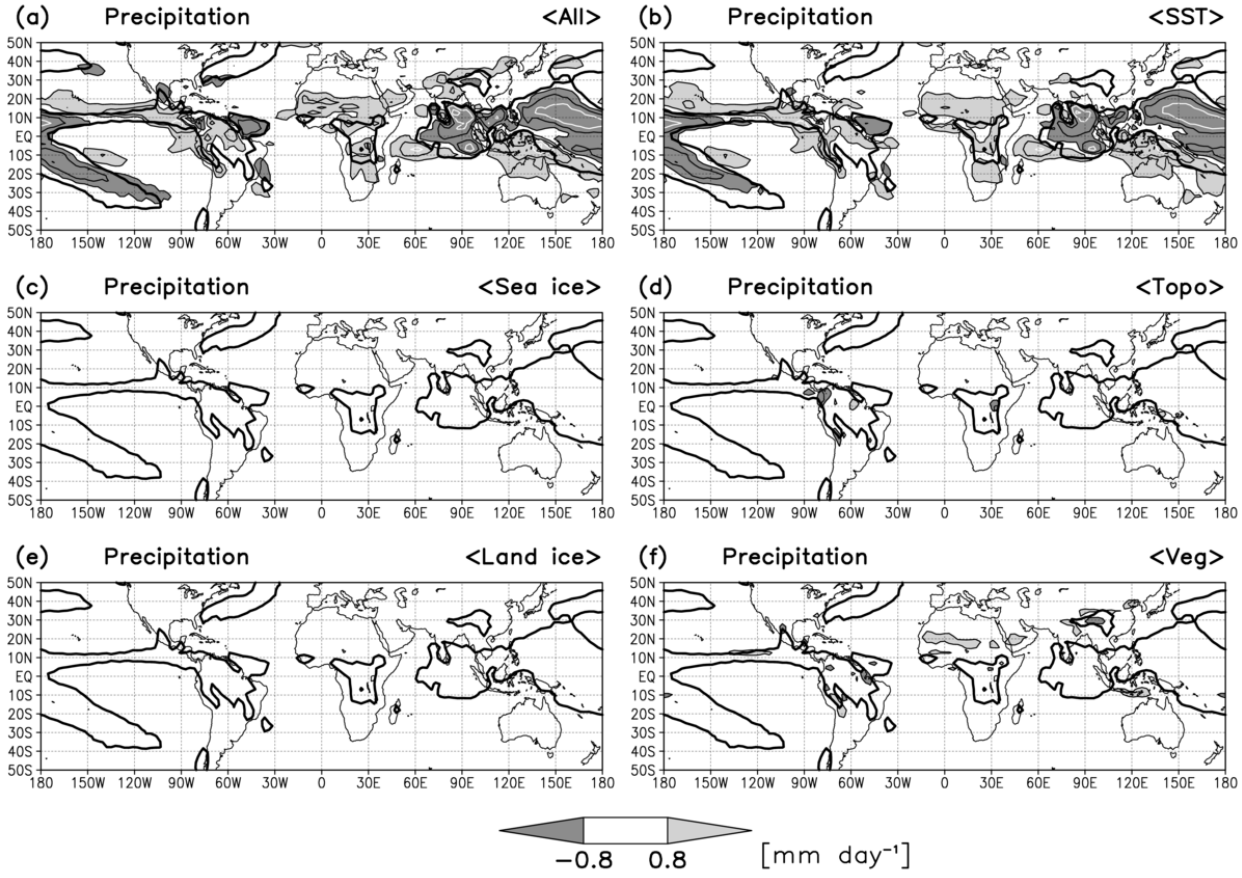

Fig. 3.4. Changes in the annual mean precipitation (mm day^{-1}). (a) Difference between 3 Ma and 0 Ma (same as Fig. 3.2d). (b) Effect of SST, (c) sea ice, (d) topography, (e) land ice, (f) vegetation. Thin black contour represents ±0.8, ±2 mm day^{-1}, white contour interval is 4 mm day^{-1} with the zero contours omitted for clarity. Solid black contour represents 4 mm day^{-1} in climatological value in 0 Ma.

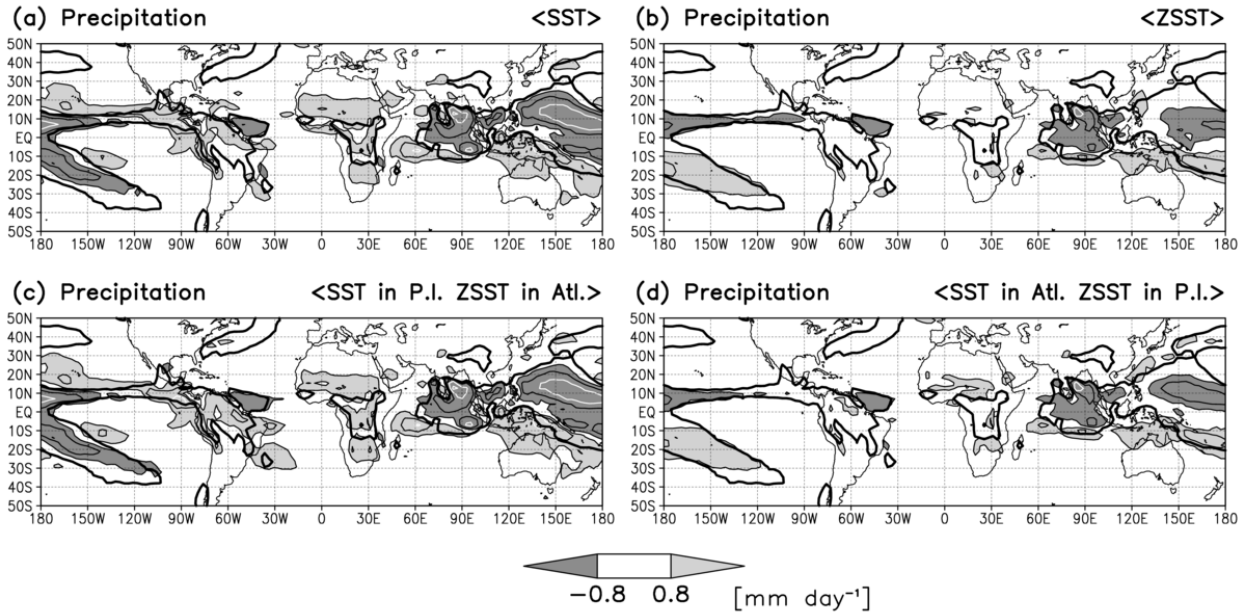

Fig. 3.5. Same as Fig. 3.4, but for the idealized SST experiments. (a) Effect of 3 Ma SST in the globe (3 Ma minus 3 Ma_0SST, same as Fig. 3.4b). (b) Effect of 3 Ma zonal-mean SST (ZSST) in the globe (3 Ma_ZSST minus 3 Ma_0SST). (c) Effect of 3 Ma SST in the Pacific/Indian Ocean and ZSST in the Atlantic Ocean (3 Ma_AtlZSST minus 3 Ma_0SST). (d) Effect of 3 Ma SST in the Atlantic Ocean and ZSST in the Pacific/Indian Ocean (3 Ma_PIZSST minus 3 Ma_0SST).

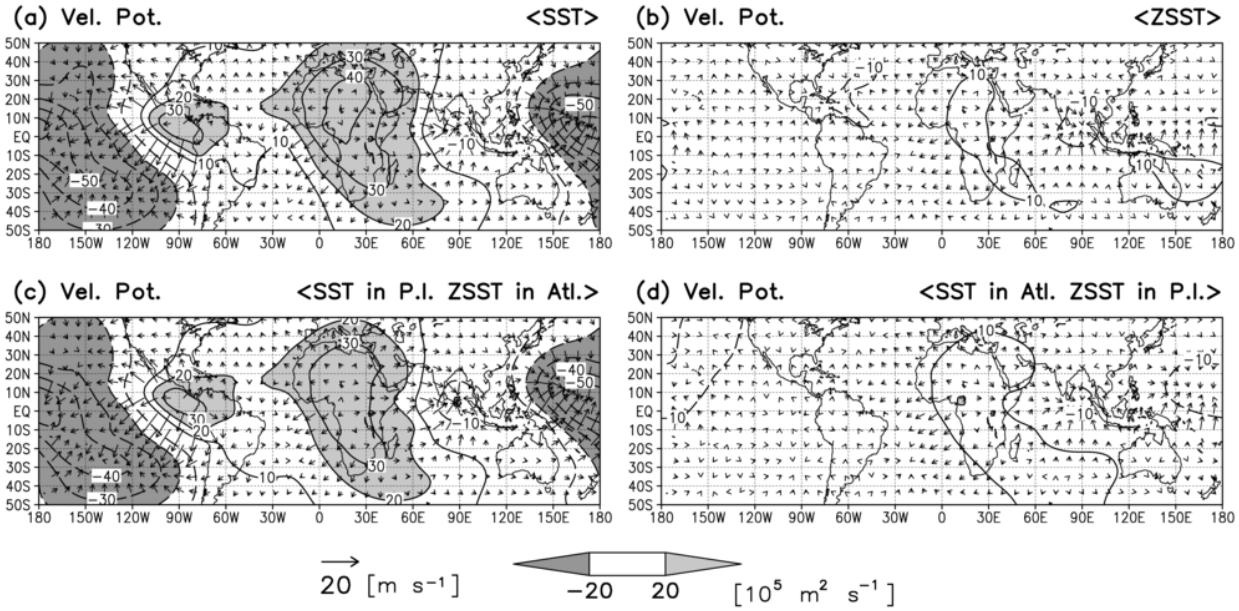

Fig. 3.6. Same as Fig. 3.5, but for velocity potential (shading and contour in 10^5 m^2 s^{-1}) and divergent wind (vector in m s^{-1}) at 200 hPa. Contour interval is 10×10^5 m^2 s^{-1} with the zero contours omitted for clarity. Solid (dashed) contour represents positive (negative) change.

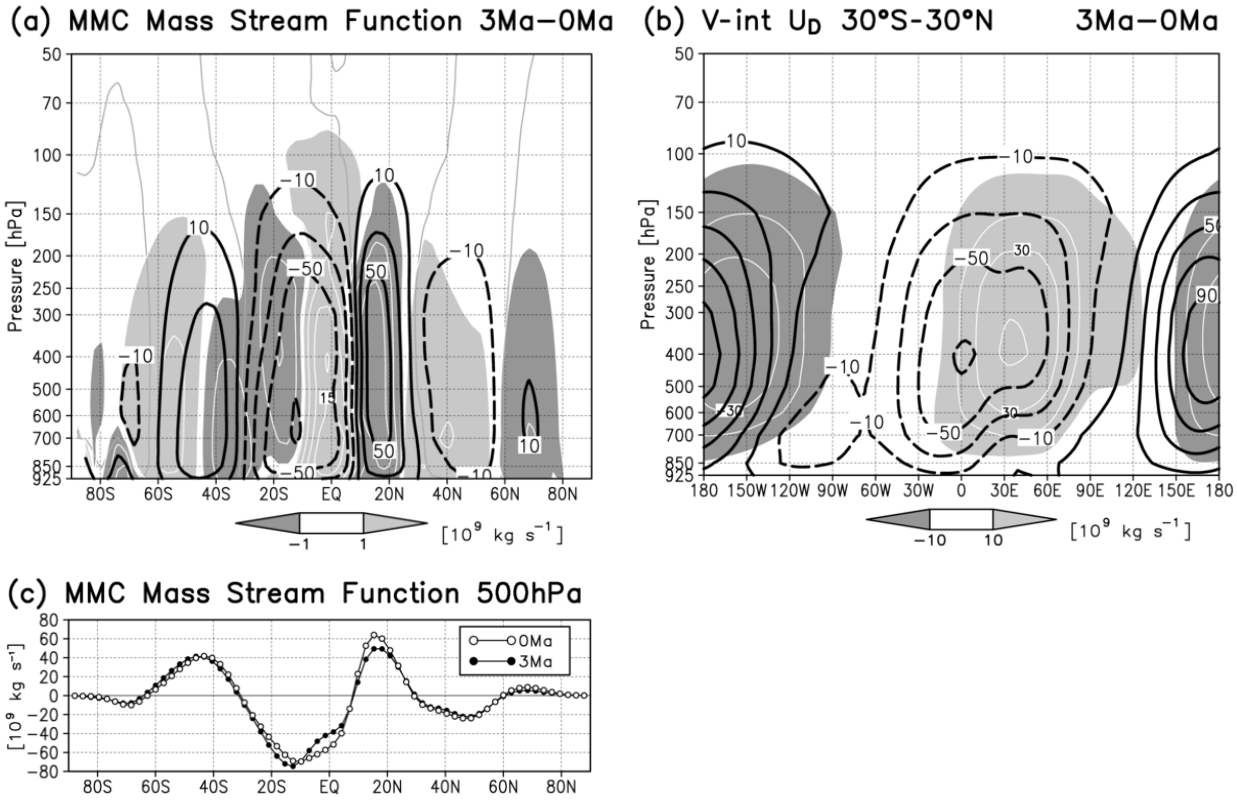

Fig. 3.7. (a) Mass stream function (10^9 kg s^{-1}) of the annually averaged mean meridional circulation (MMC). Black and grey contour represents climatological value in 0 Ma (black contour interval is 20 × 10^9 kg s^{-1}, grey contour is 0 kg s^{-1}). Shading and white contour represents difference between 3 Ma and 0 Ma. Contour interval is 5 × 10^9 kg s^{-1}. (b) Vertically integrated east-west component of annual-mean divergent wind averaged over 30°S-30°N (10^9 kg s^{-1}). Black contour represents climatological value in 0 Ma. Contour interval is 20 × 10^9 kg s^{-1}. Shading and white contour represents difference between 3 Ma and 0 Ma. Contour interval is 10 × 10^9 kg s^{-1}. (c) Latitudinal distribution of the MMC mass stream function (10^9 kg s^{-1}) at 500 hPa in 0 Ma (open circle) and 3 Ma (filled circle).

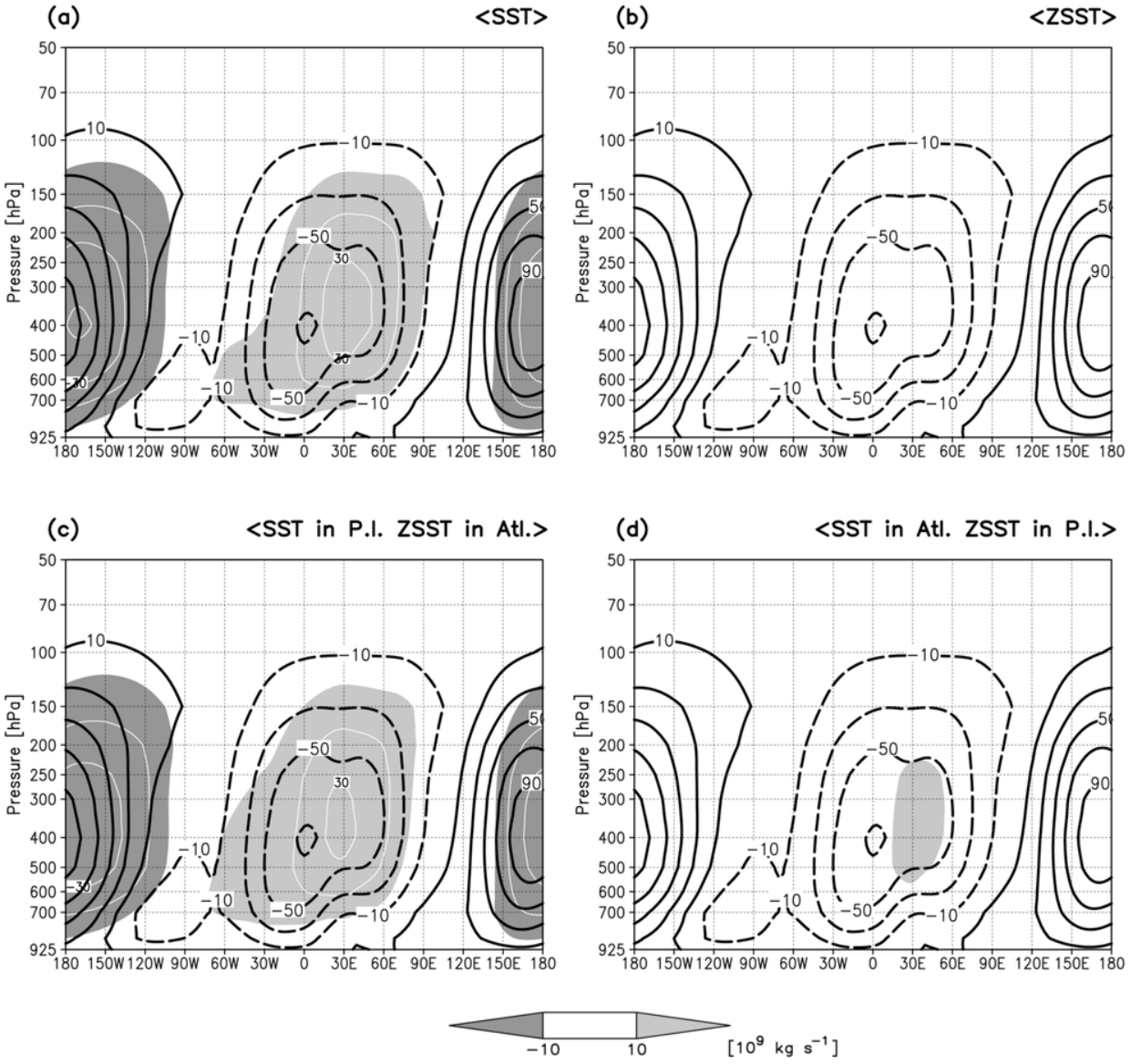

Fig. 3.8. Same as Fig. 3.7b, but for the idealized SST experiments. (a) Effect of 3 Ma SST in the globe (3 Ma minus 3 Ma_0SST). (b) Effect of 3 Ma zonal-mean SST (ZSST) in the globe (3 Ma_ZSST minus 3 Ma_0SST). (c) Effect of 3 Ma SST in the Pacific/Indian Ocean and ZSST in the Atlantic Ocean (3 Ma_AtlZSST minus 3 Ma_0SST). (d) Effect of 3 Ma SST in the Atlantic Ocean and ZSST in the Pacific/Indian Ocean (3 Ma_PIZSST minus 3 Ma_0SST).

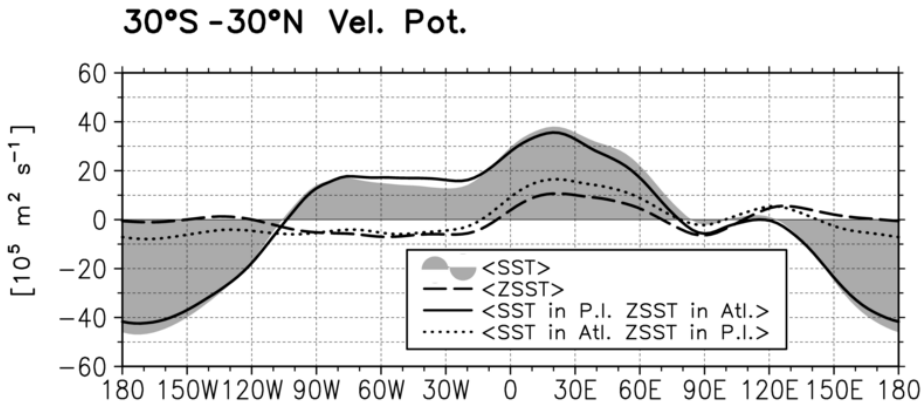

Fig. 3.9. Low latitude (30°S−30°N) annual mean velocity potential at 200 hPa (10^5 m^2 s^{-1}). Shading is the effect of 3 Ma SST in the globe. Dashed line is the effect of ZSST in the globe. Solid line is the effect of 3 Ma SST in the Pacific/Indian Ocean and ZSST in the Atlantic Ocean. Dotted line is the effect of 3 Ma SST in the Atlantic Ocean and ZSST in the Pacific/Indian Ocean.

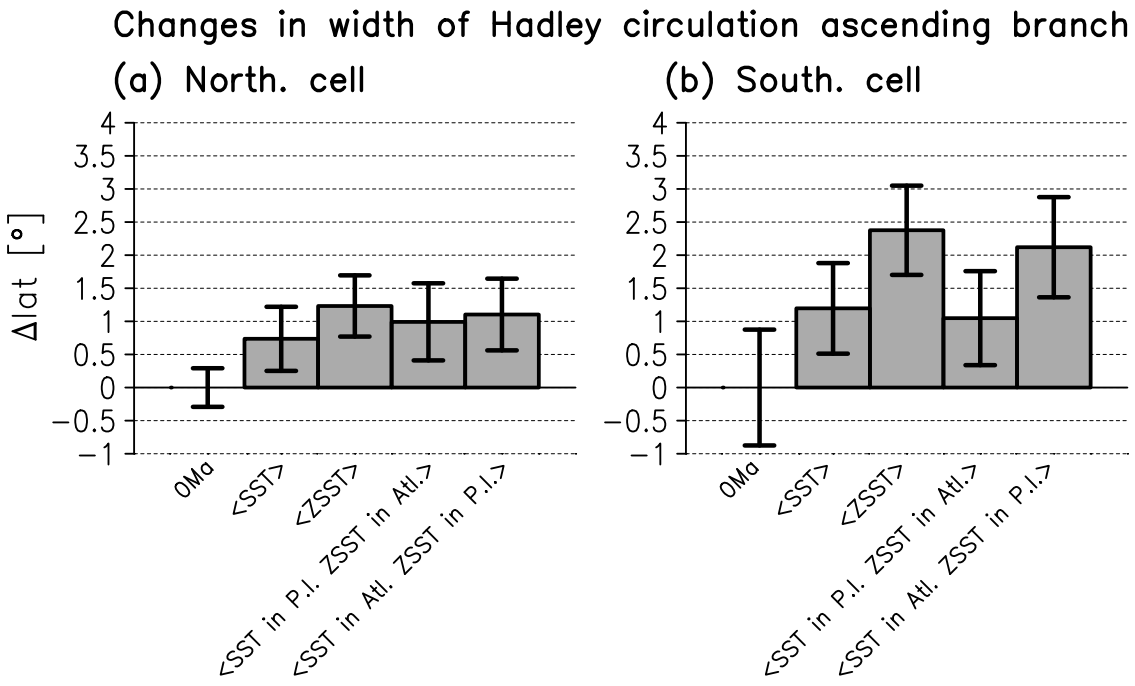

Fig. 3.10. Changes in latitudinal range (°) of Hadley circulation ascending branch. Positive (negative) value represents expanding (shrinking) of the range. (a) Northern cell, (b) southern cell. Error bars indicate standard deviations in each run.

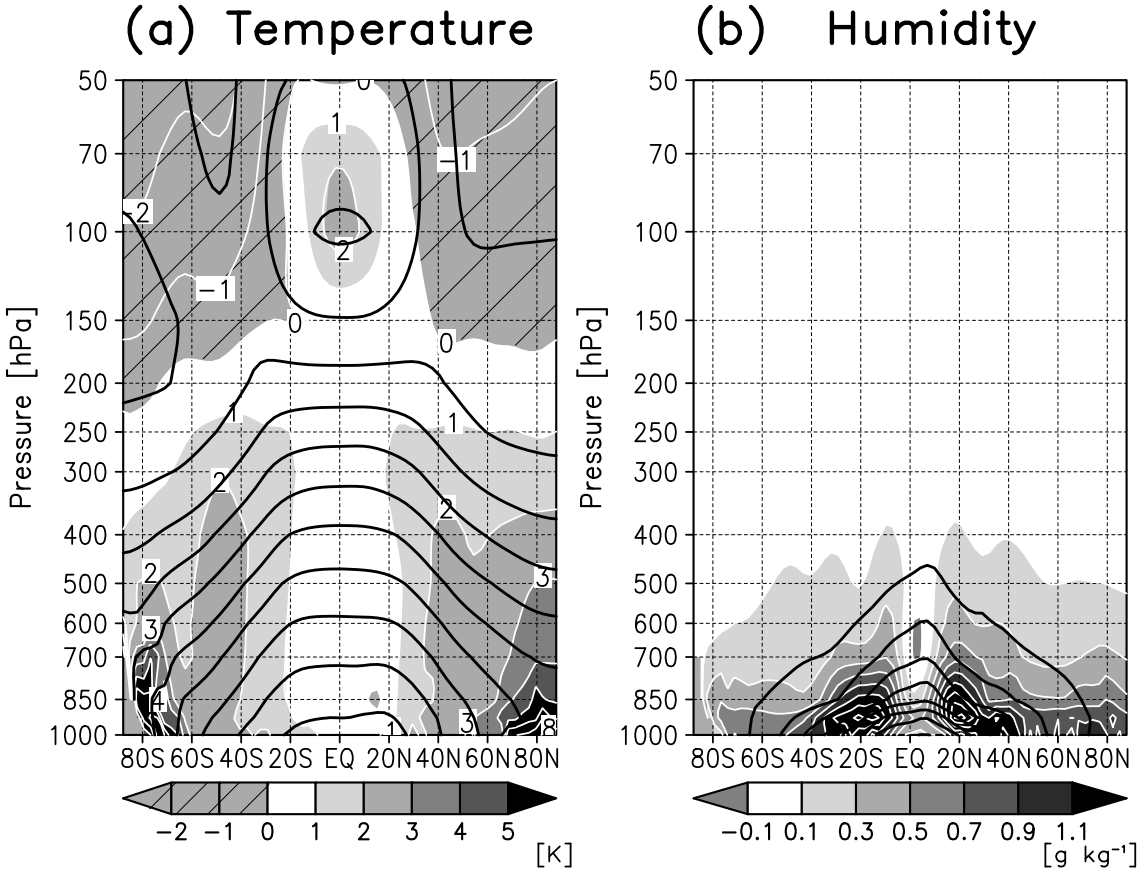

Fig. 3.11. Zonal average of annual mean (a) air temperature (K), (b) specific humidity (g kg^{-1}). Black contour represents climatological value in 0 Ma, shading and white contour represents difference between 3 Ma and 0 Ma. Black and white contour interval is (a) 10 and 1 K, (b) 2 and 0.2 g kg^{-1}, respectively.

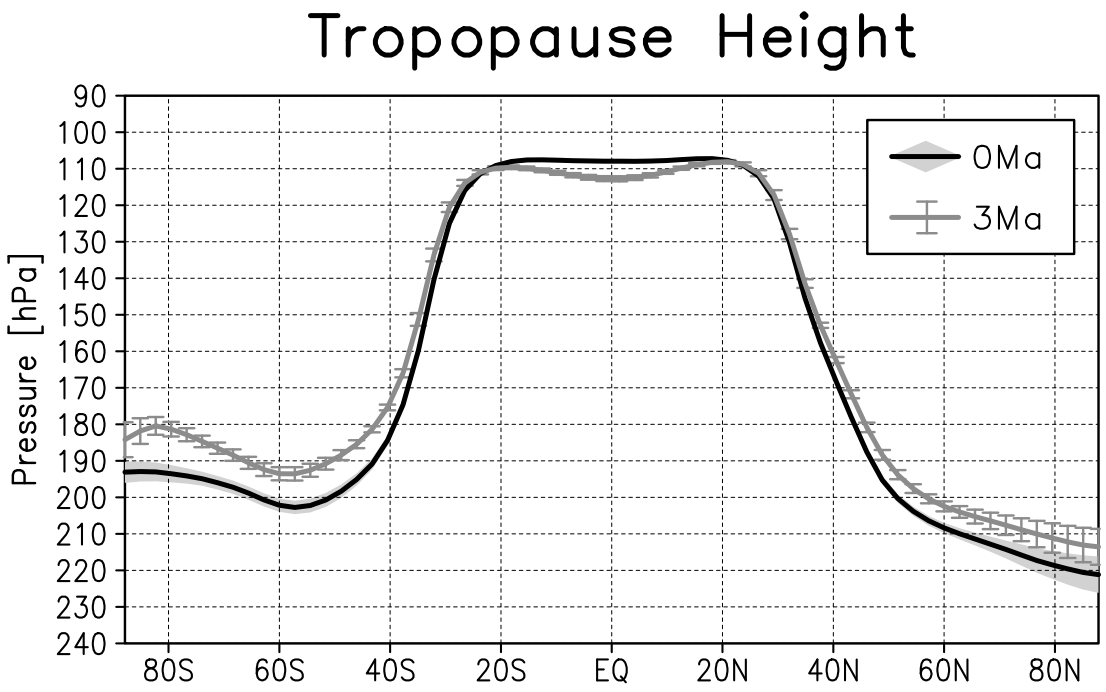

Fig. 3.12. Zonal average of annual mean tropopause height (hPa). Black and grey line represents 0 Ma and 3 Ma, respectively. Grey shading and error bars represent the ranges of standard deviations in 0 Ma and 3 Ma, respectively.

4. Radiative balance at the top of the atmosphere

4.1 Experimental design and analysis method

In this chapter, radiative balance at the top of the atmosphere (TOA) during 3 Ma is investigated. Fundamental framework of experimental design in this study is mostly identical to Chapter 3. First, we employed two experiments, 0 Ma (pre-industrial control simulation) and 3 Ma (mid-Pliocene simulation), to figure out differences of climate pattern between the two time slices. The concentrations of atmospheric CO_2 in 0 Ma and 3 Ma experiments are set to 280 and 405 ppmv. In the absence of any adequate proxy data, all other trace gases are specified to pre-industrial value, as is the solar constant. Second, 6 types of sensitivity experiments are conducted to quantify the contributions of the individual boundary conditions (CO_2, SST, sea ice, topography, land ice, and vegetation) for the 3 Ma simulation. The effect of each boundary parameter is evaluated by the difference between the 3 Ma control experiment and 3 Ma simulation forced by prescribed 0 Ma parameters (Ueda et al. 2011; Kamae et al. 2011). In addition to the sensitivity experiments in Chapter 3, an additional experiment to separate the effect of CO_2 increase (280 to 405 ppmv) is also performed in this study. To note that the surface warming due to the high-level CO_2 also affect the SST, sea ice, land ice, and vegetation in 3 Ma used in this methodology. Third, the model is also forced with 3 types of idealized patterns in anomalous SST to separate effects of zonal-mean SST anomaly (hereafter, ZSST) and zonally-asymmetric component of SST anomaly (hereafter, ZASST) in the ocean sectors (Fig. 3.1 and Table 3.3). We determine the effect of global ZSST by subtracting the result of the “3 Ma_ZSST” (forced with SST superimposed znoally-averaged anomalous SST in the globe) from the result of the “3 Ma_0SST” (forced with SST in 0 Ma). By use of ZSST replaced to 3 Ma SST in the Atlantic Ocean and Arctic Ocean (Indian Ocean and Pacific Ocean), we performed “3 Ma_AtlZSST” (“3 Ma_PIZSST”) experiment to evaluate effect of ZASST in the Atlantic Ocean and Arctic Ocean (Indian Ocean and Pacific Ocean) by comparing with the result of 3 Ma_ZSST.

The results of the idealized-SST experiments are described in Section 4.3. The model is integrated for the all experiments for 60 years. Climatological means are calculated from the last 50 years.

To separate the component of cloud effect in all-sky net (downward minus upward, shortwave plus longwave) radiative flux at TOA (hereafter, NET), we use the Cloud Radiative Forcing (CRF; Ramanathan et al. 1989; Cess et al. 1990). CRF is determined by the difference between NET and the clear-sky TOA flux (hereafter, CS), the TOA flux the atmospheric column would have if clouds were removed but all other variables remained the same. The sign convention is such that a positive forcing corresponds to a warming effect (positive downward). NET is divided to four components as follows:

$$NET = CS_S + CS_L + CRF_S + CRF_L \tag{4.1}$$

CS_S and CS_L (CRF_S and CRF_L) are the shortwave and longwave component of CS (CRF), respectively. CS and CRF are the conventional quantities describing variations of cloud-radiative balance and could be compared easily with other climate models under the intermodel-comparison framework.

4.2 TOA radiative balance and cloud amount in the mid-Pliocene

Figure 4.1 shows spatial distribution of change in net (downward minus upward, shortwave plus longwave) radiative balance at TOA (NET) in 3 Ma relative to 0 Ma. Global average of NET is increased for 3.8 W m^{-2} which is larger than the direct radiative forcing by increasing CO_2 concentration (from 280 to 405 ppmv). The spatial pattern of change in NET shows apparent regionality including land (cooling) / sea (warming) contrast in 3 Ma. Net is generally increasing over the ocean, particularly over the North Indian Ocean, tropical and subtropical Pacific Ocean, and the North Atlantic Ocean, and decreasing over mid-latitude land

regions in Northern Hemisphere (Central and East Siberia and northern North America). Net is also enhanced over subtropical land regions (subtropical North Africa, Central Asia, and Australia). In high latitude, the radiative balance at the TOA warms up the Earth system over the Arctic Ocean, Antarctic Ocean, and West Greenland and cools down over their neighboring regions, implying alterations of cloud covers in those regions. Spatial map of each component of the radiative balance determined in Section 4.1 is shown in Figure 4.2. CS_S generally explains the changes of NET (Fig. 4.1) over the land regions (Central and East Siberia, northern North America, subtropical North Africa, Central Asia, Australia, and Greenland). Major factor for the differences of CS_S are the alterations of land/sea surface cover (surface reflectance) in the subtropics and mid- and high-latitude regions (vegetation, land ice, sea ice, and associated snow cover). Increasing of CS_S over the Arctic and Antarctic Oceans are caused by the reduction of sea-ice in these regions because of greatly warmer condition in 3 Ma (Haywood et al. 2010). CS_L (Fig. 4.2b) shows similar patterns but opposite sign with little magnitude to the CS_S in high latitude. As for the subtropical regions, CS_L shows similar sign (increasing) to the CS_S. These changes are corresponding to the surface warming (mid- and high-latitude) / cooling (subtropics) during 3 Ma compared to 0 Ma (Kamae et al. 2011). CRF_S shows positive change over the low- and mid-latitude ocean and negative over the subtropical land regions and the high-latitude ocean (Fig. 4.2c). Except the low- and mid-latitude ocean, CRF_S generally reduces CS_S changes (Fig. 4.2a). CRF_S (and also NET) increases over the North Indian Ocean, western North Pacific, South Pacific Convergence Zone (SPCZ), eastern edges of the Pacific and Atlantic Oceans (off the western coasts of South and North America, and South Africa), and northern North Atlantic (Figs. 4.1 and 4.2c). Over the Arctic and Antarctic Oceans, CRF_S are decreased significantly, compensating partly the positive change of CS_S. CRF_L (Fig. 4.2d) shows opposite sign (negative) and little magnitude compared to CRF_S over the oceans in low and high latitude (Fig. 4.2c). Generally, changes in NET over the low-latitude oceans depend on the changes in the shortwave component and longwave component reduces the magnitude partly.

Figure 4.3 shows latitudinal distributions of the changes in zonal-mean NET, CS and CRF components in 3 Ma relative to 0 Ma. The global average of NET (3.8 W m^{-2}) is mainly attributed to the lower latitude region (40°S~40N°) prior to the higher latitudes because of the larger area. Shortwave components of CS and CRF in the higher latitude (particularly over the Arctic and Antarctic Ocean) are larger than those in low latitude, but they are compensating each other, resulting little changes in NET (Fig. 4.3). In low latitude, CRF_S, CS_S, and CS_L mainly contribute for the positive anomaly in NET. The increase of CRF_S (~18 W m^{-2}) between 5°S and 15°N is implying existence of changes in cloud amount over the tropics. Figure 4.4 shows latitudinal distribution of differences in cloud cover between 3 Ma and 0 Ma. Cloud covers are diminished significantly (~2%) at middle to upper level in tropics and lower and middle level in subtropics and extratropics. In contrast, high level cloud in mid- and high-latitudes and all levels cloud throughout troposphere in high-latitude are increasing. Much reduced high level cloud (Fig. 4.4a and 4.4b) in tropics enhances radiative cooling of the atmosphere (~10 W m^{-2}, shown in Fig. 4.3), but the reduction of total cloud amount reduces the optical thickness of cloud and intensifies the incoming solar radiation (~18 W m^{-2}) and then Net in tropics is much enhanced (12 W m^{-2}, also contributed by CS_S and CS_L) in 3 Ma compared to 0 Ma (Fig. 4.3). Over the Arctic and Antarctic Oceans (65°N-90°N and 75°S-55°S), increase in cloud cover (Figs. 4.4a and 4.4b) tends to cool the Earth, but increased CS_S by reduction in surface albedo compensates the CRF effect (Fig. 4.3).

The differences of the atmospheric compositions (CO_2) and surface boundary conditions (SST, sea ice, topography, land ice cover and volume, and vegetation) in 3 Ma could alter surface albedo and/or atmospheric radiative balances by changes in atmospheric conditions. Figure 4.5 shows effects of the individual boundary conditions for the changes in NET in 3 Ma. The increase in atmospheric CO_2 concentration (280 ppmv in 0 Ma, 405 ppmv in 3 Ma) does not affect regional radiative balance but modifies the global-averaged radiative balance (described in Section 4.4). The increases of NET over the oceans, i.e., the North Indian Ocean, western North

Pacific, SPCZ, and North Atlantic (Fig. 4.1), are mainly induced by the alteration of SST (Fig. 4.5b). The reduction of sea ice also intensifies Net over the Arctic and Antarctic Ocean (Fig. 4.5c). The alteration of topography modifies atmospheric circulations and snow covers but its contribution on the radiative balance is relatively small (Fig. 4.5d). The reductions of the land glaciers over the East Antarctic and Greenland reduce surface albedo in those regions and also modify formation of cloud around those regions (Fig. 4.5e). Over the land regions in low- and mid-latitude, NET is generally affected by the shift of boundaries in vegetation cover (Fig. 4.5f). The decreasing of surface albedo by grassing and foresting over the subtropical North Africa, Central Asia, and Australia enhance the NET in those regions (Fig. 4.1). Expansions of the grassland over Eurasian and North American continent in mid-latitude (Salzmann et al. 2008) reduce the shortwave radiation at the surface. The boundaries of boreal forest and tundra shifts poleward, inducing positive change in Net in the higher latitudes. Figure 4.6 shows zonal-mean change in net radiations and its components due to the effects of the individual boundary conditions. Increases of CS_L and NET by rising of atmospheric CO_2 level are almost uniformly (Fig. 4.6a). The alteration of SST pattern in 3 Ma induces positive change due to the increase of CRF_S in low latitude, and negative change induced by CS_L in mid- and high-latitude (Fig. 4.6b). The effects of the individual boundary conditions on the globally-averaged radiative balance are discussed in Section 4.4. The sea ice reductions in the higher latitude (75°S~55°S and 65°N~90°N) induce positive change in CS_S and CRF_L and negative change in CS_L and CRF_S induced by the sea ice reduction are compensating each other and producing modest change in NET (Fig. 4.6c). The NET in those latitudes is increased (~10 W m^{-2}) because the former tends to be larger than the latter. The alterations of topography and land ice induce small changes in net radiation (Figs. 4.6d and 4.6e). The shifts of boundaries of surface vegetation covers enhance CS_S together with the weakening of CRF_S.

4.3 Dependences of cloud amounts and radiative balances on SST patterns

The increase of Net in low latitude (Fig. 4.3) mainly induced by the alteration of SST pattern in 3 Ma (Fig. 4.6b). The spatial pattern of 3 Ma SST has the two major characteristics; 1) decreasing of meridional gradient due to prominent warming in mid- and high-latitude despite little changes in low latitude, and 2) reduction of east-west gradient in low latitude by the warming in the upwelling regions in the eastern edges of the oceans. To decompose contributions of the former corresponding with the broadening of ascending branch in Hadley circulation and the latter inducing the weakening of Walker circulation (see Chapter 3), we conduct the idealized SST experiments described in Section 4.1.

Figure 4.7 represents the effect of each anomalous SST pattern (ZSST and ZASST in each ocean sector) on the TOA radiation. Figs. 4.7a, 4.7b, 4.7c, and 4.7d represent the effects of global SST, global ZSST, SST in Pacific and Indian Ocean and ZSST in Atlantic Ocean, and SST in Atlantic Ocean and ZSST in Pacific and Indian Ocean. The effect of global ZSST (Fig. 4.7b) and ZASST in Atlantic Ocean (Fig. 4.7d compared to Fig. 4.7b), show some differences with that of global SST (Fig. 4.7a) in low latitude. Those effects reproduce the positive Net in low latitude with much restricted strength (~3 W m^{-2}) relative to that of global SST (~10 W m^{-2}). In contrast, increase of Net in low latitude is well reproduced by the effect of ZASST in the Indian and Pacific Ocean (~10 W m^{-2}, Fig. 4.7c compared to Fig. 4.7b) due to significant increase in CRF_S (~21 W m^{-2}). Over the oceans in low and mid latitude, spatial distribution of CRF_S with the effect of ZASST in the Indian and Pacific Ocean is similar to the change in Net due to the alteration of global SST (figure not shown). For the mid- and high-latitude, the enhanced radiative cooling due to the temperature rise is well reproduced by the global ZSST and Atlantic ZASST experiments (Figs. 7b and 7d), resulting negative change in globally-averaged Net in these experiments (see Section 4.4).

Figures 4.8 and 4.9 show changes in spatial distribution of cloud covers due to the effects of ZSST and ZASST in the individual oceans. Geographical pattern of changes in cloud amount

due to the alteration of global SST (Fig. 4.8a) resembles that of CRF_S (Fig. 4.2c) and NET (Fig. 4.1). Cloud amount is increased only over the subtropical land regions due to the wetter condition (see Chapter 3). Over the North Indian Ocean, western North Pacific, tropical and subtropical central Pacific, SPCZ, eastern edges of the Pacific and Atlantic Oceans, and northern North Atlantic, the cloud covers are reduced, inducing the positive radiative forcing at the TOA (Fig. 4.2c and 4.5b). With the effect of global ZSST, the weakening and the expansion of ascending branch of Hadley circulation (see Chapter 3) induces reduction of cloud cover at mid to high level of troposphere in low latitude but it is not sufficient relative to that of global SST (Figs. 4.8b, 4.8c, 4.9b, and 4.9c). The reductions of east-west SST gradient in Indian Ocean and Pacific Ocean in low latitude lead to the weakening of east-west atmospheric overturning circulation and deep convective activity in tropics (see Chapter 3). In addition, SST increase in eastern edges of the Pacific and Atlantic oceans reduces amount of stratocumulus clouds over the regions (Fig. 4.8c). These results indicate that the zonally-asymmetric patterns in the Indian and Pacific Ocean SST in 3 Ma have essential roles for the increase of CRF_S and NET in low latitude.

4.4 Global radiative forcings in the mid-Pliocene

The global-averaged radiative forcings in 3 Ma due to the individual boundary conditions are summarized in Figure 4.10. The major factor for the global average of anomalous NET in 3 Ma (+3.8 W m^{-2}) is atmospheric CO_2 concentration (1.4 W m^{-2}) which alters CS_L uniformly (Fig. 4.6a). This is followed by the change in SST pattern (1.3 W m^{-2}). Despite the prominent warming in mid- and high-latitude forced by the SST alteration reduces CS_L and cools the system (Fig. 4.6b), the positive radiation due to CS_S (Fig. 4.6b) in low latitude warms the system in the global-averaged radiative balance (Fig. 4.10). The sea ice, topography, and land ice also affect global radiative balance but the amplitude is moderate (0.5, 0.3, 0.0 W m^{-2}, respectively) compared to the CO_2 and SST because their areas are restricted (Figs. 4.5 and 4.6). The effects of

vegetation are appeared in relatively wider regions but contribute little (0.0 W m^{-2}) to the global radiative balance (Fig. 4.10) because the positive and negative changes compensate each other (Fig. 4.6f). The contributions of SST alteration in the ocean sectors determined by the idealized experiments highly depend on where the zonal asymmetric pattern is applied. Global ZSST and ZASST in Atlantic Ocean do not induce positive forcing in the globally-averaged radiative balance (-0.8 and -0.6 W m^{-2}, respectively). In contrast, warming effect similar to the SST effect (1.3 W m-2) is reproduced by ZASST in the Indian and Pacific Ocean (1.3 W m^{-2}), indicating the dependence of the 3 Ma radiative balance on the ZASST in the Indian and Pacific Ocean. To note that the sum of the effects of three types of SST pattern does not correspond with the total SST effect because of the any SST patterns contain the change in the meridional SST gradient (Sections 3.1.2 and 4.1). The enhanced radiative cooling (increase in CS_L) due to the SST warming in mid- and high-latitiude tends to be prior to the CRF (Fig. 4.7), resulting the negative forcing in globally-averaged radiative budget (Fig. 4.10). The reduction of cloud formation at higher troposphere according to the weakening of deep convection over the North Indian Ocean, western North Pacific, tropical and subtropical central Pacific, SPCZ, and equatorial eastern Pacific and reduction of stratocumulus cloud over the eastern edges of the Pacific Ocean induced by the ZASST in the Indian and Pacific Ocean (Fig. 4.8c) are more dominant relative to the cooling effect by the mid- and high-latitude warming (Fig. 4.7c), resulting the positive forcing for the Earth system (Fig. 10).

4.5 Summary and discussions

The Earth climate system during the 3 Ma warm period is cooled by the enhancement of longwave emission owing to the warmer condition in mid- and high-latitude. However, the global radiative balance at TOA warms up the system (+3.8 W m^{-2}) particularly in low latitude. In addition to the CO_2 radiative forcing, the alteration of SST pattern in low latitude, associated with the changes in ocean heat transport and thermal structure, induces the reductions of the

cloud cover, resulting warms up the Earth system. The magnitude of the SST effect is prior to the other factors of surface forcings, the sea ice reduction, changes in the topography, the shrinking of the land glaciers, and the shifts of vegetation cover. The positive change in CRF_S associated with the general reduction of cloud amount in low latitude are partly damped by the cooling effect of CRF_L. The weakening of shortwave reflection by cloud according to the reduction of cloud cover (deep convective cloud in the North Indian Ocean, western North Pacific, and SPCZ, and low-level stratocumulus in the eastern edges of the ocean sectors) is primarily induced by the diminished east-west gradient of SST in low latitude documented by the several types of proxy evidences. This study also shows that the change in the meridional SST gradient does little to enhance the radiative forcing in low latitude, resulting negative forcing in global radiative balance.

The relative importance in the reductions of meridional and zonal SST gradient in low latitude was also investigated by idealized experiment in Brierley and Fedorov (2010). They concluded that the magnitudes of those effects on global radiative balances are comparable, contrasting to the results of this study. In the previous study, simplified-SST pattern assuming no zonal SST gradient across the basin by extending 16 sites of SST estimates in tropics and subtropics is prescribed to isolate the two effects on various kinds of regional climate changes (i.e. ice sheet inception over North America, and African and Asian monsoon intensity). This study, in contrast, is based on the global paleoenvironmental reconstruction which includes the east-west SST gradient (SST in the western Pacific is higher than the eastern Pacific for ~2 K) based on the 86 sites of proxy evidences (Dowsett et al. 2009b). However, the SST reconstruction in PRISM3 also contains uncertainty in estimation by single or multiple proxy evidences and limited density of data coverage. These results indicate that the accuracy in changes of spatial pattern and magnitude in tropical and subtropical SST has predominant impact for the insight of the warmth in the Pliocene Earth system.

As related to the above, the other reconstructions used as the boundary conditions in this

study also contain some uncertainties. In addition to the direct evidences, extrapolation by using of the other paleoenviromnental data were applied to estimate the extent and coverage of sea ice and land glaciers in Arctic, Greenland, and Antarctic regions where the direct geological evidences are sparse (Haywood et al. 2010). The vegetational reconstruction is based on palaeobotanical data set and biome prediction using climate parameters based on a GCM simulation (Salzmann et al. 2008). The simulated biome pattern, particularly the poleward shift of the boreal forest and tundra, the expansion of the grassland in the mid-latitude land regions in Northern Hemisphere, and the shift of tropical savanna and grassland, are depend on the GCM used for simulating the climate parameters (Haywood et al. 2009b, Kamae and Ueda 2011). The surface albedo and cloud covers over the land regions in 3 Ma have substantial uncertainties in the data sparse regions. The reconstruction of surface environment in 3 Ma is now improving by using newly archived data (e.g., Reed-Sterrett et al. 2010; Salzmann et al. 2011). The next phase of the reconstruction project, PRISM4, now progresses efforts for integrating multi-proxy data including new proxy evidences for providing more accuracy and consistency in boundary conditions used for the numerical climate simulations (Dowsett et al. 2010). In addition, the multi-model simulations and comparisons under the PlioMIP framework (Haywood et al. 2010, 2011) applying the same experimental settings will facilitate evaluations of the model-uncertainly in simulation for the 3 Ma warmth (e.g., Chan et al. 2011; Yan et al. 2011; Koenig et al. 2012; Kamae and Ueda. 2012b).

The global radiative forcing warming up the 3 Ma Earth system shown in this study is mainly contributed by the positive radiative balance in low latitude. In contrast, the surface environment in mid- and high-latitude is much warmer relative to that in low latitude. The inconsistency requires of the enhancement of meridional heat transport in the 3 Ma climate system (e.g., Crowley 1996; Haywood et al. 2009a). The recent studies revealed the role of stronger Atlantic meridional overturning circulation (e.g., Robinson et al. 2011), and upper-ocean circulation (Philander and Fedorov 2003; Fedorov et al. 2010) for the sustainment of SST pattern

and ocean thermal structure in 3 Ma. Further studies about the meridional and general circulations (atmosphere and ocean) by proxy data and modeling approaches have necessities for the insight of sustainment of the warmer Earth climate system including future climate change in longer timescale.

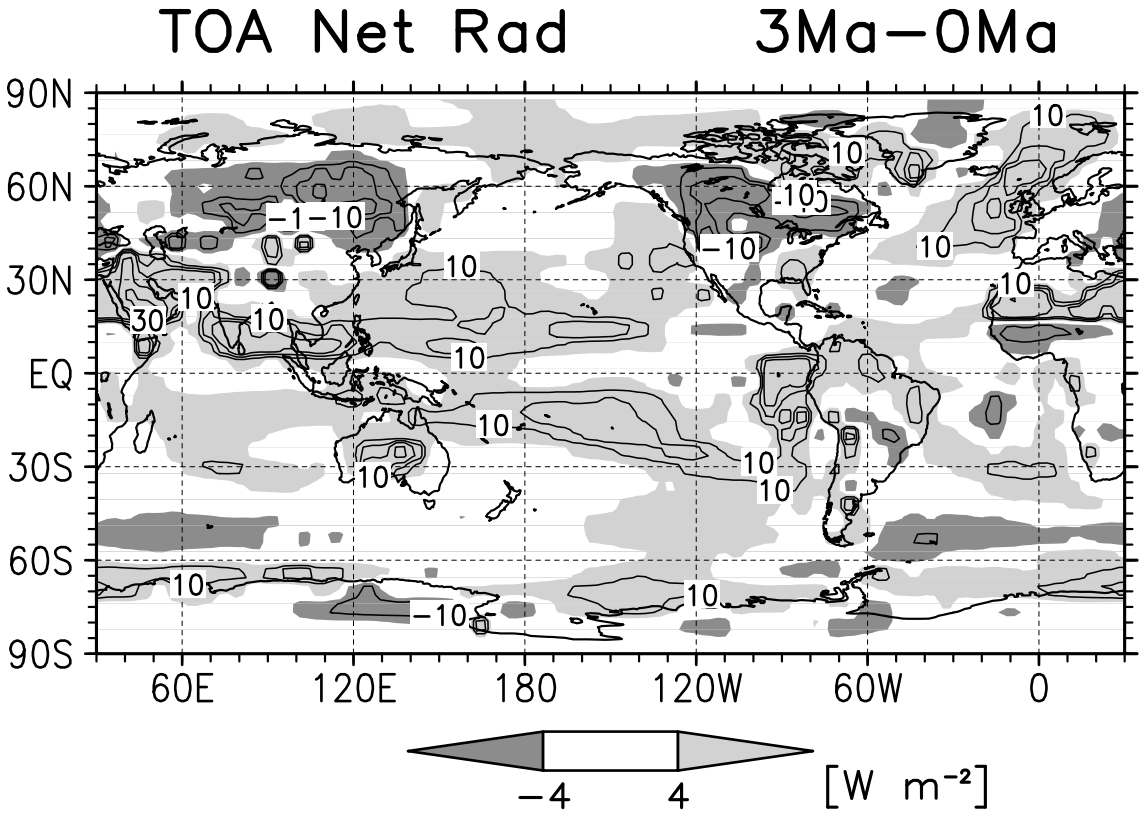

Fig. 4.1. Differences in annual mean net (shortwave plus longwave) radiation (W m^{-2}) at the top of the atmosphere (TOA) between 3 Ma and 0 Ma. Contours represent ±10, 15, 20, 30, and 40 W m^{-2}.

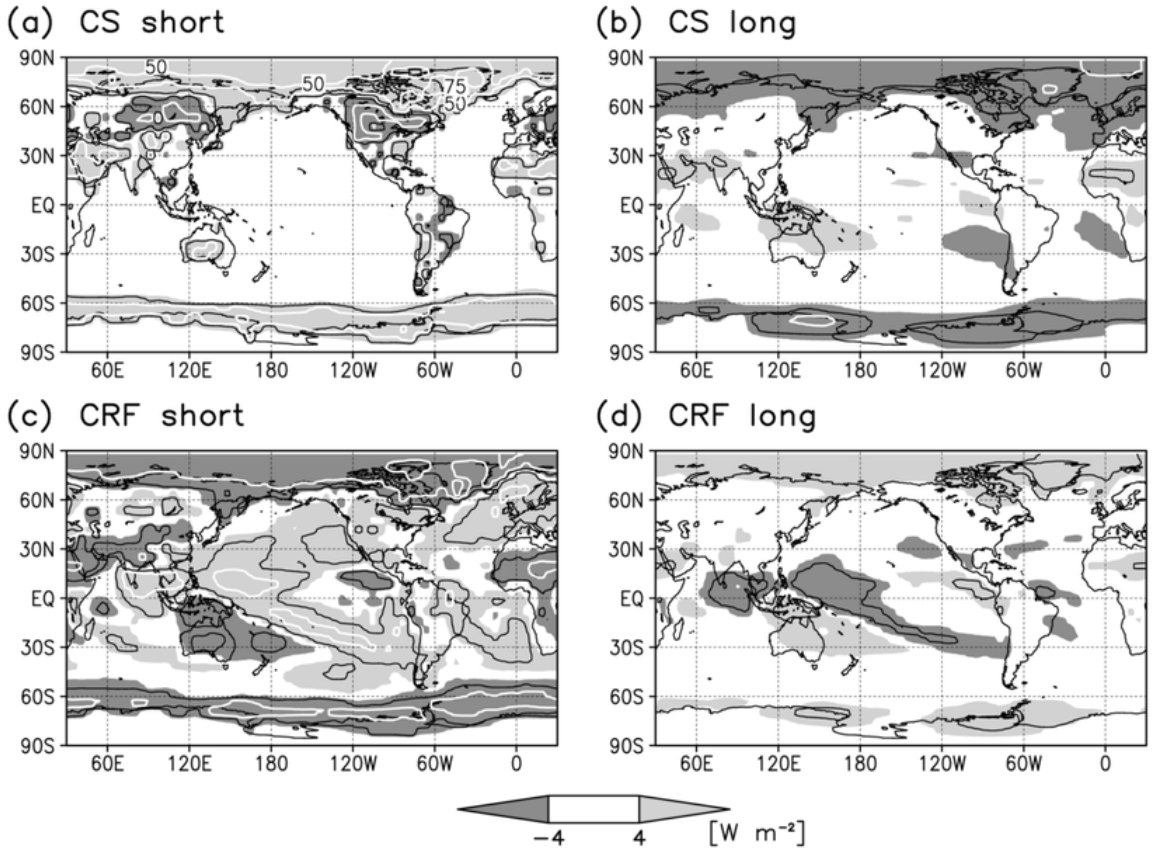

Fig. 4.2. Same as Fig. 4.1, but for its components. (a) Clear-sky (CS) shortwave radiation, (b) CS longwave radiation, (c) shortwave and (d) longwave component of cloud radiative forcing (CRF). Black contours represent ±10 W m^{-2}. White contour interval is 25 W m^{-2}.

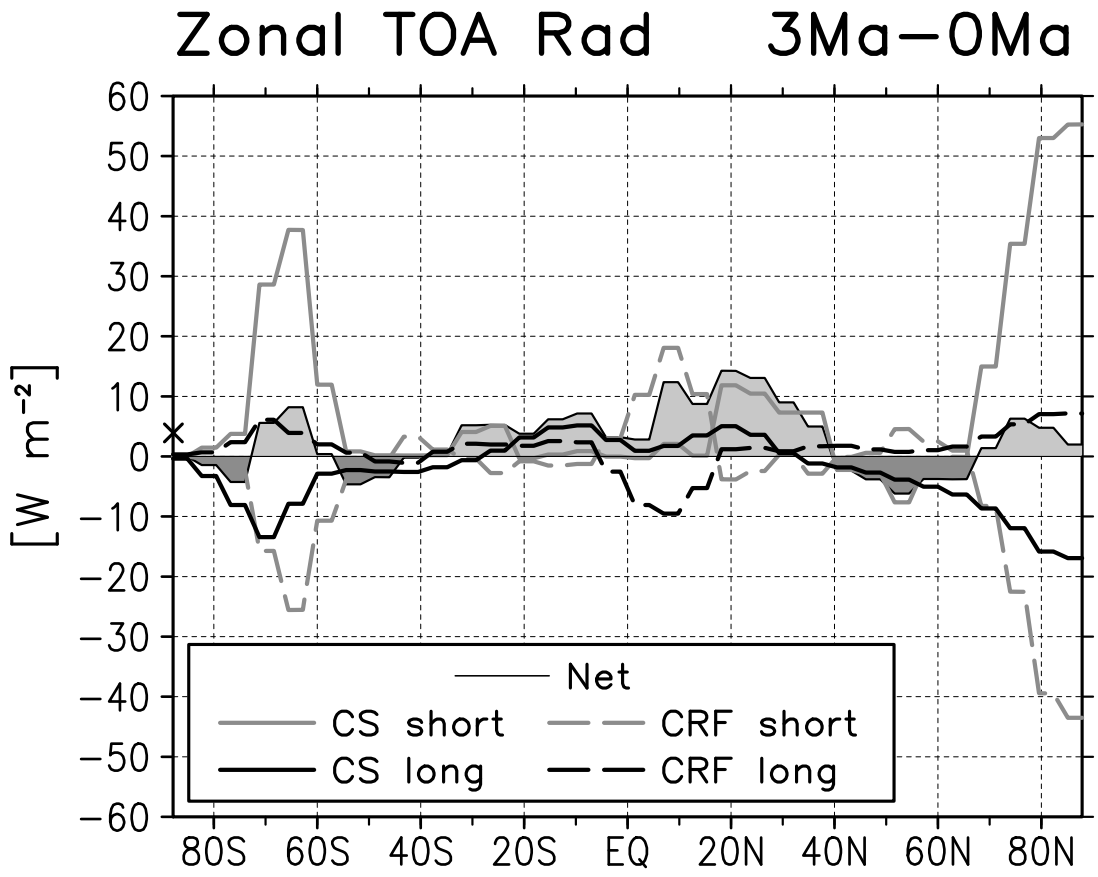

Fig. 4.3. Differences in zonal average of annual mean TOA radiation between 3 Ma and 0 Ma. Thin line represents net radiation. Grey and black solid lines indicate CS shortwave and longwave radiations, respectively. Grey (black) dashed line is shortwave (longwave) component of CRF.

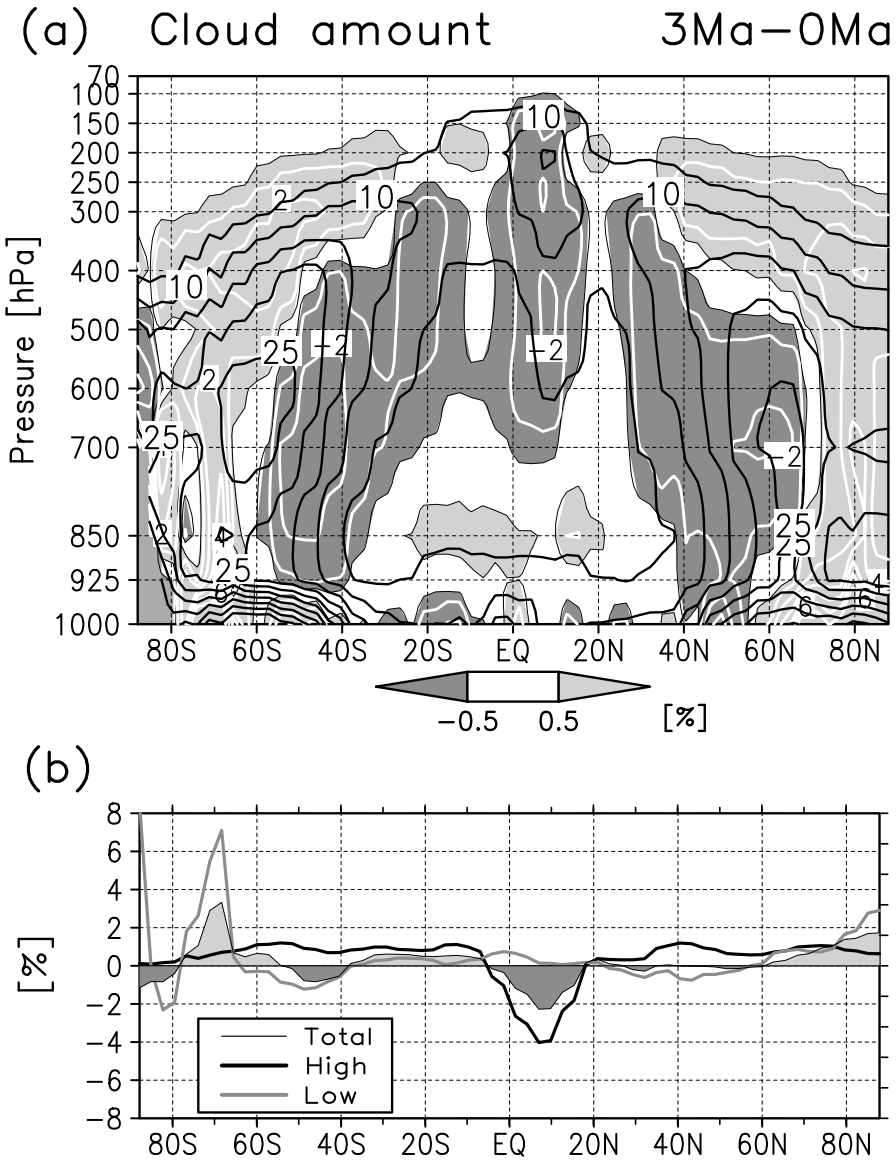

Fig. 4.4. (a) Latitude-height cross section of difference in zonal average of annual mean cloud amount between 3 Ma and 0 Ma. White contour interval is 1%. Solid black contour represents climatological value in 0 Ma (interval is 5%). (b) Latitudinal distributions of cloud amounts in total, high, and low level. High clouds are defined as clouds above the 400 hPa level, while low clouds occur below 700 hPa.

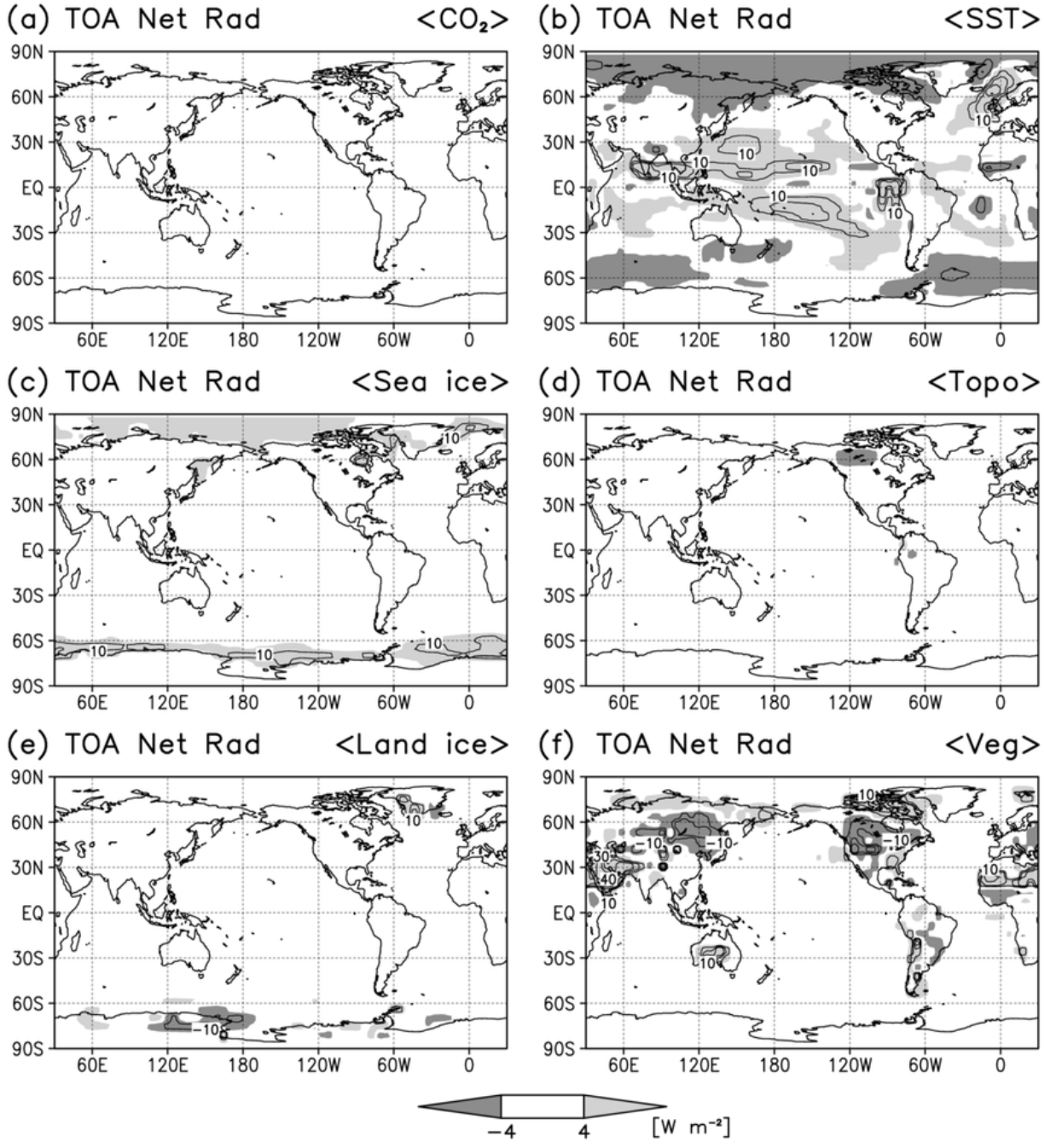

Fig. 4.5. Changes in the TOA net radiation (W m^{-2}). (a) Effect of increase in atmospheric CO_2 concentration (280 to 405 ppmv), (b) SST, (c) sea ice, (d) topography, (e) land ice, (f) vegetation. Contours represent ±10, 15, 20, 30, and 40 W m^{-2}.

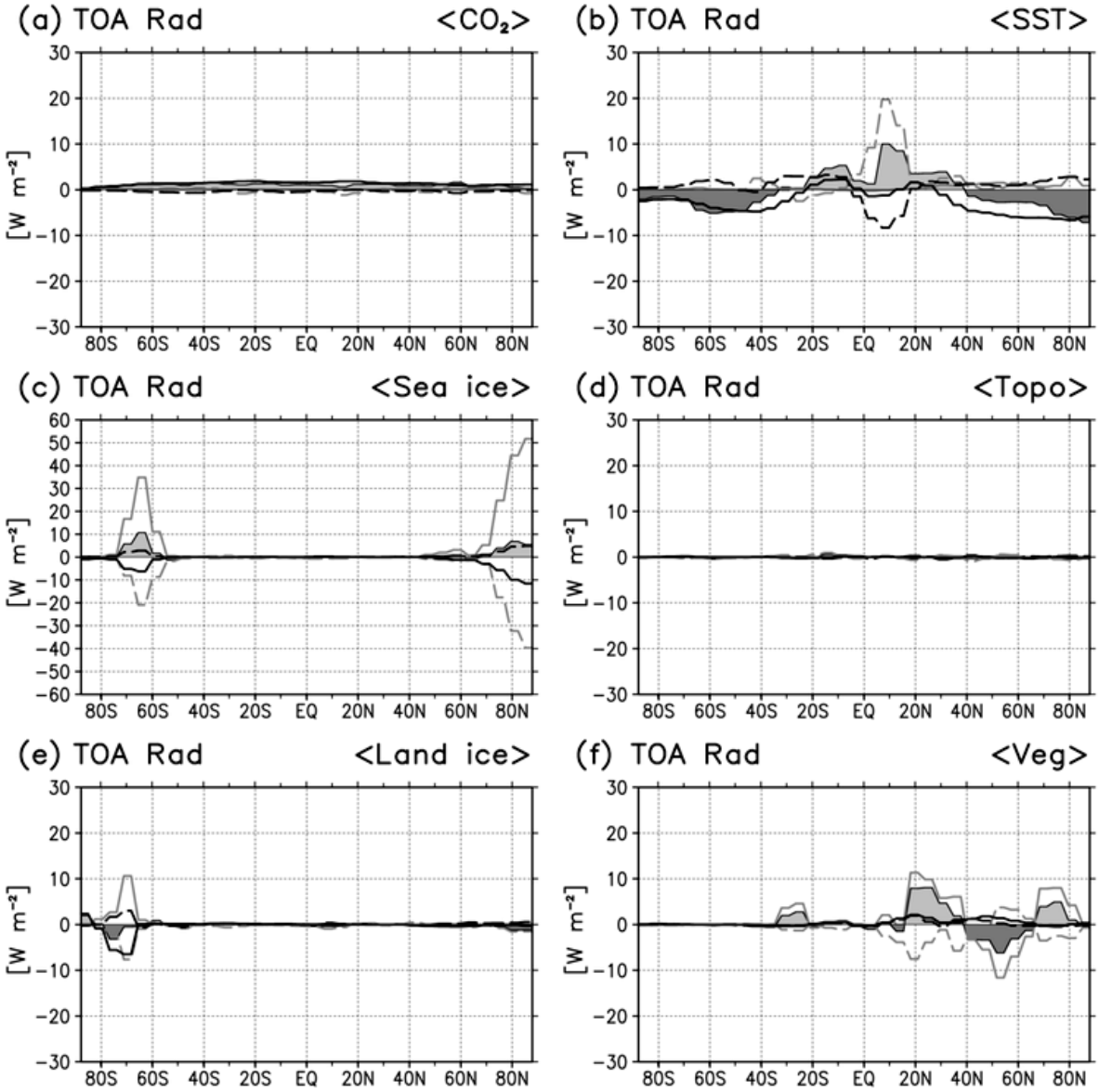

Fig. 4.6. Same as Fig. 4.3, but for the effect of (a) increase in atmospheric CO_2 concentration, (b) SST, (c) sea ice, (d) topography, (e) land ice, (f) vegetation. Scale of vertical axis range in (c) is twice larger than others.

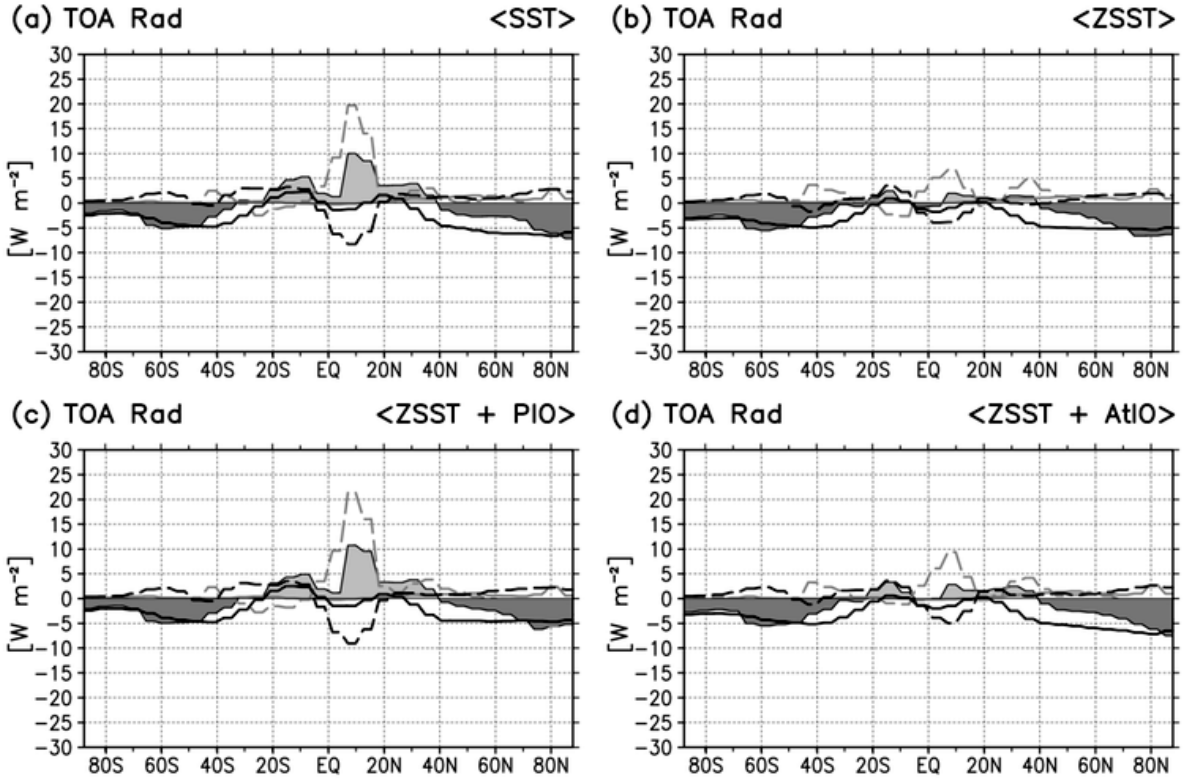

Fig. 4.7. Same as Fig. 4.6, but for the effect of (a) 3 Ma SST in the globe. (b) 3 Ma zonal-mean SST (ZSST) in the globe, (c) 3 Ma SST in the Pacific/Indian Ocean and ZSST in the Atlantic Ocean, and (d) 3 Ma SST in the Atlantic Ocean and ZSST in the Pacific/Indian Ocean.

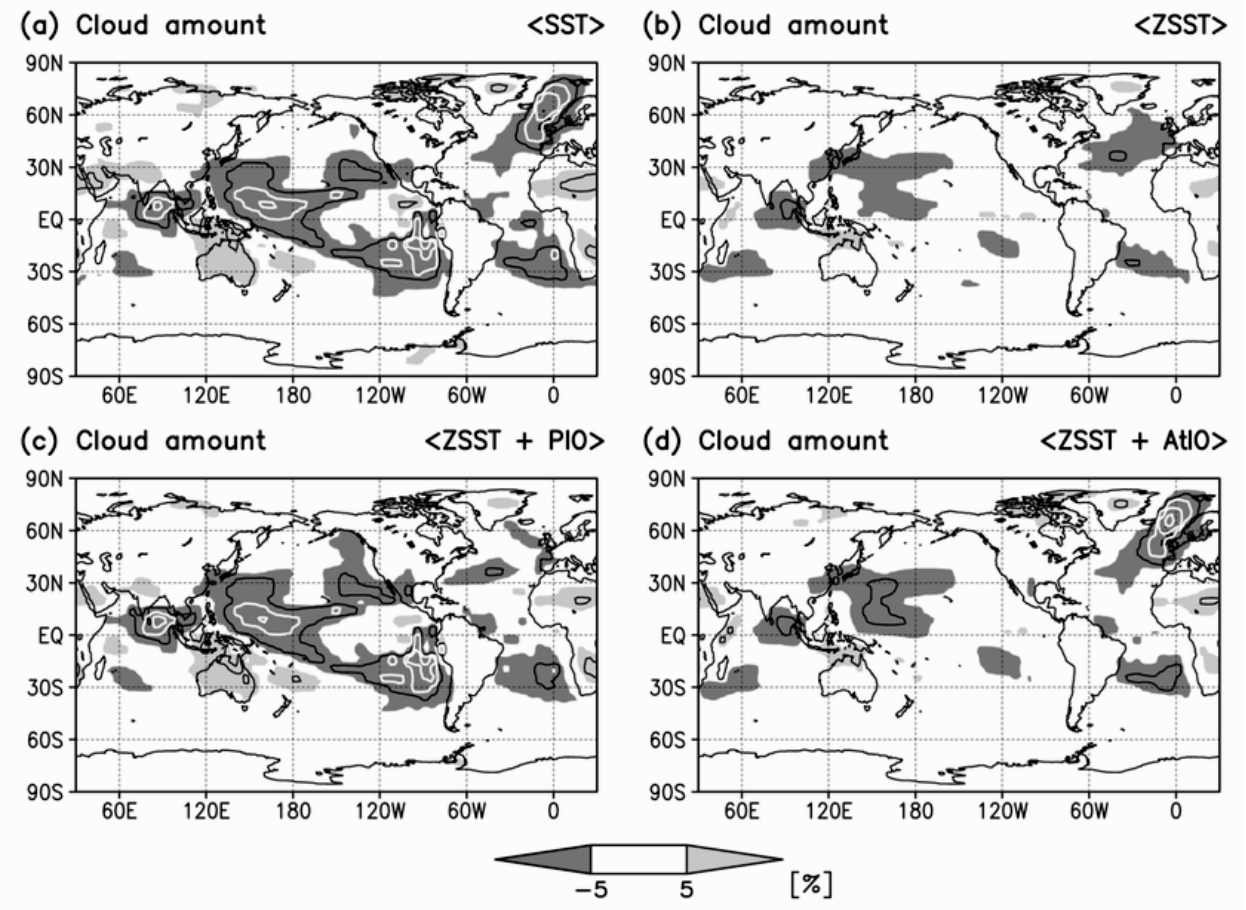

Fig. 4.8. Same as Fig. 4.7, but for spatial distribution of changes in total cloud amount (%). Black contour represents ±10%. White contour shows ±15, 20, 25, 30%.

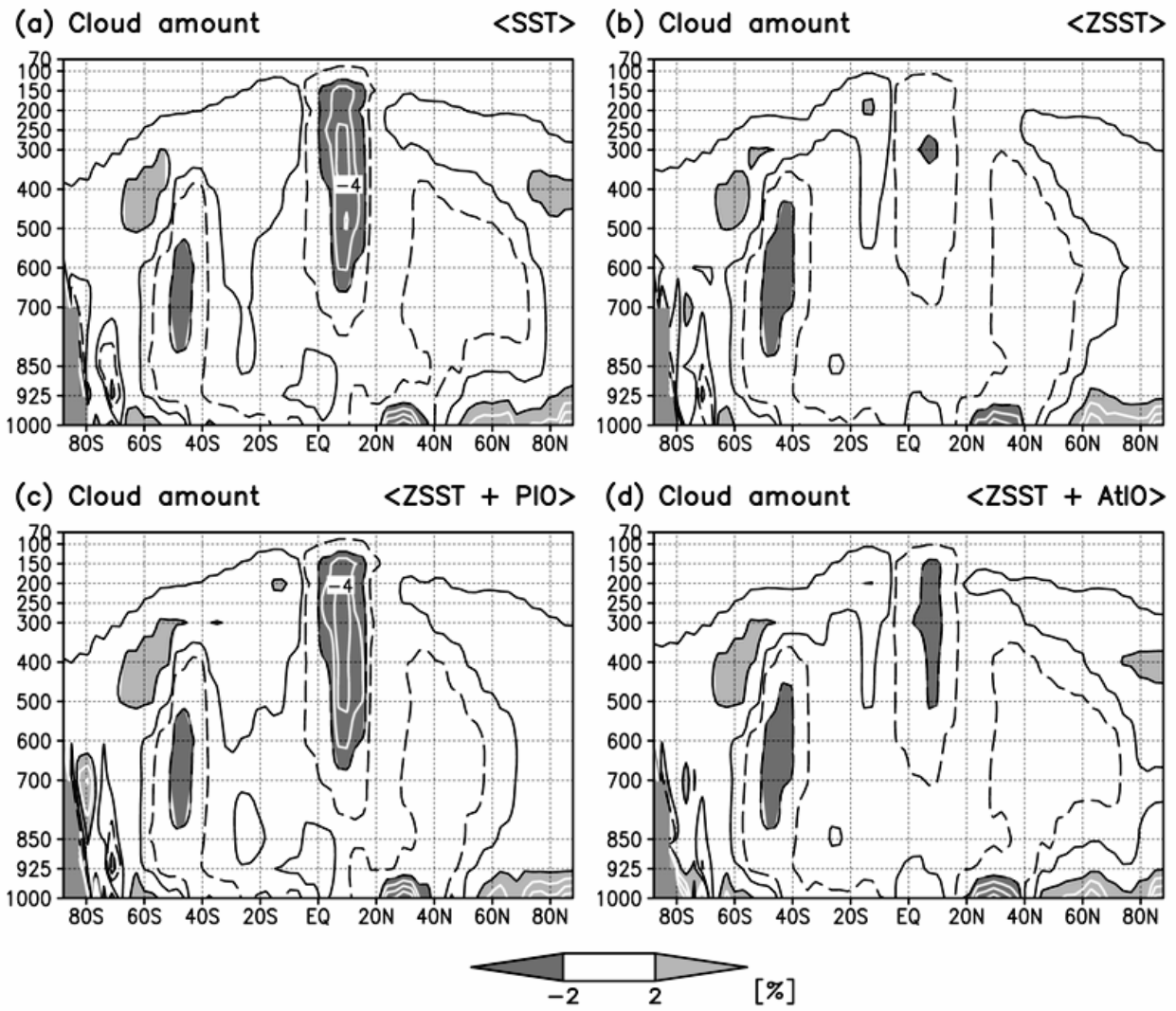

Fig. 4.9. Same as Fig. 4.8, but for the latitude-height cross section of zonal-mean cloud amount. Black solid (dashed) contour represents +1 (−1)%. White contour shows ±3, 4, 5%.

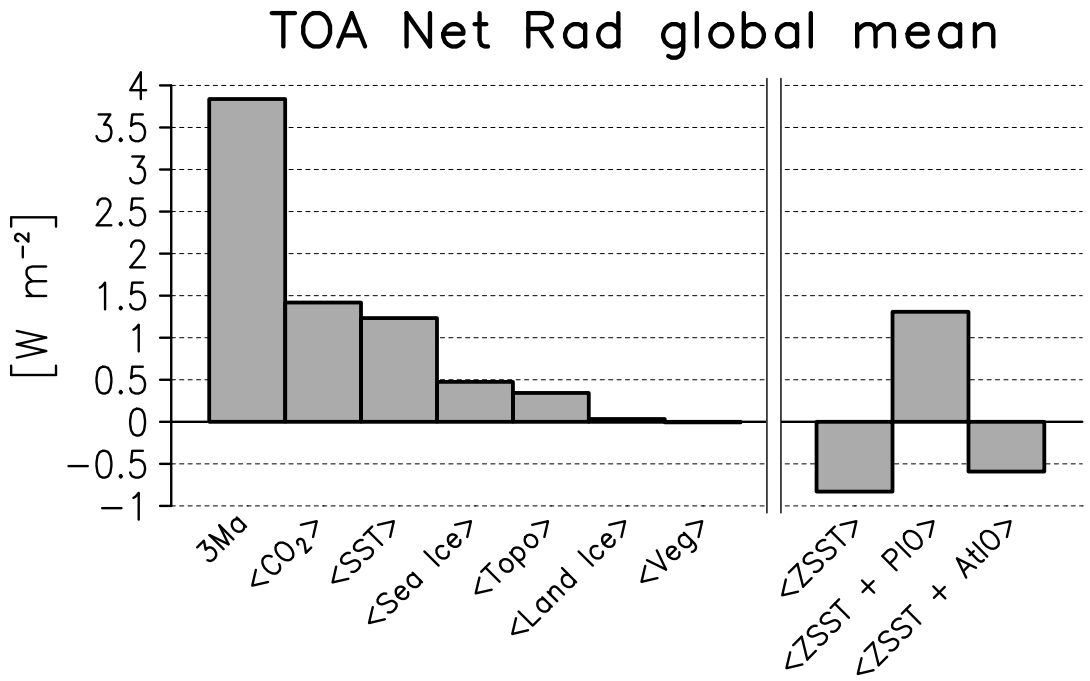

Fig. 4.10. Changes in global average of annual mean TOA net radiation (W m^{-2}).

5. Evaluation of simulated climate in lower latitude regions using paleovegetation data

5.1 Experimental design and analysis method

5.1.1 Vegetation simulation using BIOME4

The simulated climate parameters during mid-Pliocene warm period in Chapters 3 and 4 could be evaluated through comparison with the paleobotanical proxy date suggesting natural vegetation during the period by using equilibrium biogeography model. For diagnosis purposes, biome simulations could be run using GCM-derived climatologies directly (e.g., Claussen 1997) from mid-Pliocene warm period (3.6~2.6 Ma, MPWP) and present day (PD) experiments (i.e., direct procedure). However, this would necessitate an evaluation of the simulated vegetation patterns in both the MPWP and the PD experiments. The MPWP biomes simulated directly contains the uncertainties in GCM (e.g., physical parameters and schemes) and the boundary conditions (e.g., SST distribution and land ice volume/coverage). In this study, we adopted an anomaly procedure (e.g., Kaplan et al. 2003; Wohlfahrt et al. 2008; Haywood et al. 2009) for MPWP biome simulations by using the "3 Ma_0veg" experiment in Chapter 3. The use of an anomaly procedure, in which the changes in climate between two simulations are superimposed on an observation-based PD climatology, enables us to compensate the first-order biases in the climate control simulation (e.g., Harrison et al. 1998; Wohlfahrt et al. 2008) and extract general discrepancies in biome types caused by the uncertainties in the boundary conditions during MPWP. To apply this procedure, differences in the climatological values of monthly mean precipitation, temperature, and percent of potential sunshine hours between MPWP and PD climate experiments described in Chapter 3 were linearly interpolated to the 0.5° grid of the BIOME4 model and then added to a long-term mean climatology for the 20th century

(1901-1996), CLIMATE 2.2 (Kaplan et al. 2003). This modern climatology is an improved version of the Leemans and Cramer (1991) data set, based on a greatly expanded weather station network. The dataset was generated by interpolating climate parameters from station data. The interpolation method is thin-plate smoothing splines (Hutchinson and Bischof 1983; Hutchinson 1995) which is highly appropriate for interpolating climate data from a sparse or irregular network of stations (Kaplan et al. 2003). Soil properties were specified from a dataset derived from Food and Agriculture Organization (FAO) global soil map (FAO 1995). Atmospheric CO_2 concentrations of 324 and 405 ppmv are used to force BIOME4 for PD and MPWP biome simulations, respectively. The former is approximately the mean value during the period of measurement of the climate station data used in CLIMATE 2.2. The CO_2 concentration in the latter experiment is based on the several types of proxy data during the MPWP (Haywood et al. 2010) and was also used in MPWP climate simulation conducted in Chapter 3.

The anomaly climate driving BIOME4 model on anomaly procedure was derived from an atmospheric general circulation model (AGCM) experiments described in Chapter 3 by use of an atmospheric component of MRI-CGCM2.3.2 (Yukimoto et al. 2006). The AGCM has a horizontal resolution of 2.8° × 2.8° in latitude and longitude, 30 layers in the vertical. For the MPWP climate simulation, the AGCM was set with Pliocene Research, Interpretation and Synoptic Mapping phase 3 (PRISM3) boundary conditions (Dowsett et al. 2010; Haywood et al. 2010) and a CO_2 concentration of 405 ppmv. Topography in MPWP is set to higher East African Rift Valley for 500 m and lower elevation in the western cordilleras of the North America and the northern South America than PD (Thompson and Fleming 1996; Dowsett et al. 1999; Sohl et al. 2009; shown in Fig. 2.1b). Land ice over Greenland and Antarctic were restricted to much reduced extent (Dowsett et al. 1999; Haywood et al. 2010; shown in Fig. 2.2). Sea surface temperature (SST) contains prominent warming in mid- and high-latitude and equatorial and coastal upwelling regions (Dowsett et al. 2009; shown in Fig. 2.1a). Sea ice cover in Southern Hemisphere and the Arctic region shows seasonally ice-free condition and extreme warm

environment (Haywood et al. 2010; shown in Fig. 2.3). The anomaly climate is derived from the differences in the 50-year climatologies between the MPWP and PD climate experiments. Only the difference of the absolute minimum temperature is derived from the last 5 years in each experiment. To note that the anomaly climate used in this study is derived from the "3 Ma_0veg" experiment in Chapter 3 which was conducted with the present-day vegetation distribution as a boundary condition. The anomaly climate is mainly contributed by the unique zonal/meridional patterns of the MPWP SST (Dowsett et al. 2009).

5.1.2 Data-model comparison on each site

The PRISM3 vegetation reconstruction (Salzmann et al. 2008) was compiled from fossil pollen and plant macrofossil data from 202 terrestrial sites covering all continents and classified into 28 types of BIOME4 classification scheme. Figure 5.1a shows the location and biome type of paleobotanical data on each site. The dataset shows an exceptionally better spatial coverage relative to the previous version of the dataset (Thompson and Fleming 1996), allowing more detailed reconstruction of MPWP climate, especially in subpolar and subtropical regions. The use of the BIOME4 classification scheme allows a numerical comparison between climate parameters deduced from vegetation simulations with observational PD and GCM-derived anomaly (MPWP minus PD) climate data.

For the purposes of detecting relatively large changes in climate resulting in major alterations of vegetation, we adopted a simplified biome classification scheme, MEGABIOME, grouping individual biomes into major vegetation types (Harrison and Prentice 2003). We distinguish match or mismatch of MEGABIOME types between proxy and simulation by a criterion, whether the fraction of the area in which the simulated MEGABIOME is the same to the reconstructed type in the 1 grid of the GCM (~2.8°) square region is above 5% (match) or below (mismatch). The estimate of mismatches between the data and the model in this study using MEGABIOME scheme is relatively conservative.

This study only focuses on the relatively warmer regions and major pattern in differences of MEGABIOME because of some limitations (see Section 5.3). The paleobotanical data in the region between 45°S and 45°N are used in this study. The data in which the locations of the sites are higher than 2,000 m altitude are also eliminated. 118 sites of the paleovegetational proxy records used in this study are mapped in Fig. 5.1.

5.2 General patterns of biome simulations

Figures 5.1b and 5.1c show simulated vegetation patterns in the lower latitudes predicted by BIOME4 during PD and MPWP, respectively. The biomes are classified into the 9 types of MEGABIOME scheme. The MPWP vegetation in the lower latitudes (Fig. 5.1c) generally shows larger area of moister biomes than those in PD (Fig. 5.1b) in accordance with the precipitation increase (Fig. 5.2b). Tropical forest in equatorial and eastern South America, equatorial and South Africa, and southeastern Asia expand for wider regions in MPWP relative to PD. In subtropical North and South Africa, Central Asia, and Australia, savanna and grassland shift poleward, thus reducing the fractional coverage of desert. For example, the fractions of the areas for tropical forest and desert in MPWP relative to those in PD on African continent change for +65% and –30%, respectively. The MPWP biomes also reveal poleward displacements of warm-temperate, temperate, and boreal forest in mid-latitudes, particularly in North America, Europe, and Asia, relative to PD. The increase in the coverage of warmer-temperate forest in the mid latitudes regions are mainly corresponding with the warmer surface condition (2~5 °C) in MPWP (Fig. 3.2a). The relative contributions of differences of the potential sunshine hours and atmospheric CO_2 concentration between MPWP and PD for the alterations in the biome patterns are minor (figures not shown) than those of the temperature and precipitation.

Blue/red circles in Fig. 5.1b (5.1c) represent whether the simulated biomes on individual sites in PD (MPWP) are match or mismatch with the reconstructed types of MPWP vegetation (Fig. 5.1a). The simulated MPWP vegetation (Fig. 5.1c) shows relatively better consistency with

the reconstructed MPWP biomes (Fig. 5.1a) rather than that in PD (Fig. 1b), particularly in the semi-arid regions. Figure 5.3a shows locations of the 10 sites in which the simulated biome types are inconsistent with the proxy data (Fig. 5.1a) in PD (Fig. 5.1b) but consistent in MPWP (Fig. 5.1c). Site numbers used in Salzmann et al. (2008) are labeled. The improving consistencies in the subtropical North Africa (site No. 113, 116), Arabian Peninsula (No. 120), and subtropical Australia (No. 179) correspond with the expansions of tropical forest, savanna, dry woodland, and grassland replaced by the drier biomes in the regions. The simulated transitions of biome types in the mid-latitudes are partly supported by the proxy records (No. 20, 91, 143, and 153). It is also noting that the simulated MEGABIOMEs on several sites in the MPWP experiment mismatch with the data (Fig. 5.3b). Generally, the discrepancies between the data and the model are located in subtropics, failing to reproduce the moister biomes by the model (savanna and forest are revealed by the data but grassland and savanna are simulated in the model). Relationships between anomalies in the climate parameters and the improvement of consistency (Fig. 5.3a) or the mismatch in MPWP biome simulation (Fig. 5.3b) are discussed in Section 5.4.

5.3 Evaluation of simulated MPWP climate

In this study, reproducibility of the anomaly (MPWP minus PD) climate derived from GCM is evaluated using paleovegetation records. However, the comparisons of the data and the model contain nonnegligible uncertainties. Discrepancies in the biome types between the data and the model using the anomaly procedure could be related to uncertainties in: (1) proxy data (spatial and/or temporal representativeness of sampling and non-uniformity); (2) present-day baseline climate (ground-based observation and human influences); (3) anomaly climate (GCM schemes and boundary conditions); and (4) biome simulation (BIOME4 scheme and experimental designs). Point-by-point comparisons in regional scale (scale with representativeness of a proxy data) contain considerable uncertainties as listed above. In larger scale (synoptic or continental scale), however, changes in climate state simulated by GCM might

be major factor for inconsistencies of general patterns between data and model. BIOME4 simulations are mainly determined by climate parameters if contributions of other factors (soil property and atmospheric CO_2 concentration) are minor. To note that the determinations of biome types by annual-mean climate parameters are limited, especially in the higher latitudes or high altitude regions, because the BIOME4 simulations under cold climate are strongly affected by seasonality in the parameters (e.g., accumulated growing-season warmth). In the lower latitude and low altitude regions, however, the general patterns of the alterations of MEGABIOME types are corresponding with the large-scale changes of the climate parameters, which is apparent in the annual-mean value.

With the climate parameters and the match/mismatch of the PD and MPWP biome simulations with the proxy data, we evaluate the anomaly climate as: (1) under (over) estimate when the climate parameter is deficient (excess) for the “match” range; or (2) good estimate when the climate parameter in MPWP is inside but that in PD is outside of the “match” range. The evaluations are not applied in case both the simulated biomes in PD and MPWP are consistent with the proxy data. Figure 5.4 shows the climate parameters in PD and MPWP with the simulated biome types and the matching/mismatching the individual sites. The major factors for the alterations in simulated MEGABIOME types in MPWP from PD in this study are the intensification of subtropical rainfall and the mid-latitude warming (Fig. 5.2). The simulated biomes plotted with surface temperature and rainfall in Fig. 5.4 are the most prominent types in the range of 2.8° square (1 GCM grid size) around the individual sites. Comparing to the matching range (gray and blue symbols), the mismatching cases (red symbols) are often outlier, implying the factor for the mismatching might be the under/over estimate in the climate parameters. In contrast, simulated biomes in some sites in MPWP match with the proxy data although those in PD mismatch, indicating the anomaly climate in the sites are good estimates (blue symbols in Fig. 5.4). The schematic of the determinations for the evaluations of climate parameters is also shown in Fig. 5.4.

The climate parameters in the sites predicting tropical forest as the most prominent type are only found in the condition under relatively sufficient rainfall (above ~2 mm day^{-1}) and warmer environment (above ~20 °C). In the cases of sites No. 114 and 169, the simulated types during MPWP are savanna or grassland although the reconstructed MPWP biomes are classified into tropical forest (Fig. 5.3a). These inconsistencies between the paleodata and the models are attributed to the insufficient rainfall in these sites during MPWP. In contrast, simulated biome transits from savanna in PD to tropical forest in MPWP on the island of Timor (No. 177), according with the increase in precipitation (+1.3 mm day^{-1}). We determine the evaluations of the precipitation anomalies superimposing on the PD climate as "under estimate" in the sites No. 114 and 169, and "good estimate" in No. 177. The evaluation method described above is also applied to the other types of MEGABIOMEs. Warm-temperate and temperate forests are dominant under conditions with sufficient amount of rainfall (Figs. 5.4b and 5.4c). Savanna and dry woodland are limited in relatively dry condition (Fig. 5.4b). Grassland sites (Fig. 5.4e) are appeared in the drier climate than savanna but wetter than desert (Fig. 5.4f). We exclude the sites No. 39 (Haiti) and No. 128 (Namibia) from the evaluation because the factors for the improving consistencies in MPWP relative to PD in these sites are not evident in the annual-mean changes of temperature and precipitation. The evaluations of the climate parameters in the individual sites are summarized in Table 5.1.

Figure 5.2 shows the changes in annual-mean temperature and precipitation simulated in Chapter 3 and their evaluations determined by the above method (Fig. 5.4 and Table 5.1). The simulated changes in biome types (Figs. 5.1b and 5.1c) corresponding with the temperature change (Fig. 5.2a) are consistent with the terrestrial proxies in several sites in mid latitude (Caspian Sea and Central China). In contrast, the simulated MPWP temperatures on 4 sites in the Central America (No. 35, 36, 38, and 42) are evaluated as overestimates. In this region, particularly around the continental Mexico, the geographical density of the paleosites for SST reconstruction (Dowsett et al. 2009) is relatively scarce, resulting lower confidence in the GCM

simulation in Chapter 3. In case for the precipitation change (Fig. 5.2b), the precipitation increases (~0.2 to 2.0 mm day^{-1}) in the semi-arid regions (subtropical North Africa, Arabian Peninsula, and subtropical Australia) are evaluated as sufficient (No. 113, 116, 120, 177, and 179) or underestimate (No. 114, 115, 111, 119, 169, and 181) for the reconstructed changes in the MEGABIOME types. The proxy-based biomes also reveal overestimate of simulated rainfall in some sites on western coast of the Pacific (Northeastern China and Southeastern Australia) in MPWP. The paleosites which are evaluated as the overestimates of the precipitation are only found in the relatively higher latitudes (southward from 35°S and northward from 35°N) although the major changes in precipitation are concentrated in the lower latitudes. These results reveal that the modeled-increases of precipitation in the subtropical regions are qualitatively consistent in all sites but the extents are partly deficient for the reconstructed-changes of the biomes.

5.4 Contribution of interactive response of vegetation to climate

The proxy data on some sites in semi-arid regions indicate the underestimates of precipitation increases in this study, which did not include the effects of the alterations in the geographical pattern of vegetation on the surface boundary in the GCM simulation. Differences of surface albedo and hydrological properties by altering the vegetation cover could change climate pattern through biogeophysical processes (surface/atmospheric heat budget and hydrological cycle). Simulated biomes with climate parameters derived from climate simulation prescribing the MPWP vegetation on surface boundary condition reveal larger expansions of moister vegetations in semi-arid regions than those in this study. Figure 5.1d shows results of biome simulations with climate parameters including the alteration of surface boundary condition to MPWP reconstructed vegetation (Salzmann et al. 2008) in GCM simulation (Fig. 5.1d, hereafter “MPWP+veg”) or not (Fig. 5.1c). These climate simulations are corresponding to “3 Ma” and “3 Ma_0veg” experiments in Chapter 3, respectively. The inclusion of the effect of

the reconstructed expansion of moister vegetation in biome simulation contributes to the extension of geographical coverage of tropical forest and shifts of savanna and grassland replacing desert in semi-arid regions, especially in the subtropical North Africa, Arabian Peninsula, South Asia, and subtropical Australia. For example, the coverages of tropical forest in "MPWP+veg" biome simulation change for +22% and +70% from those in MPWP on the African Continent and Australian Continent, respectively. In contrast, the fractional coverage of desert decreases for 14% on the African Continent and 47% in Australian Continent. The wider coverage of moister biomes in "MPWP+veg" relative to MPWP is attributed to the precipitation increase in the subtropical regions, especially in the subtropical North Africa, Arabian Peninsula, and subtropical Australia (Fig. 3.4f). The precipitation increase compensates its deficiency on the part of the under-estimated regions (Fig. 5.2b). In relation to the above, the paleodata on 5 sites reveal better consistency to "MPWP+veg" simulation relative to the MPWP simulation, especially in subtropics (southeastern Mexico, western Africa, southwestern Africa, and Central Australia). To note that the simulated MEGABIOME on the other 5 sites are inconsistent with the paleodata in "MPWP+veg" simulation although they are consistent with the data in MPWP simulation. The uncertainties in the GCM simulation, the BIOME model, and the paleodata should be verified carefully in the future. The previous studies (Haywood and Valdes 2006; Lunt et al. 2009) also reveal that the interactive responses of vegetation to climate under the sustained warmer Earth system contribute for the warmer conditions in mid- and high-latitude and the wetter climate in subtropics, which has an essential role for the evolutions of flora and fauna, including Hominids (e.g., Haywood and Valdes 2006; Kamae et al. 2011). These results indicate that the alteration of the terrestrial ecosystem has an important role for regional climate patterns under the warmer and moister condition for the sustained time.

5.5 Summary

The simulated climate during MPWP in the lower latitudes is evaluated by the

paleovegetation data. The predicted MPWP biomes based on the climate parameters show (1) meridional shift of temperate forest corresponding with the warming in the mid latitudes and (2) expansions of forests, savanna and grassland, and shrinking of desert in the subtropical regions according to the wetter conditions. The paleobotanical data supports the above tendencies including the changes in the geographical patterns of monsoon/desert climate in low latitude regions in accordance with the alterations of Hadley/Walker circulation under the sustained greenhouse world. In addition, the biome simulation including interactive response of vegetation to climate through the biogeophysical processes in the lower latitudes contributes to the more humid environment in the subtropics which is suggested by the paleodata.

This study also shows the regional inconsistencies between the data and the model, i.e., the overestimates of surface temperature around the Caribbean Sea and the overestimates of precipitation on the western coast of the Pacific. Further studies assessing about consistencies between different GCMs for the vegetation simulations are required for more confident evaluation of MPWP climate modeling in the future. Applications of the data-model comparison conducted in this study for the higher-latitude regions and other Pliocene simulations using air-sea coupled GCMs or Earth system models are also facilitated. They could help to provide insight into the earth climate system in the warmer world.

Table 5.1. Evaluation for simulated anomaly climate in each site represented in Fig. 5.2. Upper panel listed evaluation for the surface air temperature and bottom panel shows that for the precipitation rate.

Evaluations	Site numbers
Surface temperature	
under estimate	-
good estimate	91, 153
over estimate	35, 36, 38, 42
Precipitation	
under estimate	26, 37, 111, 114, 115, 116, 119, 156, 169, 181
good estimate	113, 116, 120, 143, 177, 179
over estimate	47, 160, 191

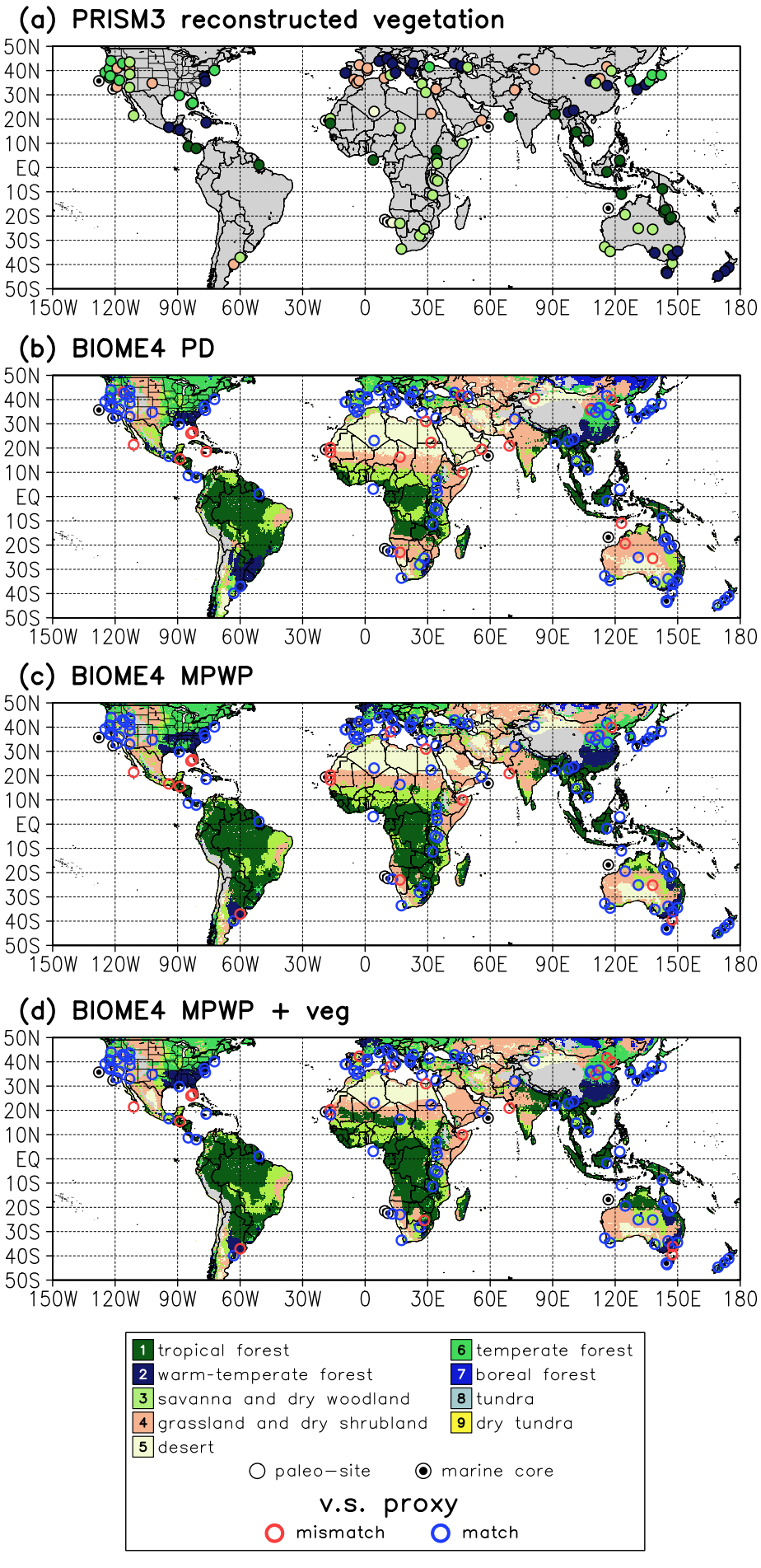
(a) PRISM3 reconstructed vegetation
(b) BIOME4 PD
(c) BIOME4 MPWP
(d) BIOME4 MPWP + veg
50N
40N
30N
20N
10N
EQ
10S
20S
30S
40S
50S
150W 120W 90W 60W 30W 0 30E 60E 90E 120E 150E 180
1 tropical forest
2 warm-temperate forest
3 savanna and dry woodland
4 grassland and dry shrubland
5 desert
6 temperate forest
7 boreal forest
8 tundra
9 dry tundra
paleo-site
marine core
v.s. proxy
mismatch
match

Fig. 5.1. (a) PRISM3 paleovegetation sites (118 sites in this study) and biomes during MPWP (modified from Haywood et al. 2009). Full references to paleo-sites are summarized in Salzmann et al. (2008). (b) Biomes in PD and (c) MPWP simulated by BIOME4 model. Red (blue) circles denote that the simulated biome mismatches (matches) with the reconstructed type of MPWP biomes on individual sites. All biome types are classified into the MEGABIOME scheme.

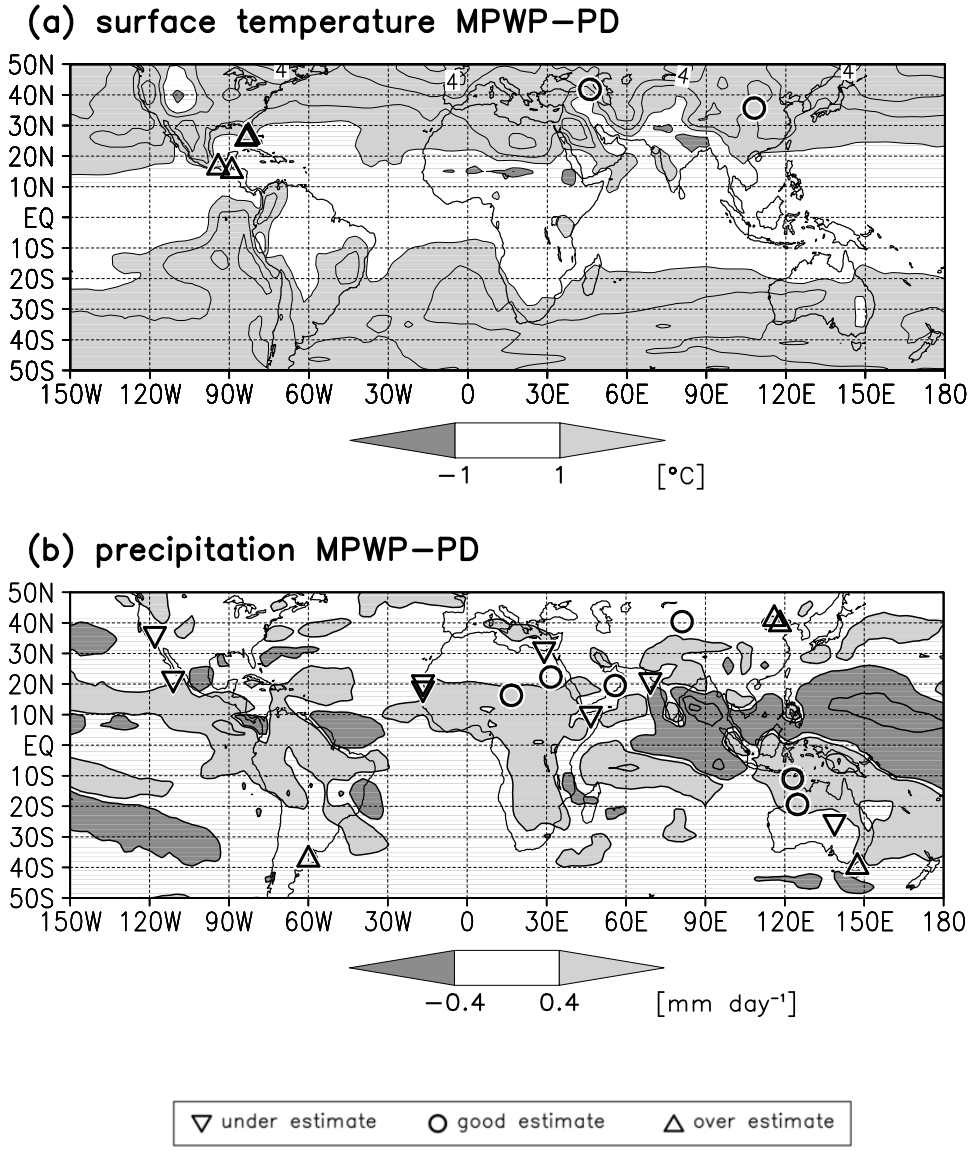

Fig. 5.2. Differences in the climate parameters for BIOME simulations between MPWP and PD. (a) Annual-mean surface air temperature (°C), and (b) precipitation rate (mm day^{-1}). Plotted symbols are evaluations of the climate parameters in individual sites. Details of the evaluations are described in Section 5.3.

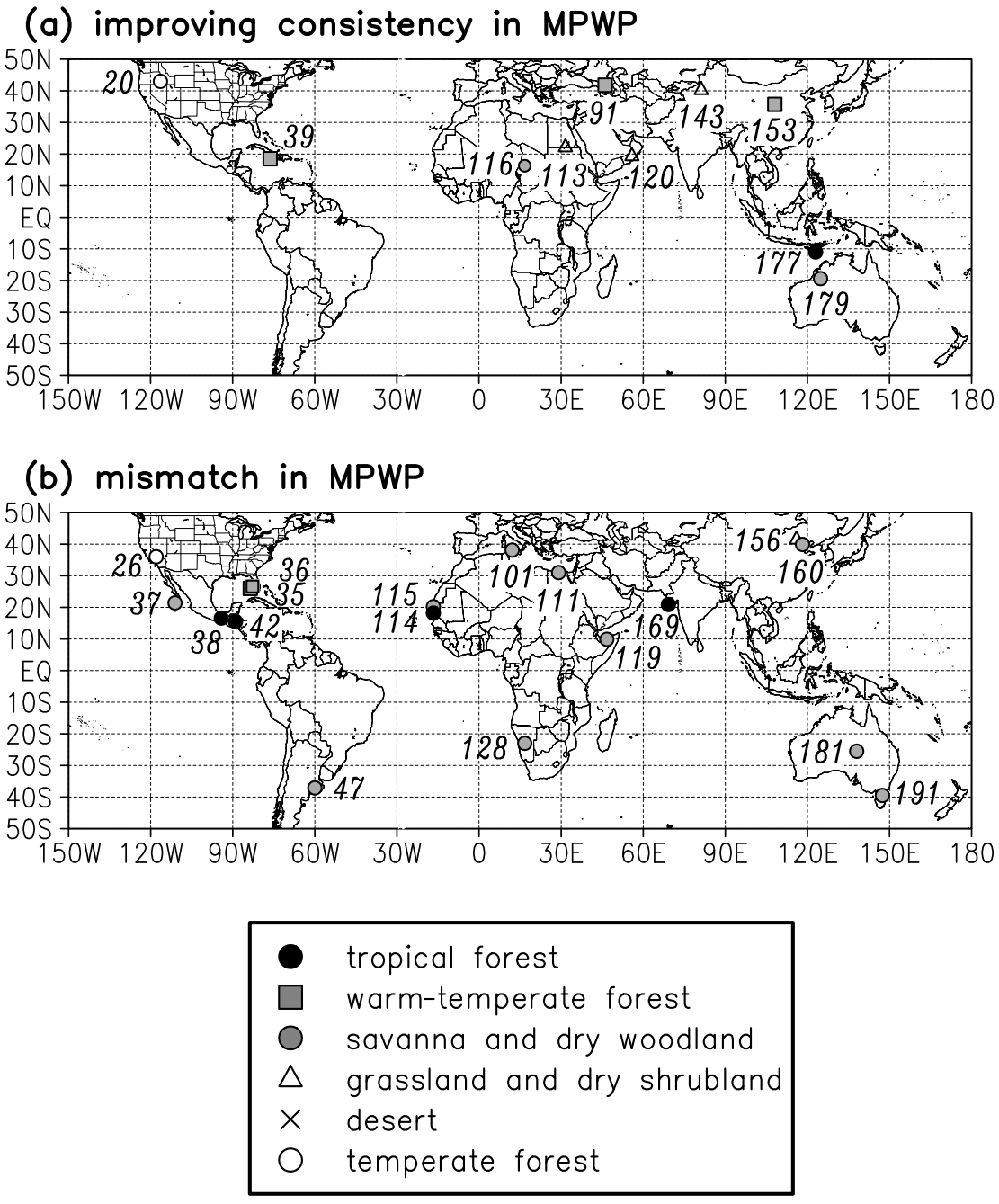

Fig. 5.3. Locations of paleovegetation sites in which the simulated biomes classified into MEGABIOME types are (a) match in MPWP with the proxy data but mismatch in PD and (b) mismatch in MPWP. Colors in the circles represent the reconstructed vegetation on the individual sites classified into the MEGABIOME classification scheme. The code noted by each site reveals the site number used in Salzmann et al. (2008).

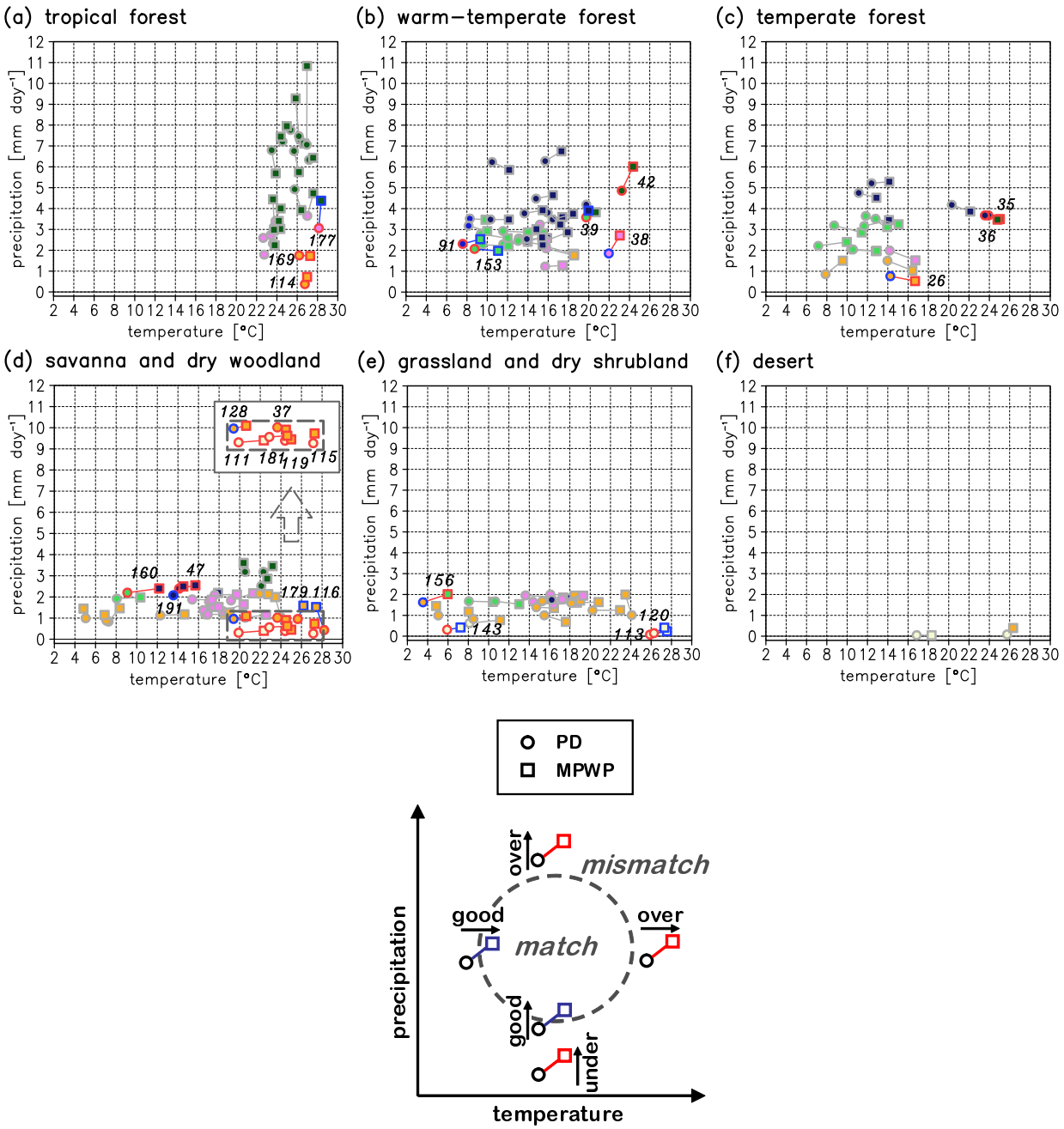

Fig. 5.4. Scatter diagram with annual-mean surface temperature (°C) and precipication rate (mm day^{-1}) on each site. A set of circle and square denote climate parameters in PD and MPWP on each site determined by the anomaly procedure, respectively. (a) The sites in which paleovegetation record is classified into tropical forest, (b) warm-temperate forest, (c) temperate forest, (d) savanna and dry woodland, (e) grassland and dry shrubland, and (f) desert. Colors in the symbols represent the simulated vegetation classified into the MEGABIOME types. Red (blue) symbols denote that the simulated biome mismatches (matches) with the reconstructed type on individual sites. Grey symbols denote that both the PD and MPWP biomes match with the proxies. Labeled codes reveal site numbers used in Salzmann et al. (2008). Schematic of the evaluations of climate parameters determined by the anomaly procedure is appended on the bottom.

6. Summary and conclusions

In Chapter 3, conducting the 3 Ma simulation and sensitivity experiments by use of AGCM forced by the PRISM3 boundary conditions, we have confirmed the physical mechanism for the weakening of tropical atmospheric circulation and wetter conditions in subtropics during 3 Ma. The prominent warming over the eastern Pacific and little change of SST over the western Pacific suppresses the intensity of the Walker circulation. The reduction of the meridional SST gradient corresponds with the weakening of Hadley circulation and the expansion of the ascending area in low latitude. It is also revealed that the proxy-suggested surface condition in low latitude have implications in the climate change during the Plio-Pleistocene transition and evolutions of flora and fauna, including Hominids, particularly in the subtropical Africa.

In Chapter 4, we investigate the radiative balance at TOA during 3 Ma and evaluate the effects of the individual boundary conditions quantitatively through the comparisons with the sensitivity experiments. In addition to the higher level of atmospheric CO_2 concentration (405 ppmv), the alteration of SST pattern in low latitude, reductions of meridional and east-west SST gradients, warms the Earth climate system by inducing the positive radiative forcing. The broadening of ascending area in low latitude corresponded with the weakening of meridional and east-west SST gradients suppresses the deep-convective activity and reduces the cloud amount over the warm-pool. The subtropical stratocumulus over the western coast of the continents is also reduced corresponding with the warmer surface condition over the eastern edge of the ocean basins, then enhancing the downward shortwave radiation over the regions. The responses of the cloud cover in low latitude corresponding to the SST pattern could help sustain the globally-warmer climate in 3 Ma.

In Chapter 5, using biogeography model to predict natural vegetation, the above tendencies in 3 Ma climate simulated by the AGCM are evaluated by the proxy data which

suggests the land-surface environment during 3 Ma. The paleobotanical data is generally consistent with the results of the 3 Ma experiment, indicating the confidence of the climate simulation in this study. The alteration of hydrological cycle corresponding with the changes in atmospheric circulation during 3 Ma is supported by the proxy data which shows wider area of the moister biomes in low latitude. The comparisons of the simulated biome with the proxy data also indicate that the simulated increase of precipitation in low latitude is partly underestimated. The interactive response of vegetation to climate through biogeophysical processes could contribute to the improving consistency with the proxy data.

The simulation of the mid-Pliocene greenhouse climate and its evaluation reveals that the climate change in low latitude has important role for the warmer Earth climate through the hydrological cycle, terrestrial ecosystem, and TOA radiative balance. Further comparisons of climate simulations conducted by different GCMs are needed to evaluate inter-model robustness and variations under the PlioMIP framework. Assessments of uncertainties in some types of proxy data and data-model comparisons have also essential roles for further insights of climate changes under different forcing from that of the present-day. It is also facilitated that the lively communications and discussions about complimentary information between modeling group and geologists to encourage paleoclimate research and comprehensive interpretations about past and future climate change.

Acknowledgements

I would like to sincerely thank all members who have helped to progress the study in this three years. Suggestive and helpful comments in scientific meetings, workshops, and seminars helped me to develop the analysis and discussions to the interdisciplinary study.

Firstly, I would like to show my best sincerely to advising professor, Associate Prof. Hiroaki Ueda who has supported over research activities in the Graduate School of Life and Environmental Sciences, University of Tsukuba. Supports and advices given by Associate Prof. Ueda improved many parts of this study relating to paleoclimate dynamics. Many ideas on analysis in this study were raised at discussions with him both in personal and at seminars. Countless comments and suggestions from the viewpoints of meteorology and climatology to this impact assessment study are given from Professors Yousay Hayashi, Hiroshi L. Tanaka, Kenichi Ueno, Hiroyuki Kusaka, and Yasutaka Wakazuki in the University of Tsukuba, which aid in proceeding development of this study. Additionally, I would like to show my special thanks to my seniors of Univ. of Tsukuba, Drs. Tomoshige Inoue, Terasaki Koji, Chieko Suzuki, Asuka P. Suzuki, Masatake E. Hori, Yasushi Watarai, Noriko Ishizaki, Sachiho Adachi, Shiori Sugimoto, friends in Graduate School of Life and Environmental Sciences, University of Tsukuba, and members of “climate laboratory” for their kind support and comments relating to use the research tools in the present study. Dr. Masamichi Ohba gave me helpful comments and technical supports for numerical climate modeling and analysis methods. I also acknowledge Dr. Akio Kitoh in the Meteorological Research Institute of Japan Meteorological Agency for providing the source code of MRI-CGCM2.3 and giving helpful comments on the paleoclimate simulations.

Secondly, I would sincerely thank for Professors and researchers in the University of Tokyo: Masahide Kimoto, Ayako Abe-Oouchi, Masahiro Watanabe, Masakazu Yoshimori, Ryota O’ishi, and Wing-Le Chang in Atmosphere-Ocean Research Institute and Hisashi Nakamura in

Research Center for Advanced Science and Technology, all of whom have gave me suggestive comments.

Thirdly, I also acknowledge Drs. Toru Nozawa, Seita Emori, Tatsuya Nagashima, Tomoo Ogura, Hideo Shiogama, Tokuta Yokohata, Manabu Abe, Strassmann Kuno, Hiroaki Kawase and Toshiharu Nagatomo in the National Institute for Environmental Studies (NIES), for their helpful support in the Graduate School of Life and Environmental Sciences, University of Tsukuba.

The authors would like to sincerely thank the PRISM group for providing the PRISM3 dataset. Prof. Alan Haywood in Leeds University and Harry Dowsett in U.S. Geological Survey given me helpful comments and financial support in participating for the PlioMIP workshop in U.S. Geological Survey, Reston, Verginia. I also thank NASA Global Change Master Directory website for providing source code of BIOME4 model. Part of the numerical calculation for the present work has been carried out under the “Interdisciplinary Computational Science Program” in Center for Computational Sciences, University of Tsukuba. This work is supported by the Global Environment Research Fund (S-5-2) of the Ministry of the Environment, Japan. All figures shown in this study are drawn by the Grid Analysis and Display System (GrADS).

Finally, I would like to show special thanks to my parents. They have kept supporting me mentally and financially. Deepest and particular appreciation should be brought to my familiar friends. The achievement of this study is essentially due to their mental supports and encouragements.

References

Abe-Ouchi, A., S. Segawa, and F. Saito, 2007: Climatic conditions for modelling the Northern Hemisphere ice sheets throughout the ice age cycle. *Clim. Past*, **3**, 423–438.

Arakawa, A. and W. H. Schubert, 1974: Interaction of a cumulus cloud ensemble with the large scale environment, Part I. *J. Atmos. Sci*., **31**, 674–701.

Axelrod, D. I., and P. H. Raven, 1978: Late Cretaceous and Tertiary vegetation history of Africa. In *Biogeography and Ecology of Southern Africa,* Eds. Werger, M. J. A., Junk, The Hague, 77–130.

Barreiro, M., G. Philander, R. Pacanowski, and A. Fedorov, 2006: Simulations of warm tropical conditions with application to Middle Pliocene atmospheres. *Climate Dyn*., **26**, 349–365.

Barron, J. A., 1996a: Diatom constraints on the position of the Antarctic Polar Front in the middle part of the Pliocene. *Mar. Micropaleontol*., 27, 195–213.

Barron, J. A., 1996b: Diatom constraints on sea surface temperatures and sea ice distribution during the middle part of the Pliocene. *U.S. Geol. Surv. Open File Rep*., 96–713.

Bartoli, G., M. Sarnthein, M. Weinelt, H. Erlenkeuser, D. Garbe-Schönberg, and D. W. Lea, 2005: Final closure of Panama and the onset of northern hemisphere glaciation. *Earth Planet. Sci. Lett*., **237**, 33–44.

Billups, K., A. C. Ravelo, and J. C. Zachos, 1997: Early Pliocene deep-water circulation: stable isotope evidence for enhanced northern component deep water. *Proc. Ocean Drill. Program, Sci. Results*, **154**, 319–330.

Braconnot, P., B. Otto-Bliesner, S. Harrison, S. Joussaume, J.-Y. Peterchmitt, A., Abe-Ouchi, M. Crucifix, E. Driesschaert, Th. Fichefet, C. D. Hewitt, M. Kageyama, A. Kitoh, A. Laine, M.-F. Loutre, O. Marti, U. Merkel, G. Ramstein, P. Valdes, L. Weber, Y. Yu, and Y. Zhao, 2007a: Results of PMIP2 coupled simulations of the mid-Holocene and Last Glacial Maximum - Part 1: experiments and large-scale features. *Clim. Past*, **3**, 261–277.

Braconnot, P., B. Otto-Bliesner, S. Harrison, S. Joussaume, J.-Y. Peterchmitt, A. Abe-Ouchi, M. Crucifix, E. Driesschaert, Th. Fichefet, C. D. Hewitt, M. Kageyama, A. Kitoh, M.-F. Loutre, O. Marti, U. Merkel, G. Ramstein, P. Valdes, S. L. Weber, Y. Yu, and Y. Zhao, 2007b: Results of PMIP2 coupled simulations of the Mid-Holocene and Last Glacial Maximum - Part 2: feedbacks with emphasis on the location of the ITCZ and mid-and high latitudes heat budget. *Clim. Past*, **3**, 279–296.

Bradley, R. S., 1999: *Paleoclimatology: Reconstructing Climate of the Quaternary*. London, Elisevier, 614 pp.

Brierley, C. M., and A. V. Fedorov, 2010: Relative importance of meridional and zonal sea surface temperature gradients for the onset of the ice ages and Pliocene-Pleistocene climate evolution. *Paleoceanography*, **25**, PA2214, doi:10.1029/2009PA001809.

Brierley, C. M., A. V. Fedorov, Z. Liu, T. D. Herbert, K. T. Lawrence, and J. P. LaRiviere, 2009: Greatly expanded tropical warm pool and weakened Hadley circulation in the early Pliocene. *Science*, **323**, 1714–1718.

Cess, R. D., G. L. Potter, J. P. Blanchet, G. J. Boer, A. D. Del Genio, and co-authors, 1990: Intercomparison and interpretation of climate feedback processes in 19 atmospheric general circulation models. *J. Geophys. Res*., **95**, 16601–16615.

Chan, W.-L., A. Abe-Ouchi, and R. Ohgaito, 2011: Simulating the mid-Pliocene climate with the MIROC general circulation model: experimental design and initial results. *Geosci. Model Dev.*, **4**, 1035–1049.

Chandler, M. A., D. Rind, and R. S. Thompson, 1994: Joint investigations of the middle Pliocene climate II: GISS GCM Northern Hemisphere results. *Global Planet. Change*, **9**, 197–219.

Charney, J. G., 1975: Dynamics of deserts and drought in the Sahel. *Quart. J. Roy. Meteor. Soc*., **101**, 193–202.

Claussen, M., 1997: Modeling bio-geophysical feedback in the African and Indian monsoon region. *Climate Dyn*., **13**, 247–257.

Claussen, M., 2009: Late Quaternary vegetation-climate feedbacks. *Clim. Past*, **5**, 203–216.

Cronin, T. M., H. J. Dowsett, G. S. Dwyer, P. A. Baker, and M. A. Chandler, 2005: Mid-Pliocene deep-sea bottom-water temperatures based on ostracode Mg/Ca ratios. *Mar. Micropaleontol*., **54**, 249–261.

Crowley, T. J., 1996: Pliocene climates: The nature of the problem. *Mar. Micropaleontol*., **27**, 3–12.

Cubasch, U., E. Zorita, F. Kaspar, J. F. Gonzalez-Rouco, H. von Storch, and K. Prömmel, 2006: Simulation of the role of solar and orbital forcing on climate. *Advances in Space Research*, **37**, 1629–1634.

Dekens, P. S., A. C. Ravelo, and M. D. McCarthy, 2007: Warm upwelling regions in the Pliocene warm period. *Paleoceanography*, **22**, PA3211, doi:10.1029/2006PA001394.

deMenocal, P. B., 1995: Plio-Pleistocene African climate. *Science*, **270**, 53–59.

deMenocal, P. B., and D. Rind, 1993: Sensitivity of Asian and African climate to variations in seasonal insolation, glacial ice cover, sea surface temperature, and Asian orography. *J. Geophys. Res*., **98**, 7265–7287.

deMenocal, P., J. Ortiz, T. Guilderson, J. Adkins, M. Sarnthein, L. Baker, and M. Yarusinsky, 2000: Abrupt onset and termination of the African Humid Period: rapid climate responses to gradual insolation forcing. *Quart. Sci. Rev*., **19**, 347–361.

Dowsett, H. J., and M. M. Robinson, 2009: Mid-Pliocene equatorial Pacific sea surface temperature reconstruction: a multi-proxy perspective. *Phil. Trans. R. Soc. A*, **367**, 109–125.

Dowsett, H. J., R.S. Thompson, J. A. Barron, T. M. Cronin, R. F. Fleming, S. E. Ishman, R. Z. Poore, D. A. Willard, and T. R. Holtz, 1994: Joint investigations of the middle Pliocene climate I: PRISM paleoenvironmental reconstructions. *Global Planet. Change*, **9**, 169–195.

Dowsett, H., J. Barron, and R. Poore, 1996: Middle Pliocene sea surface temperatures: a global

reconstruction. *Mar. Micropaleontol*., **27**, 13–26.

Dowsett, H. J., J. A. Barron, R. Z. Poore, R. S. Thompson, T. M. Cronin, S. E. Ishman, and D. A. Willard, 1999: Middle Pliocene paleoenvironmental reconstruction: PRISM2. *U.S. Geol. Surv. Open File Rep*., 99–535.

Dowsett, H. J., M. A. Chandler, and M. M. Robinson, 2009a: Surface temperatures of the Mid-Pliocene North Atlantic Ocean: implications for future climate. *Phil. Trans. R. Soc. A*, **367**, 69–84.

Dowsett, H. J., M. M. Robinson, and K. M. Foley, 2009b: Pliocene three-dimensional global ocean temperature reconstruction. *Clim. Past*, **5**, 769–783.

Dowsett, H. J., M. M. Robinson, A. M. Haywood, U. Salzmann, D. Hill, L. Sohl, M. Chandler, M. Williams, K. Foley, and D. K. Stoll, 2010: The PRISM3D paleoenvironmental reconstruction. *Stratigraphy*, **7**, 123–139.

Etourneau, J., R. Schneidera, T. Blanza, and P. Martinez, 2010: Intensification of the Walker and Hadley atmospheric circulations during the Pliocene-Pleistocene climate transition. *Earth Planet. Sci. Lett*., **297**, 103–110.

FAO 1995: *Digital soil map of the world and derived soil properties*. Food and Agric. Org., Rome.

Fedorov, A. V., P. S. Dekens, M. McCarthy, A. C. Ravelo, P. B. deMenocal, M. Barreiro, R. C. Pacanowski, and S. G. Philander, 2006: The Pliocene paradox (mechanisms for a permanent El Niño). *Science*, **312**, 1485–1489.

Fedorov, A. V., C. M. Brierley, and K. Emanuel, 2010: Tropical cyclones and permanent El Niño in the early Pliocene epoch. *Nature*, **463**, 1066–1070.

Harrison, S. P., and I. C. Prentice, 2003: Climate and CO_2 controls on global vegetation distribution at the last glacial maximum: analysis based on palaeovegetation data, biome modelling and palaeoclimate simulations. *Glob. Change Biol*., **9**, 983–1004.

Harrison, S. P., J. E. Kutzbach, I. C. Prentice, P. J. Behling, and M. T. Sykes, 1995: The response

of northern hemisphere extratropical climate and vegetation to orbitally induced changes in insolation during the last interglaciation. *Quat. Res*., **43**, 174–184.

Harrison, S. P., D. Jolly, F. Laarif, A. Abe-Ouchi, B. Dong, K. Herterich, C. Hewitt, S. Joussaume, J. E. Kutzbach, J. Mitchell, N. De Noblet, and P. Valdes, 1998: Intercomparison of simulated global vegetation distributions in response to 6 kyr BP orbital forcing. *J. Climate*, **11**, 2721–2741.

Hastenrath, S., 1991: *Climate dynamics of the tropics*. Kluwer Academic Publishers, Dortrecht, 488 pp.

Haug, G. H., and R. Tiedemann, 1998: Effect of the formation of the Isthmus of Panama on Atlantic Ocean thermohaline circulation. *Nature*, **393**, 673–676.

Haxeltine, A., and I. C. Prentice, 1996: BIOME3: An equilibrium terrestrial biosphere model based on ecophysiological constraints, resource availability, and competition among plant functional types. *Global Biogeochem. Cycles*, **10**, 693–709.

Haywood, A. M., and P. J. Valdes, 2006: Vegetation cover in a warmer world simulated using a dynamic global vegetation model for the Mid-Pliocene. *Palaeogeogr. Palaeoclimatol. Palaeoecol*., **237**, 412–427.

Haywood, A. M., P. J. Valdes, and B. W. Sellwood, 2000: Global scale palaeoclimate reconstruction of the middle Pliocene climate using the UKMO GCM: initial results. *Global Planet. Change*, **25**, 239–256.

Haywood, A. M., P. Dekens, A. C. Ravelo, and M. Williams, 2005: Warmer tropics during the mid-Pliocene? Evidence from alkenone paleothermometry and a fully coupled ocean-atmosphere GCM. *Geochem. Geophys. Geosyst*., **6**, Q03010, doi:10.1029/2004GC000799.

Haywood, A. M., H. J. Dowsett, P. J. Valdes, D. J. Lunt, J. E. Francis, and B. W. Sellwood, 2009a: Introduction. Pliocene climate, processes and problems. *Phil. Trans. R. Soc. A*, **367**, 3–17.

Haywood, A. M., M. A. Chandler, P. J. Valdes, U. Salzmann, D. J. Lunt, and H. J. Dowsett, 2009b: Comparison of mid-Pliocene climate predictions produced by the HadAM3 and GCMAM3 General Circulation Models. *Global Planet. Change*, **66**, 208–224.

Haywood, A. M., H. J. Dowsett, B. Otto-Bliesner, M. A. Chandler, A. M. Dolan, D. J. Hill, D. J. Lunt, M. M. Robinson, N. Rosenbloom, U. Salzmann, and L. E. Sohl, 2010: Pliocene Model Intercomparison Project (PlioMIP): experimental design and boundary conditions (Experiment 1). *Geosci. Model Dev*., **3**, 227–242.

Haywood, A. M., H. J. Dowsett, M. M. Robinson, D. K. Stoll, A. M. Dolan, D. J. Lunt, B. Otto-Bliesner, and M. A. Chandler, 2011: Pliocene Model Intercomparison Project (PlioMIP): experimental design and boundary conditions (Experiment 2). *Geosci. Model Dev*., **4**, 571–577.

Held, I. M., and B. J. Soden, 2006: Robust responses of the hydrological cycle to global warming. *J. Climate*, **19**, 5686–5699.

Herbert, T. D., and J. D. Schuffert, 1998: Alkenone unsaturation estimates of late Miocene through late Pliocene sea-surface temperatures at Site 958. *Proc. Ocean Drill. Program Sci. Results*, **159T**, 17–21.

Hutchinson, M. F., 1995: Interpolating mean rainfall using thin plate smoothing splines. *International Journal of GIS*, **9**, 385–403.

Hutchinson, M. F., and R. J. Bischof, 1983: A new method of estimating mean seasonal and annual rainfall for the Hunter Valley, New South Wales. *Australian Meteorological Magazine*, **31**, 179–184.

Jansen, E., J. Overpeck, K. R. Briffa, J. -C. Duplessy, F. Joos, V. Masson-Delmotte, D. Olago, B. Otto-Bliesner, W. R. Peltier, S. Rahmstorf, R. Ramesh, D. Raynaud, D. Rind, O. Solomina, R. Villalba, and D. Zhang, 2007: Palaeoclimate. In *Climate change 2007: the physical science basis. Contribution of working group I to the fourth assessment report of the Intergovernmental Panel on Climate Change,* Eds. S. Solomon, D. Qin, M. Manning, Z.

Chen, M. Marquis, K. B. Averyt, M. Tignor, and H. L. Miller, Cambridge University Press, Cambridge, 433–498.

Jiang, D., H. Wang, Z. Ding, X. Lang, and H. Drange, 2005: Modeling the middle Pliocene climate with a global atmospheric general circulation model. *J. Geophys. Res*., **110**, D14107, doi:10.1029/2004JD005639.

Joussaume, S., K. E. Taylor , P. Braconnot, J. F. B. Mitchell, J. E. Kutzbach, S. P. Harrison, I. C. Prentice, A. J. Broccoli, A. Abe-Ouchi, P. J. Bartlein, C. Bonfils, B. Dong, J. Guiot, K. Herterich, C. D. Hewitt, D. Jolly, J. W. Kim, A. Kislov, A. Kitoh, M. F. Loutre, V. Masson, B. McAvaney, N. McFarlane, N. de Noblet, W. R. Peltier, J. Y. Peterschmitt, D. Pollard, D. Rind, J. F. Royer, M. E. Schlesinger, J. Syktus, S. Thompson, P. Valdes, G. Vettoretti, R. S. Webb, and U. Wyputta, 1999: Monsoon changes for 6000 years ago: results of 18 simulations from the Paleoclimate Modeling Intercomparison Project (PMIP). *Geophys. Res. Lett.,* **26**, 859–862.

Kamae, Y., and H. Ueda, 2011: Evaluation of simulated climate in lower latitude regions during the mid-Pliocene warm period using paleovegetation data. *SOLA*, **7**, 177–180.

Kamae, Y., and H. Ueda, 2012a: Radiative balance at top of the atmosphere in mid-Pliocene climate simulation prescribing PRISM3 boundary conditions. *Tellu A*, submitted.

Kamae, Y., and H. Ueda, 2012b: Mid-Pliocene global climate simulation with MRI-CGCM2.3: set-up and initial results of PlioMIP Experiments 1 and 2. *Geosci. Model Dev*., submitted.

Kamae, Y., H. Ueda, and A. Kitoh, 2011: Hadley and Walker circulations in the mid-Pliocene warm period simulated by an atmospheric general circulation model. *J. Meteor. Soc. Japan*, **89**, 475–493.

Kaplan, J. O., N. H. Bigelow, I. C. Prentice, S. P. Harrison, P. J. Bartlein, T. R. Christensen, W. Cramer, N. V. Matveyeva, A. D. McGuire, D. F. Murray, V. Y. Razzhivin, B. Smith, D. A. Walker, P. M. Anderson, A. A. Andreev, L. B. Brubaker, M. E. Edwards, and A. V. Lozhkin, 2003: Climate change and Arctic ecosystems: 2. Modeling, paleodata-model comparisons,

and future projections. *J. Geophys. Res*., **108**(**D19**), 8171.

Karas, C., D. Nürnberg, A. K. Gupta, R. Tiedemann, K. Mohan, and T. Bickert, 2009: Mid-Pliocene climate change amplified by a switch in Indonesian subsurface throughflow. *Nature Geosci*., **2**, 434–438.

Kitoh, A., and S. Murakami, 2002: Tropical Pacific climate at the mid-Holocene and the Last Glacial Maximum simulated by a coupled ocean-atmosphere general circulation model. *Paleoceanography*, **17**, 1047, doi:10.1029/2001PA000724.

Kitoh, A., S. Murakami, and H. Koide, 2001: A simulation of the Last Glacial Maximum with a coupled atmosphere-ocean GCM. *Geophys. Res. Lett*., **28**, 2221–2224.

Knies, J., J. Matthiessen, C. Vogt, and R. Stein, 2002: Evidence of 'Mid-Pliocene (~3 Ma) global warmth' in the eastern Arctic Ocean and implications for the Svalbard/Barents Sea ice sheet during the late Pliocene and early Pleistocene (~3 - 1.7 Ma). *Boreas*, **31**, 82–93.

Koenig, S. J., R. M. DeConto, and D. Pollard, 2012: Pliocene Model Intercomparison Project Experiment 1: implementation strategy and mid-Pliocene global climatology using GENESIS v3.0 GCM. *Geosci. Model Dev.*, **5**, 73–85.

Knutti, R., and G. C. Hegerl, 2008: The equilibrium sensitivity of the Earth's temperature to radiation changes. *Nature Geosci.*, **1**, 735–743.

Kürschner, W. M., J. Van der Burgh, H. Visscher, and D. L. Dilcher, 1996: Oak leaves as biosensors of Late Neogene and Early Pleistocene paleoatmospheric CO_2 concentrations. *Mar. Micropaleontol*., **27**, 299–312.

Krishnamurti, T. N., 1971: Tropical east-west circulations during the northern summer. *J. Atmos. Sci*. **28**, 1342–1347.

Leemans, R., and W. P. Cramer, 1991: *The IIASA database for mean monthly values of temperature, precipitation, and cloudiness on a global terrestrial grid*. International Institute for Applied System Analysis (IIASA), Laxenburg, Austria, 62 pp.

Leroy, S., and L. Dupont, 1994: Development of vegetation and continental aridity in

northwestern Africa during the Late Pliocene: the pollen record of ODP site 658. *Palaeogeogr. Palaeoclimatol. Palaeoecol*., **109**, 295–316.

Li, L., Q. Li, J. Tian, P. Wang, H. Wang, and Z. Liu, 2011: A 4-Ma record of thermal evolution in the tropical western Pacific and its implications on climate change. *Earth Planet. Sci. Lett*., **309**, 10–30.

Lisiecki, L. E., and M. E. Raymo, 2005: A Pliocene-Pleistocene stack of 57 globally distributed benthic δ18O records. *Paleoceanography*, **20**, PA1003, doi:10.1029/2004PA001071.

Lu, J., G. A. Vecchi, and T. Reichler, 2007: Expansion of the Hadley cell under global warming. *Geophys. Res. Lett*., **34**, L06805, doi:10.1029/2006GL028443.

Lu, J., G. Chen, and D. M. W. Frierson, 2008: Response of the zonal mean atmospheric circulation to El Niño versus global warming. *J. Climate*, **21**, 5835-5851.

Lunt, D. J., P. J. Valdes, A. Haywood, and I. C. Rutt, 2008a: Closure of the Panama Seaway during the Pliocene: implications for climate and Northern Hemisphere glaciation. *Climate Dyn*., **30**, 1-18.

Lunt, D. J., G. L. Foster, A. M. Haywood, and E. J. Stone, 2008b: Late Pliocene Greenland glaciation controlled by a decline in atmospheric CO_2 level. *Nature*, **454**, 1102-1105.

Lunt, D. J., A. M. Haywood, G.. L. Foster, and E. J. Stone, 2009: The Arctic cryosphere in the Mid-Pliocene and the future. *Phil. Trans. R. Soc. A*., **367**, 49–67.

Lunt, D. J., A. M. Haywood, G. A. Schmidt, U. Salzmann, P. J. Valdes, and H. J. Dowsett, 2010: Earth system sensitivity inferred from Pliocene modelling and data. *Nature Geosci*., **3**, 60–64.

Manabe, S., and R. T. Wetherald, 1967: Thermal equilibrium of the atmosphere with a given distribution of relative humidity. *J. Atmos. Sci*., **24**, 241–259.

Marlow, F. R., C. B. Lange, G. Wefer, and A. Rosell-Mele, 2000: Upwelling intensification as part of the Pliocene-Pleistocene climate transition. *Science*, **290**, 2288–2291.

Matthiessen, J., J. Knies, C. Vogt, and R. Stein, 2009: Pliocene palaeoceanography of the Arctic

Ocean and subarctic seas. *Phil. Trans. R. Soc. A*, **367**, 21–48.

McLaren, S., and M. W. Wallace, 2010: Plio-Pleistocene climate change and the onset of aridity in southeastern Australia. *Global Planet. Change*, **71**, 55–72.

Meehl, G. A., T. F. Stocker, W. D. Collins, P. Friedlingstein, A. T. Gaye, J. M. Gregory, A. Kitoh, R. Knutti, J. M. Murphy, A. Noda, S. C. B. Raper, I. G. Watterson, A. J. Weaver, and Z. -C. Zhao, 2007: Global climate projections. In *Climate change 2007: the physical science basis. Contribution of working group I to the fourth assessment report of the Intergovernmental Panel on Climate Change,* Eds. S. Solomon, D. Qin, M. Manning, Z. Chen, M. Marquis, K. B. Averyt, M. Tignor, and H. L. Miller, Cambridge University Press, Cambridge, 747–846.

Melillo, J. M., A. D. McGuire, D. W. Kicklighter, B. Moore, C. J. Vorosmarty, and A. L. Schloss, 1993: Global climate change and terrestrial net primary production. *Nature*, **363**, 234–240.

Ohba, M., and H. Ueda, 2010: A GCM study on effects of continental drift on tropical climate at the early and late Cretaceous. *J. Meteor. Soc. Japan*, **88**, 869–881.

O'ishi, R., A. Abe-Ouchi, I. C. Prentice, and S. Sitch, 2009: Vegetation dynamics and plant CO_2 responses as positive feedbacks in a greenhouse world. *Geophys. Res. Lett.*, **36**, L11706, doi:10.1029/2009GL038217.

Oort, A. H., and J. J. Yienger, 1996: Observed interannual variability in the Hadley circulation and its connection to ENSO. *J. Climate*, **9**, 2751–2767.

Otto-Bliesner, B. L., S. J. Marshall, J. T. Overpeck, G. H. Miller, A. Hu, and CAPE Last Interglacial Project members, 2006: Simulating Arctic climate warmth and icefield retreat in the last intergration. *Science*, **311**, 1751–1753.

Otto-Bliesner, B. L., S. P. Harrison, and A. Abe-Ouchi, 2009: Modeling and data syntheses of past climates. *EOS Trans. AGU*, **90**, 93–93.

Pagani, M., Z. Liu, J. Lariviere, and A. C. Ravelo, 2010: High Earth-system climate sensitivity determined from Pliocene carbon dioxide concentrations. *Nature Geosci.*, **3**, 27–30.

Peixoto, J., and A. Oort, 1992: *The physics of climate*. American Institute of Physics, New York, 520 pp.

Philander, S. G., and A. V. Fedorov, 2003: Role of tropics in changing the response to Milankovich forcing some three million years ago. *Paleoceanography*, **18**, 1045, doi:10.1029/2002PA000837.

Poore, H. R., R. Samworth, N. J. White, S. M. Jones, and I. N. McCave, 2006: Neogene overflow of Northern Component Water at the Greenland-Scotland Ridge. *Geochem. Geophys. Geosyst.*, **7**, Q06010, doi:10.1029/2005GC001085.

Prell, W. L., and J. E. Kutzbach, 1987: Monsoon variability over the past 150,000 years. *J. Geophys. Res.*, **92**, 8411–8425.

Ramanathan, V., R. D. Cess, E. F. Harrison, P. Minnis, B. R. Barkstrom, E. Ahmad, and D. Hartmann, 1989: Cloud-radiative forcing and climate: Results from the earth radiation budget experiment. *Science*, **243**, 57–63.

Randall, D., and D. -M. Pan, 1993: Implementation of the Arakawa-Schubert cumulus parameterization with a prognostic closure. *Meteorological Monograph/The representation of cumulus convection in numerical models*, **46**, 145–150.

Ravelo, A. C., 2010: Warmth and glaciation. *Nature Geosci*, **3**, 672-674.

Ravelo, A. C., D. H. Andreasen, M. Lyle, A. O. Lyle, and M. W. Wara, 2004: Regional climate shifts caused by gradual global cooling in the Pliocene epoch. *Nature*, **429**, 263–267.

Raymo, M. E., B. Grant, M. Horowitz, and G. H. Rau, 1996: Mid-Pliocene warmth: stronger greenhouse and stronger conveyor. *Mar. Micropaleontol.*, **27**, 313–326.

Reed-Sterrett, C., P. S. Dekens, L. D. White, and I. W. Aiello, 2010: Cooling upwelling regions along the California margin during the early Pliocene: Evidence for a shoaling thermocline. *Stratigraphy*, **7**, 141–150.

Reichler, T., M. Dameris, and R. Sausen, 2003: Determining the tropopause height from gridded data. *Geophys. Res. Lett.*, **30**, 2042, doi:10.1029/2003GL018240.

Robinson, M. M., 2009: New quantitative evidence of extreme warmth in the Pliocene arctic. *Stratigraphy*, **6**, 1–10.

Robinson, M. M., P. J. Valdes, A. M. Haywood, H. J. Dowsett, D. J. Hill, and S. M. Jones, 2011: Bathymetric controls on Pliocene North Atlantic and Arctic sea surface temperature and deepwater production. *Palaeogeogr. Palaeoclimatol. Palaeoecol.*, **309**, 92–97.

Rodwell, M. J., and B. J. Hoskins, 1996: Monsoons and the dynamics of deserts. *Quart. J. Roy. Meteor. Soc.*, **122**, 1385–1404.

Salzmann, U., A. M. Haywood, D. J. Lunt, P. J. Valdes, and D. J. Hill, 2008: A new global biome reconstruction and data-model comparison for the Middle Pliocene. *Glob. Ecol. Biogeogr.*, **17**, 432–447.

Salzmann, U. A., M. Haywood, and D. J. Lunt, 2009: The past is a guide to the future? Comparing Middle Pliocene vegetation with predicted biome distributions for the twenty-first century. *Phil. Trans. R. Soc. A*, **367**, 189–204.

Salzmann, U., J. B. Riding, A. E. Nelson, and J. L. Smellie, 2011: How likely was a green Antarctic Peninsula during warm Pliocene interglacials? A critical reassessment based on new palynofloras from James Ross Island. *Palaeogeogr. Palaeoclimatol. Palaeoecol.*, **309**, 73–82.

Sarnthein, M., G. Bartoli, M. Prange, A. Schmittner, B. Schneider, M.Weinelt, N. Andersen, and D. Garbe-Schönberg, 2009: Mid-Pliocene shifts in ocean overturning circulation and the onset of Quaternary-style climates. *Clim. Past*, **5**, 269–283.

Sato, N., P. J. Sellers, D. A. Randall, E. K. Schneider, J. Shukla, J. L. Kinter, Y. -Y. Hou, and E. Albertazzi, 1989: Effects of implementing the simple biosphere model in a general circulation model. *J. Atmos. Sci.*, **46**, 2757–2782.

Sellers, P. J., Y. Mintz, Y. C. Sud, and A. Dalcher, 1986: A simple biosphere model (SiB) for use within general circulation models. *J. Atmos. Sci.*, **43**, 505–531.

Sloan, L. C., T. J. Crowley, and D. Pollard, 1996: Modeling of middle Pliocene climate with the

NCAR GENESIS general circulation model. *Mar. Micropaleontol*., **27**, 51–61.

Soden, B. J., and I. M. Held, 2006: An assessment of climate feedbacks in coupled ocean-atmosphere models. *J. Climate*, **19**, 3354–3360.

Sohl, L. E., M. A. Chandler, R. B. Schmunk, K. Mankoff, J. A. Jonas, K. M. Foley, and H. J. Dowsett, 2009: PRISM3/GISS topographic reconstruction. *U.S. Geological Survey Data Series*, **419**, 6 pp.

Steph, S., R. Tiedemann, M. Prange, J. Groeneveld, M. Schulz, A. Timmermann, D. Nürnberg, C. Rühlemann, C. Saukel, and G. H. Haug, 2010: Early Pliocene increase in thermohaline overturning: A precondition for the development of the modern equatorial Pacific cold tongue. *Paleoceanography*, **25**, PA2202, doi:10.1029/2008PA001645.

Thompson, R. S., and R. F. Fleming, 1996: Middle Pliocene vegetation: reconstructions, paleoclimatic inferences, and boundary conditions for climate modeling. *Mar. Micropaleontol*., **27**, 27–49.

Ueda, H., H. Kuroki, M. Ohba, and Y. Kamae, 2011: Seasonally asymmetric transition of the Asian monsoon in response to ice age boundary conditions. *Climate Dyn*., **37**, 2167–2179.

Van der Burgh, J., H. Visscher, D. L. Dilcher, and W. M. Kürschner, 1993: Paleoatmospheric signatures in Neogene fossil leaves. *Science*, **260**, 1788–1790.

Wara, M. W., A. C. Ravelo, and M. L. Delaney, 2005: Permanent El Niño-like conditions during the Pliocene warm period. *Science*, **309**, 758–761.

Wohlfahrt, J., S. P. Harrison, P. Braconnot, C. D. Hewitt, A. Kitoh, U. Mikolajewicz, B. L. Otto-Bliesner, and S. L. Weber, 2008: Evaluation of coupled ocean-atmosphere simulations of the mid-Holocene using palaeovegetation data from the northern hemisphere extratropics. *Climate. Dyn*., **31**, 871–890.

World Meteorological Organization, 1957: Meteorology - A three-dimensional science: Second session of the commission for aerology. *WMO Bull*., **IV**, 134–138.

Yan, Q., Z. Zhang, H. Wang, Y. Gao, and W. Zheng, 2011: Set-up and preliminary results of

mid-Pliocene climate simulations with CAM3.1. *Geosci. Model Dev. Discuss*., **4**, 3339–3361.

Yu, B., and G. J. Boer, 2002: The roles of radiation and dynamical processes in the El Niño-like response to global warming. *Climate Dyn*., **19**, 539–553.

Yu, B., and F. W. Zwiers, 2010: Changes in equatorial atmospheric zonal circulations in recent decades. *Geophys. Res. Lett.*, **37**, L05701, doi:10.1029/2009GL042071.

Yukimoto, S., A. Noda, A. Kitoh, M. Sugi, Y. Kitamura, M. Hosaka, K. Shibata, S. Maeda, and T. Uchiyama, 2001: The new meteorological research institute coupled GCM (MRI-CGCM2) -Model climate and variability-. *Pap. Meteor. Geophys*., **51**, 47–88.

Yukimoto, S., A. Noda, A. Kitoh, M. Hosaka, H. Yoshimura, T. Uchiyama, K. Shibata, O. Arakawa, and S. Kusunoki, 2006: Present-day and climate sensitivity in the meteorological research institute coupled GCM version 2.3 (MRI-CGCM2.3). *J. Meteor. Soc. Japan*, **84**, 333–363.

Zachos, J., M. Pagani, L. Sloan, E. Thomas, and K. Billups, 2001: Trends, rhythms, and aberrations in global climate 65 Ma to present. *Science*, **292**, 686–693.

Appendix

List of abbreviations

0 Ma: 0 Million years ago

3 Ma: 3 Million years ago

3 Ma_0Land ice: 3 Ma experiment forced by prescribed 0 Ma land ice

3 Ma_0Sea ice: 3 Ma experiment forced by prescribed 0 Ma sea ice

3 Ma_0SST: 3 Ma experiment forced by prescribed 0 Ma SST

3 Ma_0Topo: 3 Ma experiment forced by prescribed 0 Ma topography

3 Ma_0Veg: 3 Ma experiment forced by prescribed 0 Ma vegetation

3 Ma_AtlZSST: 3 Ma experiment forced by prescribed ZSST in Atlantic Ocean and SST in Pacific and Indian Ocean

3 Ma_PIZSST: 3 Ma experiment forced by prescribed ZSST in Pacific and Indian Ocean and SST in Atlantic Ocean

3 Ma_ZSST: 3 Ma experiment forced by prescribed ZSST

AGCM: Atmospheric General Circulation Model

CS: Clear-Sky radiative flux

CRF: Cloud Radiative Forcing

FAO: Food and Agriculture Organization

GDD: Growing Degree Days

ITCZ: Inter-Tropical Convergence Zone

MMC: Mean Meridional Circulation

MPWP: Mid-Pliocene Warm Period

MRI-CGCM2.3: Meteorological Research Institute Coupled General Circulation Model version 2.3

PD: Present-Day

PlioMIP: Pliocene Model Intercomparison Project

PRISM3: Pliocene Research, Interpretation and Synoptic Mapping phase 3

SiB: Simple Biosphere

SPCZ: Southern Pacific Convergence Zone

SST: Sea Surface Temperature

T42: Triangle truncation wavenumber 42

TOA: Top Of the Atmosphere

USGS: the United State Geological Survey

ZSST: Zonal-mean SST anomaly

ZASST: Zonally-Asymmetric SST anomaly